Modeling and Control of an Elastic Ship-Mounted Crane Using Variable-Gain Model-Based Controller

Von der Fakultät für Ingenieurwissenschaften, Abteilung Maschinenbau der
Universität Duisburg-Essen
zur Erlangung des akademischen Grades

DOKTOR-INGENIEUR

genehmigte Dissertation

von

Yousef M. Al-Sweiti
aus
Hebron

Referent: Univ.-Prof. Dr.-Ing. Dirk Söffker
Korreferent: Univ.-Prof. Dr. Manfred Braun
Tag der mündlichen Prüfung: 08.08.2006

Dedication

To

my parents,

and

my wife

Acknowledgment

I would like to thank Prof. Dr.-Ing. Dirk Söffker for his powerful supervision, suggestions and continuous encouragements in every stage of my work. His support has not restricted only to my academic work but also extended to my social life in Germany. He gave me full access to the facilities and laboratories owned by the department which led at the end to the successful experimental realization of the work.

I am also very grateful to Prof. Dr. Manfred Braun for his efforts in co-referring and reviewing my work. I am also thankful to Mr. Kurt Thelen for his help and practical ideas during constructing the test rig.

Special thank to the German Academic Exchange Service (DAAD) for their financial support during my research period in Germany.

Duisburg, August 2006

Yousef Al-Sweiti

Abstract

This work deals with mathematical modeling and control of elastic ship-mounted cranes which have the Maryland Rigging. The developed model contains three independent inputs to control the vibrations in the plane of the boom; the luff angle is utilized to ensure the controllability of the elastic boom, and the total length of the upper cable in conjunction with the position of its lower suspension point are used to guarantee the controllability of the payload. The disturbance acting on the ship due to sea motions is represented by the rolling displacement of the ship about its center of gravity. The full nonlinear model of the crane is developed and Taylor series is utilized to expand the nonlinear terms about the current equilibrium point which vary with the luff angle and the length of the upper cable. This has led to a linear model with additive nonlinear terms (higher order terms) collected in a separate column vector.

Simulation results show that, within a considerable range of pendulation displacements of the payload, the nonlinear model and the linearized one obtained by neglecting the nonlinear terms from consideration reflect nearly equivalent responses. Consequently, the linear model is used to design the control system of the crane. The coefficient matrices of this linear model are calculated at the current (instantaneous) equilibrium point, which vary with the luff angle and the length of the upper cable, therefore, a variable-model problem is created and accordingly a variable-gain observer and a variable-gain controller are designed to cover the operation of the crane for all possible equilibrium points in the working space of the crane.

The switching between these gains takes place automatically according to the output of a region finder, which uses the measurements of the luff angle and the length of the upper cable to detect the current operating region. A PI-Observer is used to estimate the states and the unknown disturbance force or forces acting directly on the payload; this guarantees that the estimated states converge to their true values even though a nonzero disturbance force acts on the payload. The controller uses the estimated states and the measured roll angle to create the required damping and to compensate for the rolling action of the ship. Stability and performance robustness of the system are ensured for the total working space and also for the expected range of the payload mass. Simulation and experimental results show that the observer can estimate the states and the unknown disturbance acting on the payload very well and the controller can reduce the payload pendulations significantly.

Contents

1 Introduction

1.1 Motivation

Ship-mounted cranes are used to transfer cargo from one ship to another in an open sea as shown in Fig. 1.1. They are used also at port to transfer cargo from large ships to lighter port-going vessels when ports of deep water are not available. During the transfer process, wave-induced motions of the crane can produce large oscillations of the cargo being hoisted, especially if the exciting frequency coming from the sea waves is close to the resonance frequency of the crane. This endangers the operation of the crane and forces the cargo transfer to be suspended.

Figure 1.1: Picture of a ship-mounted crane at sea

Ship-mounted cranes are discussed in the last few years in several publications. Yuan et al. [YHG97] proposed the “Maryland’s Rigging” and applied a brake system to the upper cable as it passes over the pulley, Kimiaghalam et al. [KHB99] proposed a fuzzy controller to limit the pendulation of the payload by changing the length of the upper cable, Dadone and Van Landingham [DV99] proposed fuzzy logic for controlling the Coulomb friction in the pulley, Kimiaghalam et al. [KHB00] proposed feedback and feedforward control law to change the luff angle and the length of the rope. Abdel-Rahman and Nayfeh [AN01] examined the in-plane and out-of-plane responses of the crane to an in-plane excitation and a control effort limited to dry friction and viscous damping applied at the pulley.

In the cited publications, the authors studied rigid boom cranes and assumed that the actuators are able to realize the calculated control inputs. In reality, these assumptions

may be difficult to apply because the rigid boom is usually massive, which means that it may be difficult to realize the proposed perfect drive dynamics.

This work focuses on modeling and control of an elastic ship-mounted crane equipped with the Maryland rigging, which transforms a crane from a single pendulum to double pendulum to improve the controllability over the payload; the upper pendulum consists of a pulley riding on a cable suspended from two different points on the boom, and the lower pendulum consists of the payload suspended by a cable from the pulley.

An elastic light-weight boom is considered, and a small modification in the configuration of the crane is proposed by adding a limited degree of mobility to the lower suspension point of the upper cable on which the pulley rides. This leads to a new type (construction) of ship cranes which has lighter-weight booms and can respond faster to the operator commands with less power consumption. The finite element method is used to model the elastic boom dynamics, which is coupled with the dynamics of the pulley and the payload. The model contains three independent inputs to control the planar vibrations of the elastic boom and the payload; the luff angle $\rho(t)$ is proposed to ensure the controllability of the elastic boom, and the total length of the upper cable $L(t)$ in addition to the position of its lower suspension point $D(t)$ to ensure the controllability of the payload. This guarantees the complete state controllability of the system. The model considers the in-plane oscillations which are dangerous in practical applications. The disturbances acting on the crane are represented by the rolling displacement $\Delta\delta$ of the ship about its center of gravity and the wind forces p_2 acting directly on the payload as shown in Fig. 2.1.

1.2 Organization of the thesis

The thesis consists of five chapters; Chapter 1 gives a brief introduction with some literature reviews, Chapter 2 concerns the development of the mathematical model of the elastic and rigid parts of the crane, the nonlinear terms are separated using Taylor series expansion and the model is examined by simulations to investigate the effect of the nonlinearity in the overall response for different operating conditions. In Chapter 3, the state space representation of the crane is given. A variable-gain PI-Observer is designed to reconstruct the states and the unknown disturbance force acting directly on the payload during the cargo transfer process. This kind of observer improves the robustness and the steady state error in estimating the states because the disturbance force is reconstructed and then taken into consideration inside the observer feedback loop while reconstructing the states of the system. Here a controller consisting of two variable-gain parts is defined; the first part is defined to compensate for the measured rolling motion of the ship and the second part (an optimal variable-gain part), which is based on minimizing a performance index, aims to create the necessary damping in the

crane. The experimental validation using a scaled test rig is presented in Chapter 4; the rolling disturbance is generated using a hydraulic cylinder connected to the base of the crane. The luff angle of the elastic boom and the position of the lower suspension point of the upper cable are controlled by two separate hydraulic cylinders mounted on the appropriate positions. The length of the cable is controlled by a DC motor integrated with a spur gear box. The necessary measurements are carried out using a strain gauge and a set of potentiometers, and the controller is implemented using a dSPACE signal processor system. Finally, Chapter 5 summarizes the results and conclusions with some recommendations which may be useful for future studies.

2 Model development

This chapter deals with model development of elastic ship-mounted cranes which have the Maryland Rigging as shown in Fig. 2.1. The elastic boom is modeled using the finite element method. The dynamics of the payload and the other rigid parts are expressed by Newton's second law. Three inputs are assigned to control the planar vibrations of the elastic boom and payload due to the planar base excitation. The model is limited to the in-plane oscillations because those have the dangerous effect in practical applications in comparison to the other effects as heave and pitch motions. The disturbances acting on the system are represented by the rolling displacement of the ship due to sea motions, and the wind force acting directly on the payload.

2.1 Assumptions

In deriving the mathematical model of the crane, the following assumptions are considered:

- The lower part of the boom (part AB) is elastic, while the upper part (part BC) is rigid.
- The mass of the cables is neglected.
- The elongation of the cables and the structural damping of the boom are neglected.
- The lower suspension point B' of the upper cable is movable along the rigid part of the boom.
- The pulley m_1 riding on the upper cable is frictionless.
- The luff angle ρ, which represents the rotation of the boom axis with respect to the ship, is altered by the moment M_A applied directly to the lower end of the boom.
- The angle β represents the orientation of the boom axis with respect to the horizontal. It is equal to the (algebraic) sum of the roll angle $\Delta\delta$ and the luff angle ρ.
- The disturbances acting on the crane are the rolling action of the ship due to sea motions in addition to the force p_2 acting directly on the payload; this force may appear due to a strong wind or a direct impact force which may happen by accident during the operation of the crane.

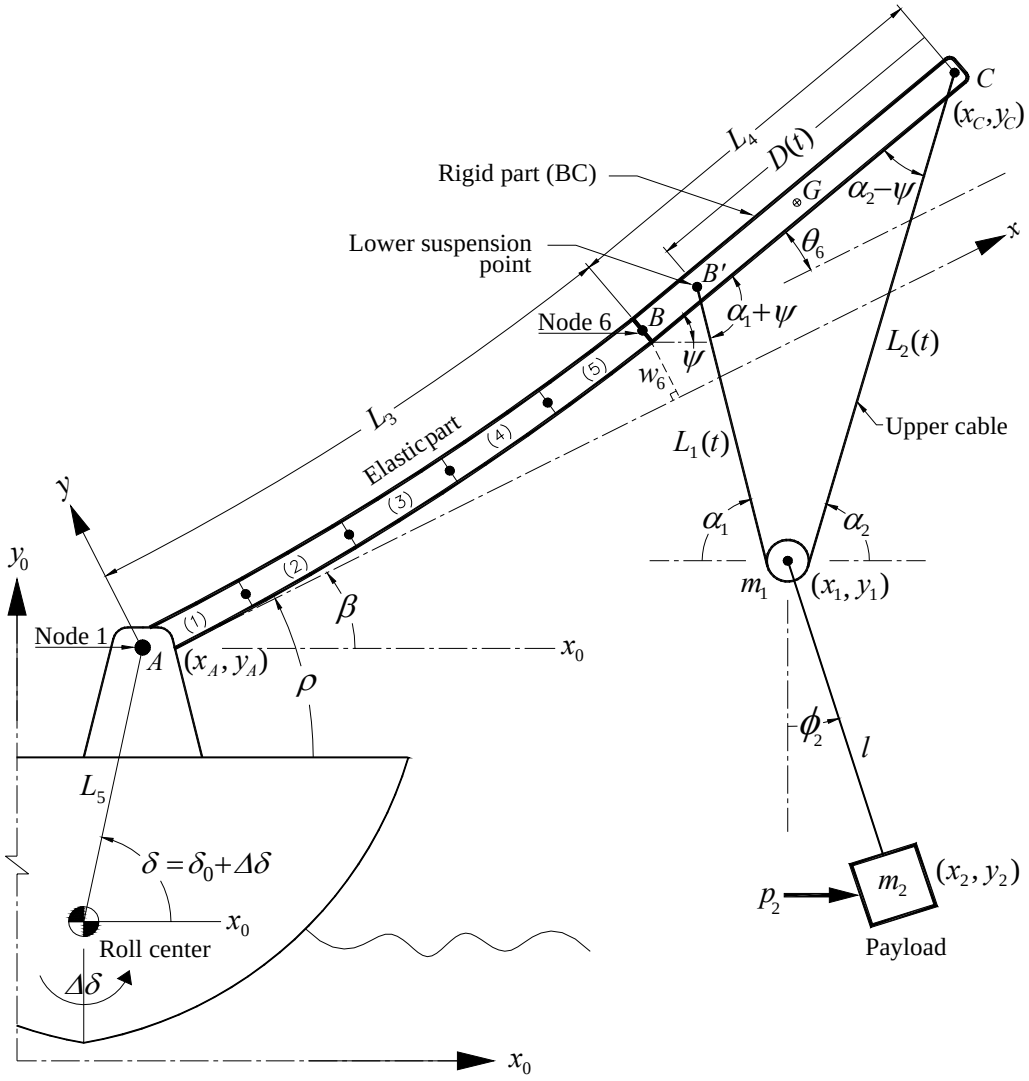

Figure 2.1: Modified crane configuration with Maryland Rigging

2.2 Kinematics of the upper cable

With reference to Fig. 2.1, it is assumed that L_1 and L_2 are the distances between the pulley and the lower and upper suspension points (*B'* and *C*) respectively. By applying the sine law, these distances can be expressed as

$$L_1 = D\,s(\alpha_2 - \psi)\csc(\alpha_1 + \alpha_2) \tag{2.1}$$

$$L_2 = D\,s(\alpha_1 + \psi)\csc(\alpha_1 + \alpha_2). \tag{2.2}$$

So the total length of the cable is given by

$$L(t) = L_1 + L_2$$
$$= D\,c(\psi + \frac{\alpha_1 - \alpha_2}{2})\sec(\frac{\alpha_1 + \alpha_2}{2}), \tag{2.3}$$

where s and c are the abbreviations for the trigonometric sine and cosine functions respectively, α_1 and α_2 denote the angles of L_1 and L_2 with respect to the horizontal, D represents the position of the movable suspension point B' along the portion BC with respect to the tip of the boom, and

$$\psi = \beta + \theta_6 \tag{2.4}$$

is the planar orientation of BC with respect to the horizontal, with

$$\beta = \rho + \Delta\delta, \tag{2.5}$$

where ρ denotes the luff angle of the boom, the angle θ_6 is the elastic rotational displacement at node 6 which represents the end point of the elastic portion of the boom, and $\Delta\delta$ denotes the ship roll angle due to sea motions. Reformulating Eq.(2.3) and utilizing the trigonometric relations to isolate α_1 give

$$\frac{s\frac{\alpha_1}{2}}{c\frac{\alpha_1}{2}} = \frac{L\,c\frac{\alpha_2}{2} - D\,c(\frac{\alpha_2}{2} - \psi)}{L\,s\frac{\alpha_2}{2} + D\,s(\frac{\alpha_2}{2} - \psi)}. \tag{2.6}$$

Therefore, the above equation yields

$$\frac{\alpha_1}{2} = \text{Atan2}\left[\left(L\,c\frac{\alpha_2}{2} - D\,c(\frac{\alpha_2}{2} - \psi)\right), \left(L\,s\frac{\alpha_2}{2} + D\,s(\frac{\alpha_2}{2} - \psi)\right)\right], \tag{2.7}$$

where Atan2(y,x) is the arctangent function of two arguments; it expresses the arctangent of the ratio y/x but utilizes the sign of each argument to determine which quadrant the resulting angle belongs to.

Applying the cosine law to the triangle spanned by L_1, L_2, and D gives

$$L_1^2 = L_2^2 + D^2 - 2L_2 D\,c(\alpha_2 - \psi). \tag{2.8}$$

The length L_1 can be expressed as

$$L_1 = L - L_2. \tag{2.9}$$

Thus

$$L^2 - 2LL_2 + L_2^2 = L_2^2 + D^2 - 2L_2 D\, c(\alpha_2 - \psi) \tag{2.10}$$

Solving Eq. (2.10) for L_2 leads

$$L_2 = \frac{1}{2}\left(\frac{L^2 - D^2}{L - D\, c(\alpha_2 - \psi)} \right). \tag{2.11}$$

Differentiating Eq. (2.11) with respect to time gives

$$\dot{L}_2 = \gamma_1 \dot{L} + \gamma_2 \dot{D} + \gamma_3 (\dot{\alpha}_2 - \dot{\psi}) \tag{2.12}$$

$$\ddot{L}_2 = \gamma_1 \ddot{L} + \gamma_2 \ddot{D} + \gamma_3 (\ddot{\alpha}_2 - \ddot{\psi}) + f_2, \tag{2.13}$$

with the abbreviations

$$\begin{aligned}
\gamma_1 &= \frac{L^2 + D^2 - 2DL\, c(\alpha_2 - \psi)}{2[L - D\, c(\alpha_2 - \psi)]^2} \\
\gamma_2 &= \frac{[L^2 + D^2]\, c(\alpha_2 - \psi) - 2DL}{2[L - D\, c(\alpha_2 - \psi)]^2} \\
\gamma_3 &= \frac{[D^3 - DL^2]\, s(\alpha_2 - \psi)}{2[L - D\, c(\alpha_2 - \psi)]^2} \\
f_2 &= \dot{\gamma}_1 \dot{L} + \dot{\gamma}_2 \dot{D} + \dot{\gamma}_3 (\dot{\alpha}_2 - \dot{\psi}).
\end{aligned} \tag{2.14}$$

2.3 Kinematics of the pulley

The global position of the pulley is described as

$$x_1 = x_C - L_2\, c\alpha_2, \tag{2.15}$$

$$y_1 = y_C - L_2\, s\alpha_2, \tag{2.16}$$

where the coordinates x_C and y_C of the tip of the boom with respect to the inertial reference frame can be represented by

$$x_C = x_A + L_3\, c\beta - w_6\, s\beta + L_4\, c\psi, \tag{2.17}$$
$$y_C = y_A + L_3\, s\beta + w_6\, c\beta + L_4\, s\psi. \tag{2.18}$$

Here w_6 denotes the transverse displacement of point B with respect to the straight boom. The shortening of the length L_3 of the elastic boom due to its deflection is neglected. The base pivot A has the coordinates

$$\begin{aligned} x_A &= L_5\, c\delta \\ &= L_5\, c(\delta_0 + \Delta\delta), \end{aligned} \tag{2.19}$$

$$\begin{aligned} y_A &= L_5\, s\delta \\ &= L_5\, s(\delta_0 + \Delta\delta), \end{aligned} \tag{2.20}$$

where δ_0 represents the elevation angle of the base pivot of the crane with respect to the ship's roll center, and $\Delta\delta$ denotes the roll angle of the ship.
Differentiating Eqs. (2.15, 2.16) twice with respect to time gives the acceleration components of the pulley as

$$\ddot{x}_1 = \ddot{x}_C - c\alpha_2 \ddot{L}_2 + 2s\alpha_2 \dot{L}_2 \dot{\alpha}_2 + L_2(s\alpha_2 \ddot{\alpha}_2 + c\alpha_2 \dot{\alpha}_2^2) \tag{2.21}$$
$$\ddot{y}_1 = \ddot{y}_C - s\alpha_2 \ddot{L}_2 - 2c\alpha_2 \dot{L}_2\, \dot{\alpha}_2 - L_2(c\alpha_2 \ddot{\alpha}_2 - s\alpha_2 \dot{\alpha}_2^2). \tag{2.22}$$

2.4 Kinematics of the payload

The global position of the payload is expressed as

$$x_2 = x_1 + l\, s\phi_2 \tag{2.23}$$
$$y_2 = y_1 - l\, c\phi_2, \tag{2.24}$$

which is differentiated twice with respect to time to give the absolute acceleration of the payload as

$$\ddot{x}_2 = \ddot{x}_1 + l\, c\phi_2\, \ddot{\phi}_2 - l\, s\phi_2\, \dot{\phi}_2^2 \tag{2.25}$$
$$\ddot{y}_2 = \ddot{y}_1 + l\, s\phi_2\, \ddot{\phi}_2 + l\, c\phi_2\, \dot{\phi}_2^2. \tag{2.26}$$

2.5 Kinetics of the payload

According to the elements of the free-body diagram shown in Fig. 2.2, applying Newton's second law to the payload in x_2-and y_2-directions gives

$$p_2 - T_3 s\phi_2 = m_2 \ddot{x}_2 \tag{2.27}$$

$$T_3 c\phi_2 - m_2 g = m_2 \ddot{y}_2, \tag{2.28}$$

where T_3 denotes the tension of the payload cable. Using Eq. (2.28) to eliminate T_3 from Eq. (2.27) and inserting Eqs. (2.25, 2.26) in the resultant equation, the differential equation of m_2 in implicit form can be written as

$$m_2 c\phi_2 \ddot{x}_1 + m_2 l\ddot{\phi}_2 + m_2 s\phi_2 (g + \ddot{y}_1) = p_2 c\phi_2, \tag{2.29}$$

which in view of Eqs. (2.21, 2.22) gives the full nonlinear equation of motion of the payload in explicit form as

$$\begin{aligned}
&- m_2 s(\beta - \phi_2)\ddot{w}_6 + m_2[\gamma_3 c(\alpha_2 - \phi_2) - L_4 s(\psi - \phi_2)]\ddot{\theta}_6 \\
&+ m_2[\gamma_3 c(\alpha_2 - \phi_2) - L_3 s(\beta - \phi_2) - w_6 c(\beta - \phi_2) - L_4 s(\psi - \phi_2)]\ddot{\beta} \\
&- m_2\gamma_1 c(\alpha_2 - \phi_2)\ \ddot{L} - m_2\gamma_2 c(\alpha_2 - \phi_2)\ddot{D} \\
&+ m_2[L_2 s(\alpha_2 - \phi_2) - \gamma_3 c(\alpha_2 - \phi_2)]\ddot{\alpha}_2 \\
&+ m_2 l\ddot{\phi}_2 + m_2 c\phi_2\ \ddot{x}_A + m_2 s\phi_2\ \ddot{y}_A + m_2 g s\phi_2 - m_2 f_2 c(\alpha_2 - \phi_2) \\
&- 2m_2\dot{w}_6\dot{\beta}\, c(\beta - \phi_2) - m_2\dot{\beta}^2[L_3 c(\beta - \phi_2) - w_6\, s(\beta - \phi_2)] \\
&- m_2 L_4\dot{\psi}^2\, c(\psi - \phi_2) + m_2 L_2\dot{\alpha}_2^2\, c(\alpha_2 - \phi_2) \\
&+ 2m_2\, s(\alpha_2 - \phi_2)\dot{\alpha}_2[\gamma_1\dot{L} + \gamma_2\dot{D} + \gamma_3\dot{\alpha}_2 - \gamma_3\dot{\psi}] = p_2 c\phi_2 .
\end{aligned} \tag{2.30}$$

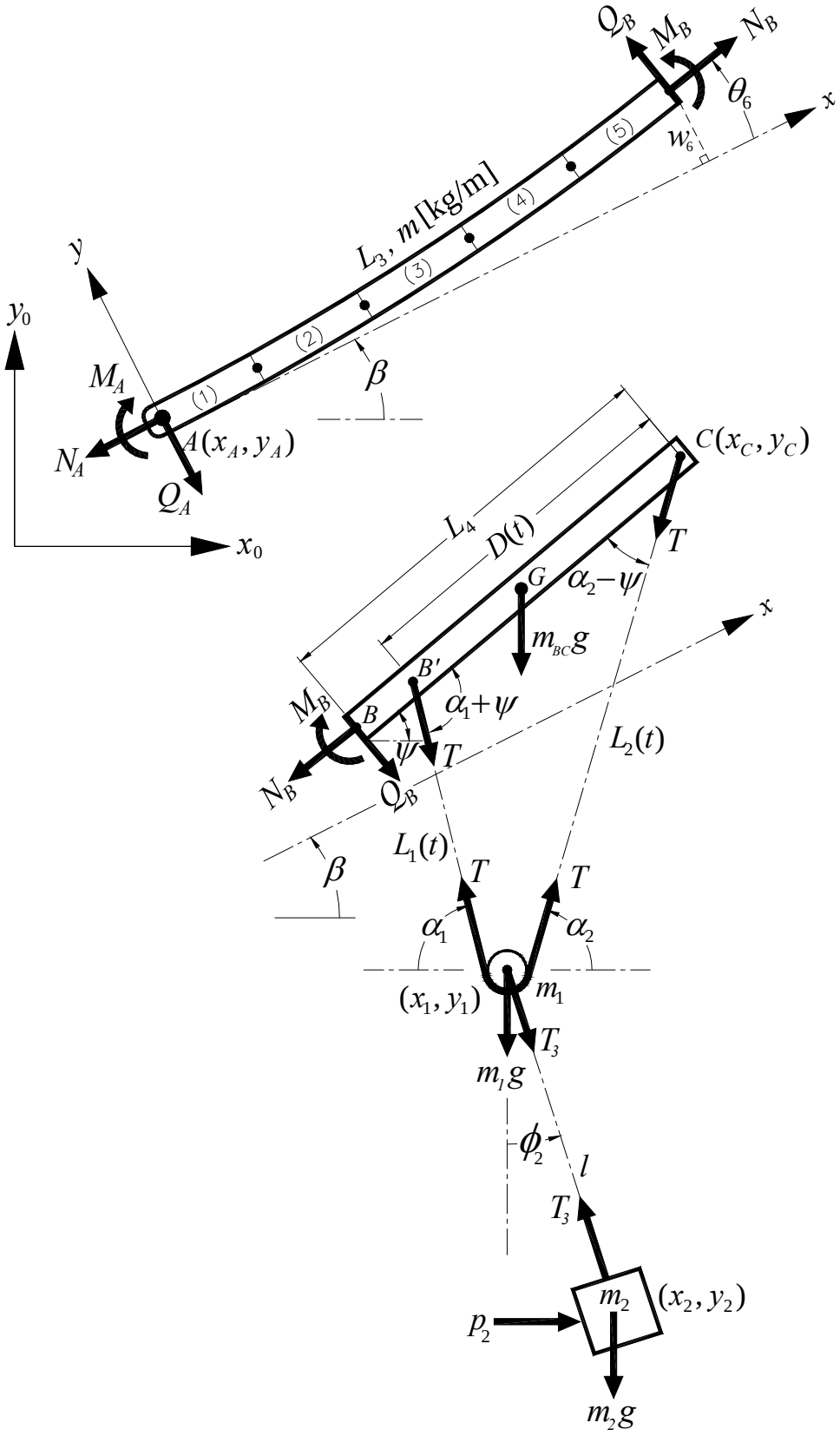

Figure 2.2: Free body diagram of the elastic and rigid parts

2.6 Kinetics of the pulley

With respect to the free-body diagram of the pulley in Fig. 2.2, and assuming that the pulley is ideal, then the tension in L_1 is equal to the tension in L_2. Hence, applying Newton's second law in x_1-and y_1-directions give

$$T\,(c\alpha_2 - c\alpha_1) + T_3\, s\phi_2 = m_1\ddot{x}_1 \tag{2.31}$$

$$T\,(s\alpha_1 + s\alpha_2) - m_1 g - T_3\, c\phi_2 = m_1\ddot{y}_1. \tag{2.32}$$

Substituting Eq. (2.28) into Eq. (2.32) and utilizing Eq. (2.26) yield the magnitude of the tension in the upper cable as

$$T = \frac{(m_1 + m_2)(g + \ddot{y}_1) + m_2(l\ddot{\phi}_2 s\phi_2 + l\dot{\phi}_2^2 c\phi_2)}{s\alpha_1 + s\alpha_2}. \tag{2.33}$$

Substituting Eqs. (2.27, 2.33) into Eq. (2.31) and using Eq. (2.25) give the full nonlinear equation of motion of the pulley in implicit form as

$$\begin{aligned}\left(\frac{c\alpha_2 - c\alpha_1}{s\alpha_1 + s\alpha_2}\right)&[(m_1 + m_2)(g + \ddot{y}_1) + m_2(l\ddot{\phi}_2\, s\phi_2 + l\dot{\phi}_2^2\, c\phi_2)] \\ &-(m_1 + m_2)\ddot{x}_1 - m_2 l\ddot{\phi}_2\, c\phi_2 + m_2 l\dot{\phi}_2^2\, s\phi_2 = -p_2.\end{aligned} \tag{2.34}$$

Using trigonometric transformations, it can be shown that

$$\left(\frac{c\alpha_2 - c\alpha_1}{s\alpha_1 + s\alpha_2}\right) = \tan\left(\frac{\alpha_1 - \alpha_2}{2}\right), \tag{2.35}$$

which can be inserted into Eq. (2.34) to give

$$\begin{aligned}&Mg\tan\left(\frac{\alpha_1 - \alpha_2}{2}\right) + m_2 l\ddot{\theta}_2\left[s\phi_2\tan\left(\frac{\alpha_1 - \alpha_2}{2}\right) - c\phi_2\right] \\ &+ m_2 l\dot{\phi}_2^2\left[\tan\left(\frac{\alpha_1 - \alpha_2}{2}\right)c\phi_2 + s\phi_2\right] \\ &+ M\tan\left(\frac{\alpha_1 - \alpha_2}{2}\right)\ddot{y}_1 - M\,\ddot{x}_1 = -p_2,\end{aligned} \tag{2.36}$$

where $M = (m_1 + m_2)$. The above equation can be simplified and rewritten as

$$
\begin{aligned}
& Mg\, s(\frac{\alpha_1-\alpha_2}{2}) - m_2 l\ddot{\theta}_2\, c(\phi_2+\frac{\alpha_1-\alpha_2}{2}) \\
& + m_2 l\dot{\phi}_2^2\, s(\phi_2+\frac{\alpha_1-\alpha_2}{2}) \\
& + M\ [s(\frac{\alpha_1-\alpha_2}{2})\,\ddot{y}_1 - c(\frac{\alpha_1-\alpha_2}{2})\,\ddot{x}_1] = -p_2\, c(\frac{\alpha_1-\alpha_2}{2}).
\end{aligned}
\tag{2.37}
$$

Using Eqs. (2.12, 2.13) to eliminate $\dot{L}_2$ and $\ddot{L}_2$ from Eqs. (2.21, 2.22), and substituting the result in Eq. (2.37) give the full nonlinear differential equation of m_1 as

$$
\begin{aligned}
& M\, s(\beta+\frac{\alpha_1-\alpha_2}{2})\ \ddot{w}_6 + M[L_4\, s(\psi+\frac{\alpha_1-\alpha_2}{2}) \\
& - \gamma_3 c(\frac{\alpha_1+\alpha_2}{2})]\ddot{\theta}_6 + M[L_3 s(\beta+\frac{\alpha_1-\alpha_2}{2}) + w_6 c(\beta+\frac{\alpha_1-\alpha_2}{2}) \\
& + L_4\, s(\psi+\frac{\alpha_1-\alpha_2}{2}) - \gamma_3 c(\frac{\alpha_1+\alpha_2}{2})]\,\ddot{\beta} + M\gamma_1\, c(\frac{\alpha_1+\alpha_2}{2})\,\ddot{L} \\
& + M\gamma_2\, c(\frac{\alpha_1+\alpha_2}{2})\,\ddot{D} + M[\gamma_3 c(\frac{\alpha_1+\alpha_2}{2}) - L_2 s(\frac{\alpha_1+\alpha_2}{2})]\ddot{\alpha}_2 \\
& - m_2 l\, c(\phi_2+\frac{\alpha_1-\alpha_2}{2})\ddot{\phi}_2 - Mc(\frac{\alpha_1-\alpha_2}{2})\ddot{x}_A + Ms(\frac{\alpha_1-\alpha_2}{2})\ddot{y}_A \\
& + Mg\, s(\frac{\alpha_1-\alpha_2}{2}) + m_2 l\dot{\phi}_2^2\, s(\phi_2+\frac{\alpha_1-\alpha_2}{2}) + Mf_2\, c(\frac{\alpha_1+\alpha_2}{2}) \\
& + 2M\dot{w}_6\dot{\beta}\, c(\beta+\frac{\alpha_1-\alpha_2}{2}) + ML_4\dot{\psi}^2\, c(\psi+\frac{\alpha_1-\alpha_2}{2}) \\
& + M\dot{\beta}^2[L_3 c(\beta+\frac{\alpha_1-\alpha_2}{2}) - w_6 s(\beta+\frac{\alpha_1-\alpha_2}{2})] \\
& - 2Ms(\frac{\alpha_1+\alpha_2}{2})\,\dot{\alpha}_2[\gamma_1\dot{L} + \gamma_2\dot{D} + \gamma_3\dot{\alpha}_2 - \gamma_3\dot{\psi}] \\
& - ML_2\dot{\alpha}_2^2 c(\frac{\alpha_1+\alpha_2}{2}) = -p_2\, c(\frac{\alpha_1-\alpha_2}{2}).
\end{aligned}
\tag{2.38}
$$

One important aspect to be mentioned here is that, choosing the angular coordinates α_1 and α_2 in describing the dynamic of the pulley results in an explicit and relatively short differential equation for m_1 (Eq. 2.38), which can be long if the Cartesian coordinates are used instead.

2.7 Dynamic of the rigid part of the boom

As shown in Fig. 2.1, the position of the center of gravity G of the rigid part BC with respect to the inertial reference frame O-$x_0y_0z_0$ can be represented as

$$\boldsymbol{G} = G_{x0}\,\boldsymbol{x}_0 + G_{y_0}\,\boldsymbol{y}_0, \tag{2.39}$$

where $\boldsymbol{x}_0$ and $\boldsymbol{y}_0$ are unit vectors in the directions x_0- and y_0- respectively, with

$$G_{x0} = x_A + L_3\,c\beta - w_6\,s\beta + \frac{L_4}{2}c\psi \tag{2.40}$$

$$G_{y_0} = y_A + L_3\,s\beta + w_6\,c\beta + \frac{L_4}{2}s\psi. \tag{2.41}$$

The component of the acceleration of point G in the lateral direction (y-direction) of the boom can be expressed as

$$\begin{aligned}\ddot{G}_y &= \ddot{G}_{y_0}\,c\beta - \ddot{G}_{x0}\,s\beta \\ &= -\ddot{x}_A\,s\beta + \ddot{y}_A\,c\beta + \ddot{w}_6 + \frac{L_4}{2}c\theta_6\,\ddot{\theta}_6 \\ &\quad + (L_3 + \frac{L_4}{2}c\theta_6)\,\ddot{\beta} - w_6\dot{\beta}^2 - \frac{L_4}{2}\dot{\psi}^2\,s\theta_6.\end{aligned} \tag{2.42}$$

Applying Newton's second law to member BC in the lateral direction gives

$$-Q_B - T\left[s(\alpha_1+\beta) + s(\alpha_2-\beta)\right] - m_{BC}g\,c\beta = m_{BC}\,\ddot{G}_y, \tag{2.43}$$

where m_{BC} denotes the mass of member BC, and Q_B denotes the shear force at point B. Substituting Eqs. (2.33) and (2.42) in Eq. (2.43) and utilizing the trigonometric transformation

$$\sin x + \sin y = 2\,s(\frac{x+y}{2})\,c(\frac{x-y}{2}), \tag{2.44}$$

yields

$$\begin{aligned}Q_B = &-m_{BC}[g\,c\beta - \ddot{x}_A\,s\beta + \ddot{y}_A\,c\beta + \ddot{w}_6 + 0.5L_4\,c\theta_6\,\ddot{\theta}_6 \\ &+ (L_3 + 0.5L_4c\theta_6)\ddot{\beta}] + m_{BC}w_6\dot{\beta}^2 + 0.5m_{BC}L_4\dot{\psi}^2 s\theta_6 \\ &+ H[M(g+\ddot{y}_1) + m_2 l\,(\ddot{\phi}_2\,s\phi_2 + \dot{\phi}_2^2\,c\phi_2)],\end{aligned} \tag{2.45}$$

with

$$H = s\beta \tan(\frac{\alpha_1 - \alpha_2}{2}) - c\beta. \tag{2.46}$$

By eliminating $\ddot{y}_1$ from Eq. (2.45), the explicit expression of the shear force at the boundary between the elastic and rigid parts can be expressed as

$$\begin{aligned} Q_B = & -[m_{BC} - MH\, c\beta]\ddot{w}_6 \\ & -[0.5 m_{BC} L_4 c\theta_6 - MH(L_4 c\psi + \gamma_3 s\alpha_2)]\ddot{\theta}_6 \\ & -[m_{BC}(L_3 + 0.5 L_4 c\theta_6) - MH(L_3 c\beta - w_6 s\beta + L_4 c\psi + \gamma_3 s\alpha_2)]\ddot{\beta} \\ & - MH\gamma_1 s\alpha_2 \ddot{L} - MH\gamma_2 s\alpha_2 \ddot{D} - MH[\gamma_3 s\alpha_2 + L_2 c\alpha_2]\ddot{\alpha}_2 \\ & + m_2 lH\, s\phi_2 \ddot{\phi}_2 + m_{BC}\, s\beta\, \ddot{x}_A + [MH - m_{BC}\, c\beta]\ddot{y}_A \\ & -[m_{BC}\, c\beta - MH]g + m_{BC}[w_6 \dot{\beta}^2 + 0.5 L_4 \dot{\psi}^2 s\theta_6] \\ & - MH[s\alpha_2\, f_2 + 2\dot{w}_6 \dot{\beta}\, s\beta + L_4 \dot{\psi}^2 s\psi \\ & + 2c\alpha_2\, \dot{\alpha}_2(\gamma_1 \dot{L} + \gamma_2 \dot{D} + \gamma_3 \dot{\alpha}_2 - \gamma_3 \dot{\psi}) - \dot{\alpha}_2^2 L_2\, s\alpha_2 \\ & + \dot{\beta}^2(L_3\, s\beta + w_6\, c\beta)] + m_2 lH \dot{\phi}_2^2\, c\phi_2. \end{aligned} \tag{2.47}$$

Similarly, the moment sum about point B (in counterclockwise direction) can be written in the form

$$\sum \boldsymbol{M}_B = I_{BC}\, \ddot{\psi}\, \boldsymbol{z}_0 + \boldsymbol{r}_{BG} \times m_{BC}\, (\ddot{G}_{x0}\, \boldsymbol{x}_0 + \ddot{G}_{y_0}\, \boldsymbol{y}_0), \tag{2.48}$$

with

$$\boldsymbol{r}_{BG} = 0.5 L_4\, (c\psi\, \boldsymbol{x}_0 + s\psi\, \boldsymbol{y}_0). \tag{2.49}$$

Therefore, the final expression of the bending moment at point B can be expressed as

$$\begin{aligned} M_B = & -[MP\, c\beta + 0.5 m_{BC} L_4 c\theta_6]\ddot{w}_6 \\ & -[I_{BC} + 0.25 m_{BC} L_4^2 + MP(L_4\, c\psi + \gamma_3\, s\alpha_2)]\ddot{\theta}_6 \\ & -[I_{BC} + 0.5 m_{BC} L_4 (L_3\, c\theta_6 + w_6\, s\theta_6 + 0.5 L_4) \\ & + MP(L_3\, c\beta - w_6\, s\beta + L_4\, c\psi + \gamma_3\, s\alpha_2)]\ddot{\beta} \\ & + MP\gamma_1 s\alpha_2\, \ddot{L} + MP\gamma_2 s\alpha_2 \ddot{D} + MP[\gamma_3 s\alpha_2 + L_2 c\alpha_2]\ddot{\alpha}_2 \\ & - m_2 lP\, s\phi_2\, \ddot{\phi}_2 + 0.5 m_{BC} L_4 s\psi\, \ddot{x}_A - [MP + 0.5 m_{BC} L_4 c\psi]\ddot{y}_A \\ & -[MP + 0.5 m_{BC} L_4 c\psi]g \end{aligned}$$

$$
\begin{aligned}
&-0.5 m_{BC} L_4 [2\dot{w}_6 \dot{\beta}\, s\theta_6 - \dot{\beta}^2 (w_6 c\theta_6 - L_3 s\theta_6)] \\
&+ MP[s\alpha_2\, f_2 + 2\dot{w}_6 \dot{\beta}\, s\beta + L_4 \dot{\psi}^2 s\psi + \dot{\beta}^2 (L_3\, s\beta + w_6\, c\beta) \\
&+ 2c\alpha_2\, \dot{\alpha}_2 (\gamma_1 \dot{L} + \gamma_2 \dot{D} + \gamma_3 \dot{\alpha}_2 - \gamma_3 \dot{\psi}) - \dot{\alpha}_2^2 L_2\, s\alpha_2] \\
&- m_2 lP\, \dot{\phi}_2^2\, c\phi_2 ,
\end{aligned}
\tag{2.50}
$$

with

$$
P = \frac{(L_4 - D)\, s(\alpha_1 + \psi) + L_4\, s(\alpha_2 - \psi)}{s\alpha_1 + s\alpha_2} . \tag{2.51}
$$

According to the free body diagram of the elastic part (Fig. 2.2), the calculated Q_B and M_B represent forces on the elastic boom which couple the dynamics of the elastic and rigid parts.

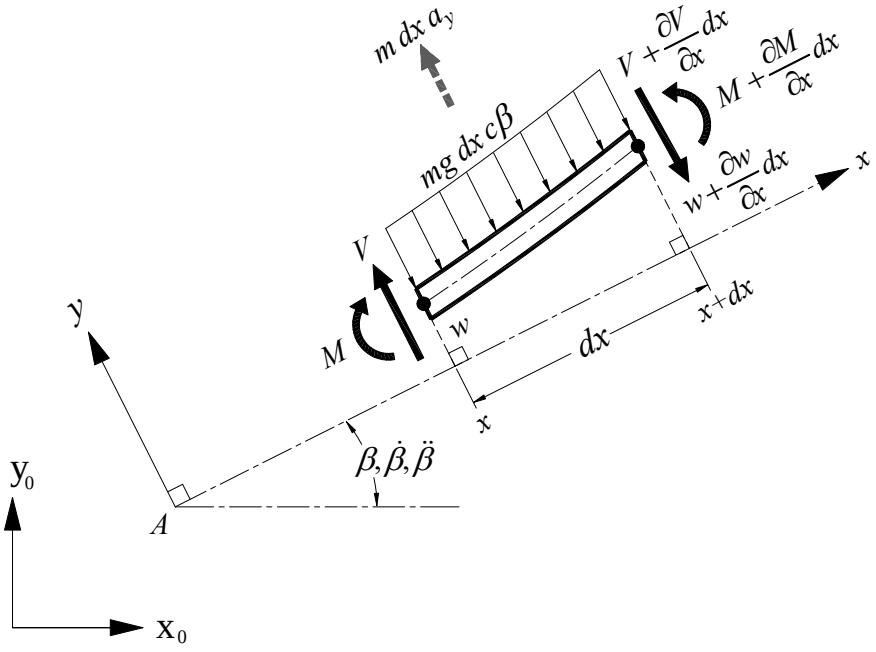

Figure 2.3: Geometry of a single boom element, all axial force components are neglected.

2.8 Dynamic of the elastic part of the boom

For deriving the finite element model of the elastic part (*AB*), the effects of rotary inertia, transverse shear deformation, and the axial force are neglected. Accordingly,

with reference to the single element shown in Fig. 2.3, the equation of motion in *y*-direction can be written as

$$\frac{\partial V}{\partial x} + ma_y = -mg\,c\beta\,. \tag{2.52}$$

Here m denotes the mass per unit length of the boom and a_y represents the absolute lateral acceleration of the element located at x, such that

$$a_y = \frac{\partial^2 w}{\partial t^2} + x\ddot{\beta} + \ddot{y}_A c\beta - \ddot{x}_A s\beta\,. \tag{2.53}$$

Substituting Eq. (2.53) into Eq. (2.52) and utilizing the relation

$$V = \frac{\partial}{\partial x}\left(EI\frac{\partial^2 w}{\partial x^2}\right) \tag{2.54}$$

yield

$$\frac{\partial^2}{\partial x^2}\left(EI\frac{\partial^2 w}{\partial x^2}\right) + m\frac{\partial^2 w}{\partial t^2} = p(x,t), \tag{2.55}$$

where

$$p(x,t) = -m\ddot{\beta}\,x - m[(g+\ddot{y}_A)c\beta - \ddot{x}_A\,s\beta] \tag{2.56}$$

represents the distributed lateral load acting on the part AB.

In Fig. 2.4 the free body diagram of a single finite element of length h is shown, the transverse displacement $w(\zeta)$ can be related to the node variables $(w_i, \theta_i, w_{i+1}, \theta_{i+1})$ through four cubic interpolation functions, such that

$$w(\zeta) = \boldsymbol{N}_e^T \boldsymbol{v}_e, \tag{2.57}$$

where

$$\boldsymbol{v}_e = [w_i\ \ \theta_i\ \ w_{i+1}\ \ \theta_{i+1}]^T, \tag{2.58}$$

is the node variables vector of order 4×1, and

$$\boldsymbol{N}_e = \begin{bmatrix} 1-3(\zeta/h)^2+2(\zeta/h)^3 \\ \zeta[1-(\zeta/h)]^2 \\ 3(\zeta/h)^2-2(\zeta/h)^3 \\ \zeta[(\zeta/h)^2-(\zeta/h)] \end{bmatrix}, \tag{2.59}$$

is the cubic interpolation functions vector of order 4×1 [Mei86], which is a typical method for the discritization of elastic continua.

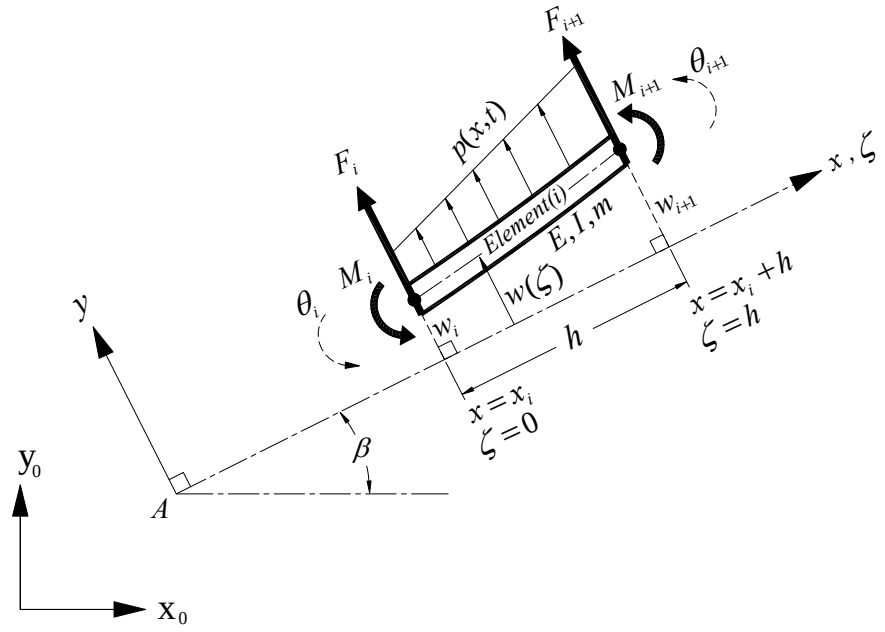

Figure 2.4: Single finite element

The element mass and stiffness matrices are defined as

$$\begin{aligned} \boldsymbol{M}_e &= \int_0^h m\,\boldsymbol{N}_e\,\boldsymbol{N}_e^T\,d\zeta, \\ &= \frac{mh}{420}\begin{bmatrix} 156 & 22h & 54 & -13h \\ 22h & 4h^2 & 13h & -3h^2 \\ 54 & 13h & 156 & -22h \\ -13h & -3h^2 & -22h & 4h^2 \end{bmatrix}, \end{aligned} \tag{2.60}$$

and

$$\boldsymbol{K}_e = \int_0^h EI\, \boldsymbol{N}_e'' \boldsymbol{N}_e''^T d\zeta,$$
$$= \frac{EI}{h^3}\begin{bmatrix} 12 & 6h & -12 & 6h \\ 6h & 4h^2 & -6h & 2h^2 \\ -12 & -6h & 12 & -6h \\ 6h & 2h^2 & -6h & 4h^2 \end{bmatrix}, \tag{2.61}$$

where $\boldsymbol{N}_e''$ denotes the second derivative of $\boldsymbol{N}_e$ with respect to the local coordinate ζ. Also, the element force vector (acting on the nodes i and i+1) can be also expressed as

$$\boldsymbol{f}_e = [F_i \;\; M_i \;\; F_{i+1} \;\; M_{i+1}]^T = \int_0^h p(x,t)\, \boldsymbol{N}_e\, d\zeta. \tag{2.62}$$

Since $p(x,t)$ varies linearly with the position (x) of the element, each element has a different force vector whose magnitude depends on the location of the element along the boom. Therefore, to calculate the integration in the right hand side of Eq. (2.62), equation (2.56) is rewritten as

$$p(x,t) = -m\ddot{\beta}\,(x_i + \zeta) - f_0, \tag{2.63}$$

with

$$f_0 = m[(g + \ddot{y}_A)c\beta - \ddot{x}_A s\beta], \tag{2.64}$$

where $0 \le \zeta \le h$ is the local longitudinal axis of the element, and x_i locates the element under consideration with respect to point A as shown in Fig. 2.4. Inserting Eq. (2.63) into Eq. (2.62) and carrying out the integration yield

$$\boldsymbol{f}_e = -\frac{h}{20}\begin{bmatrix} 10f_0 + m\ddot{\beta}\,(10x_i + 3h) \\ \frac{5}{3}hf_0 + \frac{mh}{3}\ddot{\beta}\,(5x_i + 2h) \\ 10f_0 + m\ddot{\beta}\,(10x_i + 7h) \\ -\frac{5}{3}hf_0 - \frac{mh}{3}\ddot{\beta}\,(5x_i + 3h) \end{bmatrix}. \tag{2.65}$$

By dividing the boom into five elements (i = 1,…,5), the mass matrix, the stiffness matrix, and the nodal force vector can be easily constructed by the assembling process [Mei86] to give the equations of motion that governs the elastic vibrations as

$$\boldsymbol{M}\,\ddot{\boldsymbol{v}} + \boldsymbol{K}\,\boldsymbol{v} = \boldsymbol{F}, \tag{2.66}$$

where $\boldsymbol{M}$ and $\boldsymbol{K}$ denote the 12×12 constant symmetric mass and stiffness matrices respectively, $\boldsymbol{F}$ denotes the 12×1 nodal force vector and

$$\boldsymbol{v} = [w_1 \quad \theta_1 \quad w_2 \quad \theta_2 \quad \cdots \quad w_6 \quad \theta_6]^T \tag{2.67}$$

is the 12×1 nodal displacement vector with w_i and θ_i representing the nodal translational and rotational displacements at node i with respect to the x-axis of the boom.

It is obvious that the total load vector ($\boldsymbol{F}$) is equal to the nodal force vector $\boldsymbol{f}$ resulting from the assembling process due to $p(x,t)$ plus the force vector $\boldsymbol{r}$ due to the external loads at the boundaries (A and B) of the boom (Fig. 2.2), i.e.

$$\boldsymbol{F} = \boldsymbol{f} + \boldsymbol{r}, \tag{2.68}$$

with

$$\boldsymbol{f} = -\frac{h}{20}\begin{bmatrix} 10f_0 + 3mh\ddot{\beta} \\ \frac{5}{3}hf_0 + \frac{2}{3}mh^2\ddot{\beta} \\ 20f_0 + 20mh\ddot{\beta} \\ \frac{4}{3}mh^2\ddot{\beta} \\ 20f_0 + 40mh\ddot{\beta} \\ \frac{4}{3}mh^2\ddot{\beta} \\ 20f_0 + 60mh\ddot{\beta} \\ \frac{4}{3}mh^2\ddot{\beta} \\ 20f_0 + 80mh\ddot{\beta} \\ \frac{4}{3}mh^2\ddot{\beta} \\ 10f_0 + 47mh\ddot{\beta} \\ -\frac{5}{3}hf_0 - \frac{23}{3}mh^2\ddot{\beta} \end{bmatrix}, \tag{2.69}$$

and

$$\boldsymbol{r} = [-Q_A \quad -M_A \quad 0 \quad 0 \quad 0 \quad 0 \quad 0 \quad 0 \quad 0 \quad 0 \quad Q_B \quad M_B]^T. \tag{2.70}$$

Because the boom is clamped at $x = 0$, the translational and rotational displacements must be zero, $w_1 = 0$ and $\theta_1 = 0$. Therefore, Eq. (2.66) can be partitioned to take the form

$$\begin{bmatrix} \boldsymbol{M}_{11} & \boldsymbol{M}_{12} \\ \boldsymbol{M}_{21} & \boldsymbol{M}_{22} \end{bmatrix} \begin{bmatrix} \ddot{\boldsymbol{v}}_1 \\ \ddot{\boldsymbol{v}}_2 \end{bmatrix} + \begin{bmatrix} \boldsymbol{K}_{11} & \boldsymbol{K}_{12} \\ \boldsymbol{K}_{21} & \boldsymbol{K}_{22} \end{bmatrix} \begin{bmatrix} \boldsymbol{v}_1 \\ \boldsymbol{v}_2 \end{bmatrix} = \begin{bmatrix} \boldsymbol{F}_1 \\ \boldsymbol{F}_2 \end{bmatrix}, \tag{2.71}$$

where

$$\boldsymbol{v}_1 = [w_1 \quad \theta_1]^T = [0 \quad 0]^T, \tag{2.72}$$

$$\boldsymbol{v}_2 = [w_2 \quad \theta_2 \quad \cdots \quad w_6 \quad \theta_6]^T. \tag{2.73}$$

In view of Eq. (2.71), the equations of motion of the boom can be expressed as

$$\boldsymbol{M}_{22}\ddot{\boldsymbol{v}}_2 + \boldsymbol{K}_{22}\boldsymbol{v}_2 = \boldsymbol{F}_2, \tag{2.74}$$

and the reaction force Q_A and the luff moment M_A at point A can be obtained from

$$\boldsymbol{M}_{12}\ddot{\boldsymbol{v}}_2 + \boldsymbol{K}_{12}\boldsymbol{v}_2 = \boldsymbol{F}_1. \tag{2.75}$$

Notice that, the force vector in Eq. (2.74) is coupled with the differential equations of m_1 and m_2 through the boundary reactions Q_B and M_B, which are expressed previously in their final nonlinear form in Eqs. (2.47 and 2.50). These two equations can be used to eliminate Q_B and M_B from Eq. (2.74), which in conjunction with Eqs. (2.38) and (2.30) represent the coupled nonlinear equations of motion of the complete crane. The variables $\beta(t)$, x_A, and y_A with their time derivatives can be eliminated By using Eqs. (2.5, 2.19 and 2.20). This yields that, the equations of motion of the crane contain the variables $\rho(t)$, $L(t)$, and $D(t)$ as control inputs to control the vibrations of the crane and payload resulting from the disturbance inputs $\Delta\delta(t)$ and $p_2(t)$. Notice also that in view of Eqs. (2.15, 2.16, 2.23 and 2.24), and with the knowledge of $w_6, \theta_6, \alpha_2, \phi_2, \Delta\delta$ and the three control inputs; the position of m_1 and m_2 with respect to the center of the ship can be easily computed.

2.9 Derivation of the equilibrium point

At the current equilibrium point, it is clear that

$$\begin{aligned} &\alpha_{10} = \alpha_{20} \\ &\phi_{20} = 0, \end{aligned} \tag{2.76}$$

and the elastic translational and rotational displacements vector $\boldsymbol{v}_0$ can be computed from Eq. (2.66) by setting $\ddot{\boldsymbol{v}}$ and the time dependent terms in $\boldsymbol{F}$ equal to zero, i.e.

$$\boldsymbol{v}_0 = \boldsymbol{K}^{-1}\boldsymbol{F}_0. \tag{2.77}$$

Inserting Eq. (2.76) into Eq. (2.3), the magnitude of α_{20} can be expressed as

$$\alpha_{20} = \cos^{-1}\left(\frac{D_0}{L_0} c\psi_0\right), \tag{2.78}$$

where

$$\psi_0 = \beta_0 + \theta_{60}. \tag{2.79}$$

2.10 Expanding the model about the current equilibrium point

To study the obtained nonlinear model, Taylor series is utilized to expand the nonlinear terms about the equilibrium point, which is characterized by Eqs. (2.76-79). Then, by keeping only the linear and quadratic terms, the equations of motion of the crane can be written in the form

$$\boldsymbol{M}_0\ddot{\boldsymbol{q}} + \boldsymbol{K}_0\boldsymbol{q} = \boldsymbol{B}_1\boldsymbol{u} + \boldsymbol{B}_2\ddot{\boldsymbol{u}} + \boldsymbol{B}_3\Delta\delta + \boldsymbol{B}_4\Delta\ddot{\delta} + \boldsymbol{B}_5 p_2 + \boldsymbol{n}, \tag{2.80}$$

where

$$\boldsymbol{q} = [\Delta w_2 \quad \Delta\theta_2 \quad \cdots \quad \Delta w_6 \quad \Delta\theta_6 \quad \Delta\alpha_2 \quad \Delta\phi_2]^T \tag{2.81}$$

denotes the 12×1 generalized displacement vector, and

$$\boldsymbol{u} = [\Delta\rho \quad \Delta L \quad \Delta D]^T \tag{2.82}$$

represents the control input vector, $\boldsymbol{M}_0$ and $\boldsymbol{K}_0$ are the total mass and stiffness matrices respectively of order 12×12, $\boldsymbol{B}_1$ and $\boldsymbol{B}_2$ are input matrices of order 12×3, $\boldsymbol{B}_3$, $\boldsymbol{B}_4$ and $\boldsymbol{B}_5$ are disturbance matrices of order 12×1, and all quadratic terms are collected in the vector $\boldsymbol{n}$. The structure of $\boldsymbol{M}_0$, $\boldsymbol{K}_0$, $\boldsymbol{B}_1$, $\boldsymbol{B}_2$, $\boldsymbol{B}_3$, $\boldsymbol{B}_4$, and $\boldsymbol{B}_5$ is not explicitly described for the sake of conciseness.

The measurement vector $\boldsymbol{y}_\mathrm{m}$ and the interested outputs $\boldsymbol{y}$ are specified as

$$\begin{aligned}\boldsymbol{y}_\mathrm{m} &= [\Delta\theta_6 \quad \Delta\alpha_2 \quad \Delta\phi_2]^T \\ &= \boldsymbol{C}_1\boldsymbol{q},\end{aligned} \tag{2.83}$$

and

$$\boldsymbol{y} = [x_2 \quad y_2]^T = \boldsymbol{f}(\boldsymbol{q}, \boldsymbol{u}, \Delta\delta), \tag{2.84}$$

where $\boldsymbol{C}_1$ is the measurement matrix of order 3×12; it describes the position of the sensors on the crane.

The idea behind writing the equations of motion in the form given in Eq. (2.80) is to separate the nonlinear terms in order to find if their influence on the dynamic behavior of the crane can be neglected. This is checked by simulations for different operating conditions and different initial conditions.

2.11 Analysis and simulation results

2.11.1 Studying the influence of the variables L and D on the equilibrium position of the payload

The equilibrium position of the payload with respect to the roll center of the crane can be calculated from Eqs. (2.23) and (2.24) as

$$x_{20} = x_{A0} + L_3\, c\beta_0 - w_{60}\, s\beta_0 + L_4\, c\psi_0 - L_{20}\, c\alpha_{20} \tag{2.85}$$

$$y_{20} = y_{A0} + L_3\, s\beta_0 + w_{60}\, c\beta_0 + L_4\, s\psi_0 - L_{20}\, s\alpha_{20} - l, \tag{2.86}$$

where L_{20} can be computed from Eq. (2.11) as

$$L_{20} = \frac{1}{2}\left(\frac{L_0^2 - D_0^2}{L_0 - D_0\, c(\alpha_{20} - \psi_0)}\right), \tag{2.87}$$

and x_{20} and y_{20} can be calculated from Eqs. (2.19, 2.20) as

$$\begin{aligned} x_{A0} &= L_5\, c\delta_0 \\ y_{A0} &= L_5\, s\delta_0 . \end{aligned} \tag{2.88}$$

The influence of the inputs on displacing the equilibrium position of the payload is investigated by simulation on a scaled test rig with 1.5 meter boom. In Figs. 2.5 and 2.6 the influence of the variables L and D on displacing the equilibrium position of the payload for different values of β is illustrated. It can be recognized from Figure 2.5 that for all possible values of β, changing L can efficiently displace y_{20}, with a negligible effect on x_{20}. In addition, it can be noted from Figure 2.6 that for $\beta < 1.0$ rad., which is the normal operating range of the crane, the input D can change x_{20} considerably with a little effect on y_{20}. Therefore, it can be shown that the variable D can be used efficiently to control the horizontal coordinate x_2, whereas, the variable L can be employed to control the vertical coordinate y_2

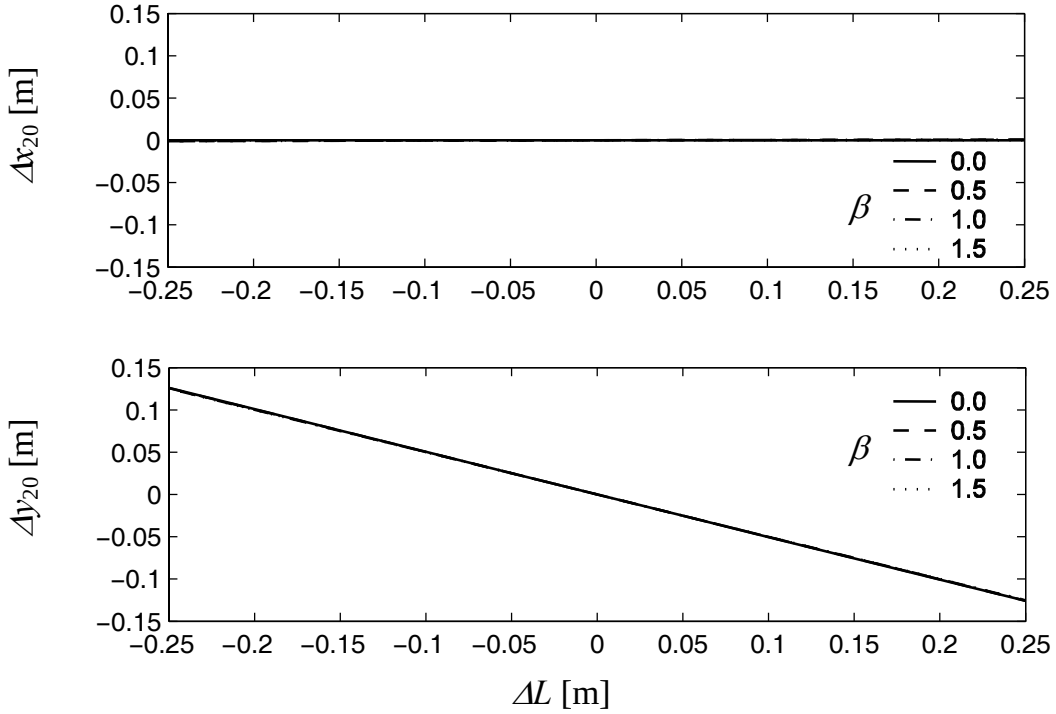

Figure 2.5: Effect of changing L on the equilibrium position of the payload for different β

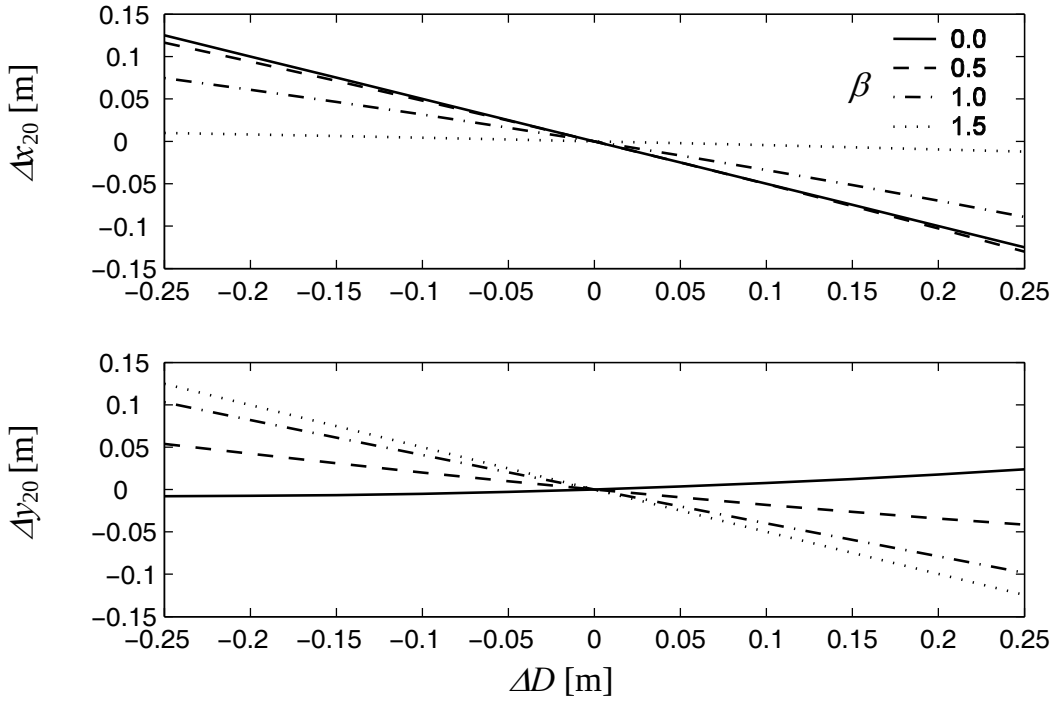

Figure 2.6: Effect of changing D on the equilibrium position of the payload for different β

2.11.2 Effect of the nonlinear terms on the simulation results

To examine the effect of the nonlinear terms on the response of the crane in the operating range, the model is simulated for different values of β and L such that, in the first step, the full nonlinear model is simulated for typical initial conditions and base excitations. In the next step, the nonlinear terms in $\boldsymbol{n}$ are eliminated and simulations are conducted again to find their influence on the overall response. Simulation results showed that within considerable operating range and amplitudes of the generalized displacements in the neighborhood of the current equilibrium point, the response using the nonlinear model is close to the response of the linear model obtained by eliminating all nonlinear terms, i.e., by setting $\boldsymbol{n} = \mathbf{0}$. As a sample of these results, Fig. 2.7 illustrates the responses of the linear and nonlinear model for $\beta = \pi/4$ and an initial velocity of $\dot{\phi}_2(0) = 5\,\text{rad/s}$. It can be noted that the response of the linear model coincides with that of the nonlinear one with only a small difference, observed in the elastic displacements (as shown in w_6 and θ_6); this small difference can be ignored in the control system design process due to the complexity that may be introduced by considering such small nonlinear effects.

In Fig. 2.8, the linear and nonlinear responses due to 3.0° sinusoidal rolling excitation in the neighborhood of the first eigenfrequency of the crane are shown, it is noted that the obtained results highlight those obtained previously in the free vibration case, i.e., the nonlinear terms have no significant effect on the response. Therefore, it is obvious that with strong controllability of the crane, the linearized model can be used to design the control law. This will be considered in detail in the next chapter.

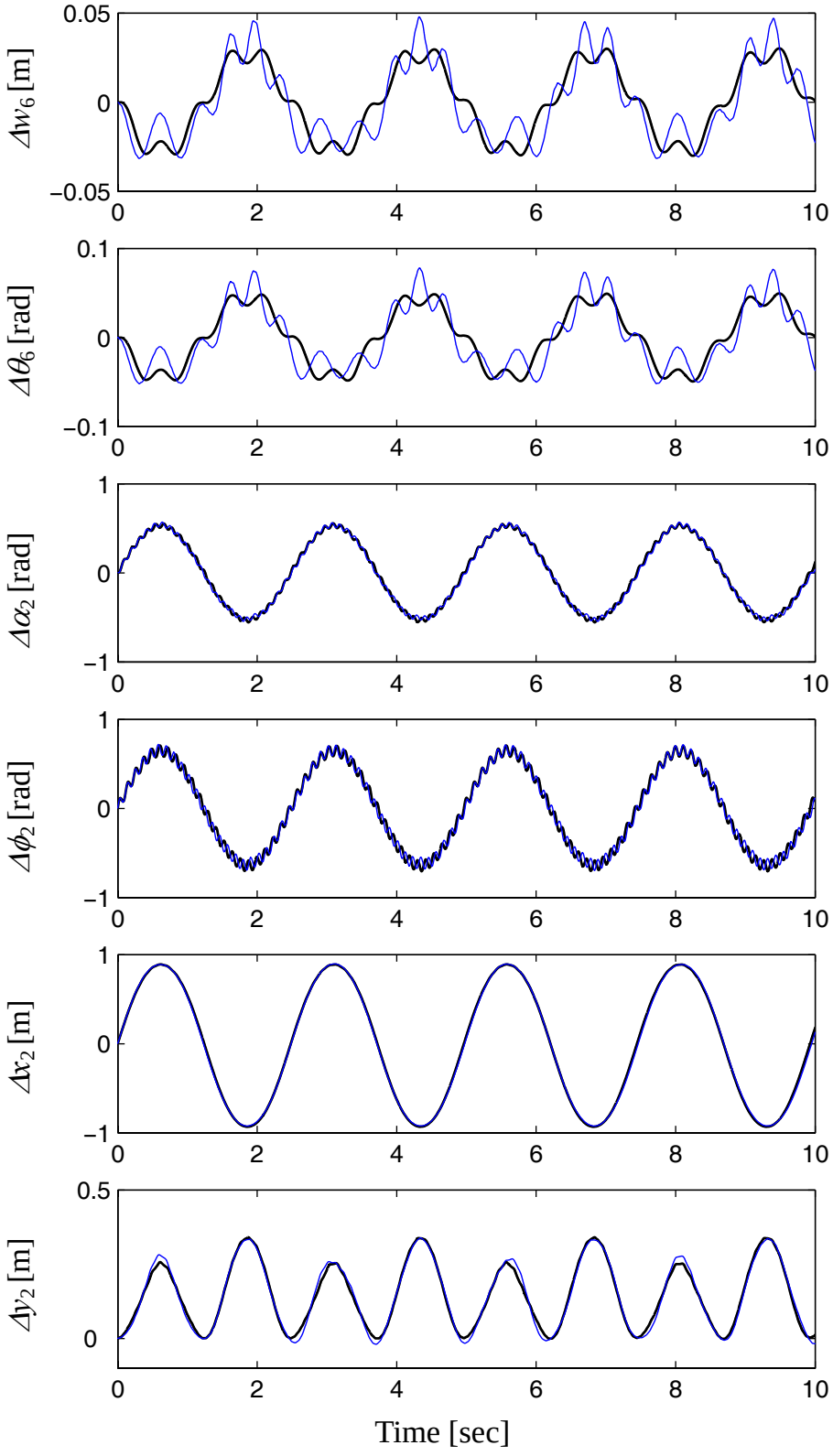

Figure 2.7: Response of the payload and the tip of the elastic boom for $\dot{\phi}_2(0) = 5\,\text{rad/s}$, $\beta = \pi/4$.

— nonlinear, — linear.

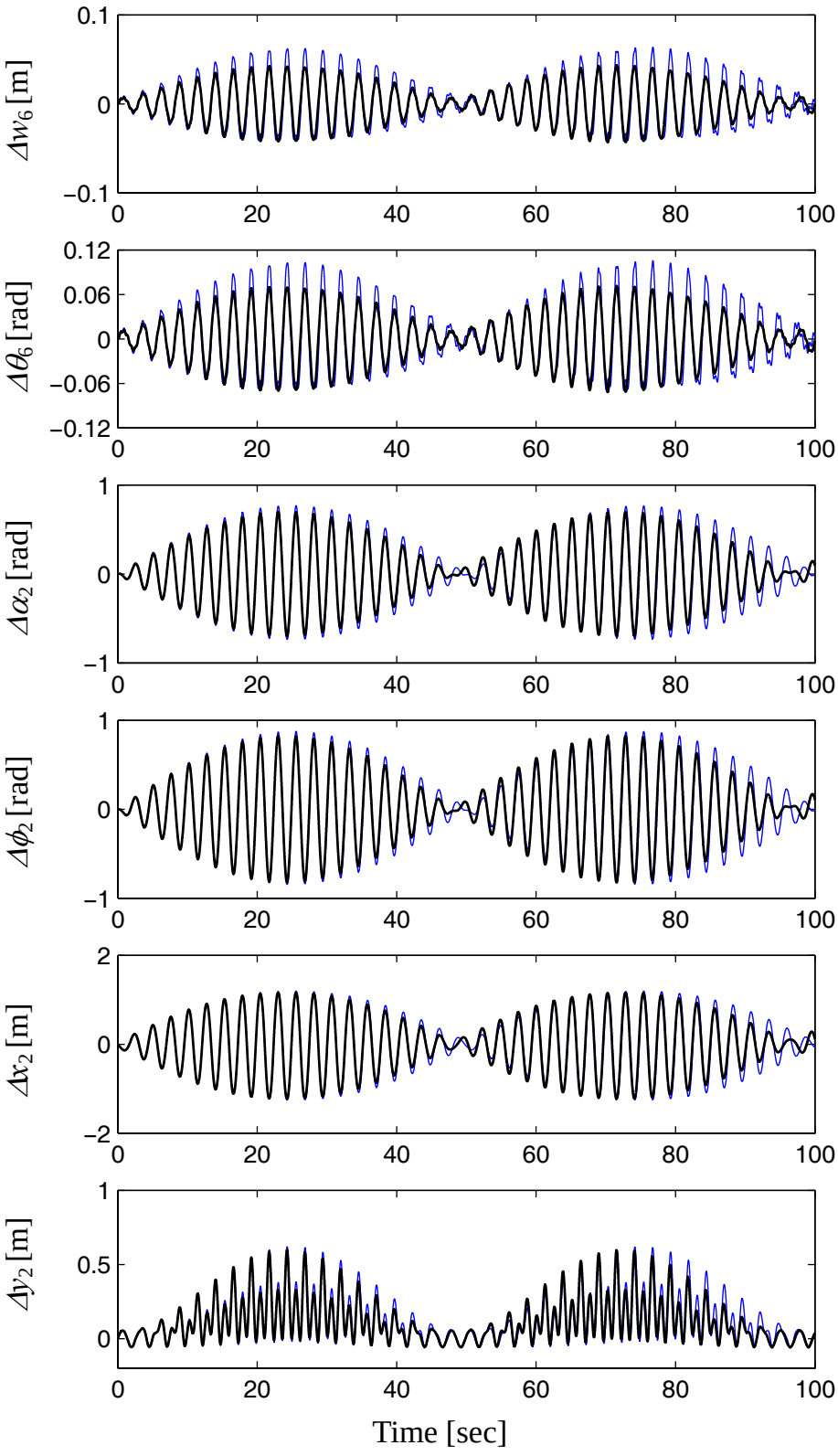

Figure 2.8: Response of the payload and the tip of the elastic boom due to rolling excitation in the neighborhood of the first eigenfrequency. Rolling amplitude = 3.0°, $\beta = \pi/4$.
— nonlinear, — linear.

3 Control system design

3.1 Introduction

This chapter presents the observer and controller design in order to minimize the pendulation of the payload which can be induced from ship rolling or from any other disturbance that can act on the crane during the cargo transfer operation. When the frequency of the ship rolling is close to the eigenfrequency of the crane for a period of time, resonance will occur and the pendulation of the payload can grow to a dangerous level even with small amplitude of the disturbing rolling motion. This means that, if no control is used, the operation of the crane should be suspended. This control problem is explained in detail in this chapter.

3.2 State space representation

The linear equations of motion of the crane, obtained by setting $\boldsymbol{n} = \mathbf{0}$ in Eq. (2.80), can be rewritten as

$$\boldsymbol{M}_0\ddot{\boldsymbol{q}} - \boldsymbol{B}_2\ddot{\boldsymbol{u}} - \boldsymbol{B}_4\Delta\ddot{\delta} = -\boldsymbol{K}_0\boldsymbol{q} + \boldsymbol{B}_1\boldsymbol{u} + \boldsymbol{B}_3\Delta\delta + \boldsymbol{B}_5 p_2 . \tag{3.1}$$

To obtain the state space model for the above equation, let

$$z_1 = \boldsymbol{M}_0\boldsymbol{q} - \boldsymbol{B}_2\boldsymbol{u} - \boldsymbol{B}_4\Delta\delta \tag{3.2}$$

$$z_2 = \boldsymbol{M}_0\dot{\boldsymbol{q}} - \boldsymbol{B}_2\dot{\boldsymbol{u}} - \boldsymbol{B}_4\Delta\dot{\delta}. \tag{3.3}$$

Then the state space equations, corresponding to the current equilibrium point, can be expressed in vector form as

$$\dot{\boldsymbol{z}} = \boldsymbol{A}\boldsymbol{z} + \boldsymbol{B}\boldsymbol{u} + \boldsymbol{E}\Delta\delta + \boldsymbol{N}p_2, \tag{3.4}$$

where

$$\boldsymbol{z} = [z_1 \quad z_2]^T \tag{3.5}$$

denotes the state vector of order 24×1, and

$$\boldsymbol{A} = \begin{bmatrix} \mathbf{0} & \boldsymbol{I} \\ -\boldsymbol{K}_0\boldsymbol{M}_0^{-1} & \mathbf{0} \end{bmatrix}, \tag{3.6}$$

$$\boldsymbol{B} = \begin{bmatrix} \mathbf{0} \\ \boldsymbol{B}_1 - \boldsymbol{K}_0 \boldsymbol{M}_0^{-1} \boldsymbol{B}_2 \end{bmatrix}, \tag{3.7}$$

represent the corresponding system and input matrices respectively, and

$$\boldsymbol{E} = \begin{bmatrix} \mathbf{0} \\ \boldsymbol{B}_3 - \boldsymbol{K}_0 \boldsymbol{M}_0^{-1} \boldsymbol{B}_4 \end{bmatrix}, \tag{3.8}$$

$$\boldsymbol{N} = \begin{bmatrix} \mathbf{0} \\ \boldsymbol{B}_5 \end{bmatrix}, \tag{3.9}$$

represent the disturbance matrices due to ship rolling and disturbance force acting on the payload respectively. Here $\boldsymbol{M}_0$ is assumed to be non-singular.

In view of Eqs. (3.2, 3.3), the initial conditions of the states can be expressed as

$$z(0) = \begin{bmatrix} \boldsymbol{M}_0 & \mathbf{0} \\ \mathbf{0} & \boldsymbol{M}_0 \end{bmatrix} \begin{bmatrix} \boldsymbol{q}(0) \\ \dot{\boldsymbol{q}}(0) \end{bmatrix} - \begin{bmatrix} \boldsymbol{B}_2 & \mathbf{0} \\ \mathbf{0} & \boldsymbol{B}_2 \end{bmatrix} \begin{bmatrix} \boldsymbol{u}(0) \\ \dot{\boldsymbol{u}}(0) \end{bmatrix} - \begin{bmatrix} \boldsymbol{B}_4 & \mathbf{0} \\ \mathbf{0} & \boldsymbol{B}_4 \end{bmatrix} \begin{bmatrix} \Delta\delta(0) \\ \Delta\dot{\delta}(0) \end{bmatrix}. \tag{3.10}$$

The displacement vector $\boldsymbol{q}$ can be obtained from Eq. (3.2) as

$$\begin{aligned} \boldsymbol{q} &= \boldsymbol{M}_0^{-1} \boldsymbol{z}_1 + \boldsymbol{M}_0^{-1} \boldsymbol{B}_2 \boldsymbol{u} + \boldsymbol{M}_0^{-1} \boldsymbol{B}_4 \Delta\delta \\ &= [\boldsymbol{M}_0^{-1} \quad \mathbf{0}]\, \boldsymbol{z} + \boldsymbol{M}_0^{-1} \boldsymbol{B}_2 \boldsymbol{u} + \boldsymbol{M}_0^{-1} \boldsymbol{B}_4 \Delta\delta. \end{aligned} \tag{3.11}$$

Therefore, the measurements $\boldsymbol{y}_{\mathrm{m}}$, given by Eq. (2.83), can be written as

$$\boldsymbol{y}_{\mathrm{m}} = \boldsymbol{C}\boldsymbol{z} + \boldsymbol{D}\boldsymbol{u} + \boldsymbol{F}\Delta\delta\,, \tag{3.12}$$

where

$$\boldsymbol{C} = [\boldsymbol{C}_1 \boldsymbol{M}_0^{-1} \quad \mathbf{0}] \tag{3.13}$$

denotes the output matrix, and

$$\boldsymbol{D} = \boldsymbol{C}_1 \boldsymbol{M}_0^{-1} \boldsymbol{B}_2\,, \tag{3.14}$$

$$\boldsymbol{F} = \boldsymbol{C}_1 \boldsymbol{M}_0^{-1} \boldsymbol{B}_4\,, \tag{3.15}$$

represent the input and disturbance direct transmission matrices respectively. Here the rolling motion of the ship $\Delta\delta(t)$ is assumed to be measured.

3.3 State and disturbance estimation

In order to design an optimal state feedback controller, all state variables must be achievable. In most cases, as it is seen in the ship crane under consideration, not all the state variables are measured since the required sensors are not available due to economic or practical reasons. Only 3 out of 24 states can be easily measured. In order to reconstruct the entire state vector $\boldsymbol{z}$, a suitable observer can to be designed as a first step to realize optimal state controller design if the related conditions for applications are fulfilled. Since the state space model of the crane contains the unknown disturbance force p_2, the state variables and the unknown disturbance can be estimated by using a special observer design able to reconstruct system states in presence of additional unknown effects acting on the system. Here a Proportional-Integral Observer (PI-Observer) [Mül98, SYM95, SBM93] could be used. The structure of this observer is shown in Fig. 3.1. The estimated states are represented by the equations

$$\dot{\hat{\boldsymbol{z}}} = \boldsymbol{A}\hat{\boldsymbol{z}} + \boldsymbol{B}\boldsymbol{u} + \boldsymbol{E}\Delta\delta + \boldsymbol{N}\hat{p}_2 + \boldsymbol{L}_1(\boldsymbol{y}_m - \hat{\boldsymbol{y}}_m), \tag{3.16}$$

and the unknown disturbance is reconstructed by

$$\dot{\hat{p}}_2 = G\,\hat{p}_2 + \boldsymbol{L}_2(\boldsymbol{y}_m - \hat{\boldsymbol{y}}_m), \tag{3.17}$$

where $\hat{\boldsymbol{y}}_m$ is the output of the observer, $\boldsymbol{L}_1$ and $\boldsymbol{L}_2$ are the observer gain matrices of appropriate dimensions. Due to the difficulty of finding a simple linear model that can adequately describe the unknown disturbance, which is principally unknown, a suitable design procedure is necessary. Since any continuous signal can be approximated by a series of step functions, a practical choice for the linear model corresponding to the estimate of p_2 is a stepwise-constant approximation; $G = 0$. If the signal is fast, then the observer dynamics should be also fast for the approximation to hold. Since the main expected cause of p_2 is the wind force, which usually has a low frequency, the disturbance can be estimated adequately without the need to use a relatively high gain approach. Therefore, the modified extended model can be written as

$$\begin{bmatrix} \dot{\hat{\boldsymbol{z}}} \\ \dot{\hat{p}}_2 \end{bmatrix} = \underbrace{\begin{bmatrix} \boldsymbol{A} & \boldsymbol{N} \\ \boldsymbol{0} & 0 \end{bmatrix}}_{\boldsymbol{A}_e} \begin{bmatrix} \hat{\boldsymbol{z}} \\ \hat{p}_2 \end{bmatrix} + \underbrace{\begin{bmatrix} \boldsymbol{B} \\ \boldsymbol{0} \end{bmatrix}}_{\boldsymbol{B}_e} \boldsymbol{u} + \underbrace{\begin{bmatrix} \boldsymbol{E} \\ 0 \end{bmatrix}}_{\boldsymbol{E}_e} \Delta\delta + \underbrace{\begin{bmatrix} \boldsymbol{L}_1 \\ \boldsymbol{L}_2 \end{bmatrix}}_{\boldsymbol{L}_e} (\boldsymbol{y}_m - \hat{\boldsymbol{y}}_m), \tag{3.18}$$

with

$$\hat{\boldsymbol{y}}_{\mathrm{m}} = \underbrace{[\boldsymbol{C} \quad \boldsymbol{0}]}_{\boldsymbol{C}_e} \begin{bmatrix} \hat{\boldsymbol{z}} \\ \hat{p}_2 \end{bmatrix} + \boldsymbol{D}\boldsymbol{u} + \boldsymbol{F}\Delta\delta. \tag{3.19}$$

This model gives the base for the PI-Observer development [SBM93, KS105, KS205]. It is necessary that the extended system is observable, i.e.,

$$\operatorname{rank} \begin{bmatrix} \lambda_i \boldsymbol{I} - \boldsymbol{A}_e \\ \boldsymbol{C}_e \end{bmatrix} = \dim(\boldsymbol{z}) + \dim(p_2) \tag{3.20}$$

is satisfied for all eigenvalues λ_i of the system. According to Eqs. (3.4 and 3.18), the error dynamics of the extended observer can be expressed by

$$\dot{\boldsymbol{e}} = (\boldsymbol{A}_e - \boldsymbol{L}_e \boldsymbol{C}_e)\boldsymbol{e} - \boldsymbol{J}\dot{p}_2, \tag{3.21}$$

where

$$\boldsymbol{e} = \begin{bmatrix} \boldsymbol{z} \\ p_2 \end{bmatrix} - \begin{bmatrix} \hat{\boldsymbol{z}} \\ \hat{p}_2 \end{bmatrix} \tag{3.22}$$

denotes the error vector of the extended observer, and

$$\boldsymbol{J} = \begin{bmatrix} \boldsymbol{0} \\ 1 \end{bmatrix} \tag{3.23}$$

represents an input matrix to the error equation. It can be seen from Eq. (3.21) that $\dot{p}_2$ tends to produce a nonzero steady state error vector. This tendency is considerable if the disturbance signal coming from the wind represents a fast dynamics. In reality, wind effects acting as disturbances usually has low frequency, which means that the effect of its time derivative on the error equation is not significant especially if the eigenvalue of the error equation corresponding to the estimated disturbance is very fast in comparison to the remaining eigenvalues. There are many different design techniques used to design the observer gain matrices. Here the gains are found by minimizing a linear quadratic performance index, which leads to solving the algebraic Riccati equation

$$\boldsymbol{A}_e \boldsymbol{P} + \boldsymbol{P}\boldsymbol{A}_e^T + \boldsymbol{Q}_e - \boldsymbol{P}\boldsymbol{C}_e^T \boldsymbol{R}_e^{-1} \boldsymbol{C}_e \boldsymbol{P} = \boldsymbol{0}. \tag{3.24}$$

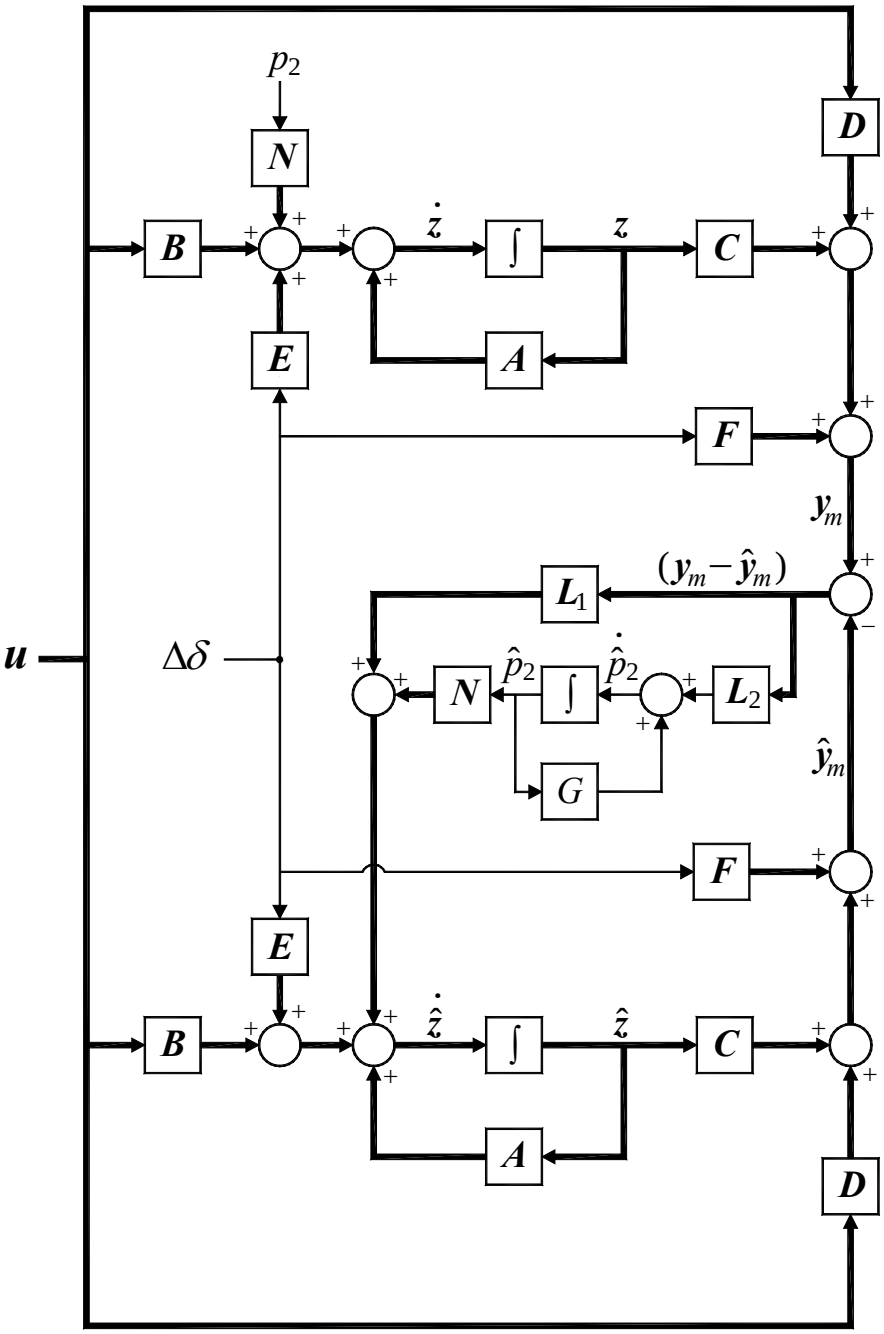

Figure 3.1: Structure of the PI-Observer corresponding to the crane linear model

The gain matrix of the observer is calculated by

$$\boldsymbol{L}_e = \boldsymbol{P}\boldsymbol{C}_e^T \boldsymbol{R}_e^{-1}. \tag{3.25}$$

where $\boldsymbol{Q}_e$ and $\boldsymbol{R}_e$ are symmetric positive definite weighting matrices for the extended states and the measurements respectively.

One important point to be mentioned here is that the estimation error corresponding to the last state $\hat{p}_2$ has to be weighted much more than the other 24 states, i.e., the observer eigenvalue corresponding to last state should be far to the left of the other eigenvalues in the complex plane. All other eigenvalues are weighted such that the observer is asymptotically stable and sufficiently faster than the real passive system. This guarantees that the observer error converges to zero in real time, which means that the estimates converge to their real values in real time and are ready for the implementation of an optimal state feedback controller; this strategy is successfully used for fault diagnosis of large systems [SBM93] and other engineering applications [SYM95,KS105].

Simulation results for an actual disturbance signal p_2 in addition to the actual displacements ($\Delta w_6, \Delta\theta_6, \Delta\alpha_2, \Delta\phi_2$) and their time derivatives are shown together with their estimation values in Fig. 3.2. Here the results are based on the dimensions of a scaled test rig (Boom length =1.5 m, L = 1.5 m, L_5 = 0.42 m, l = 0.5 m, m_2 = 5 kg, and m_1 = $0.01m_2$, $\delta_0 = \pi/4$) subjected to the disturbance force p_2 with nonzero initial condition. The initial conditions of the observer are set to zero and the actual initial condition vector of the original system is characterized by $\phi_2(0) = 1.0$ rad. Note that the error of the observer due to the difference in the initial conditions disappears in the first second, and the observer estimates the disturbance and the states very well. In Fig. 3.3, the payload is subjected to a disturbance force of variable frequency, it can also be noted that the observer gives an acceptable estimation of the fast disturbance.

It is clear from Eqs. (3.24 and 3.25) that the observer gain matrix $\boldsymbol{L}_e$ depends directly on the extended system matrix $\boldsymbol{A}_e$ in addition to the measurement matrix $\boldsymbol{C}_e$ which represent together with the weighting matrices $\boldsymbol{Q}_e$ and $\boldsymbol{R}_e$ the parameters of the Ricatti equation. Also, the matrix $\boldsymbol{A}_e$ depends on the system matrix $\boldsymbol{A}$ which is governed by the mass matrix $\boldsymbol{M}_0$ and the stiffness matrix $\boldsymbol{K}_0$. Since $\boldsymbol{M}_0$ and $\boldsymbol{K}_0$ are calculated at the current equilibrium point, which varies with the length of the cable L_0 and the boom luff angle ρ_0, the observer gain matrix $\boldsymbol{L}_e$ must be updated according to the current operating point. This leads to the concept of developing a variable-gain extended observer which can cover all possible operating equilibrium points of the crane.

To simplify the design of such an observer, and to reduce the mathematical computations that can be involved in regenerating the gain matrix $\boldsymbol{L}_e$, the length of the cable is divided into four ranges and the luff angle is divided into three ranges as shown in Fig. 3.4, where for the scaled model under consideration, the length of the

cable (in meters) and the luff angle (in degrees) are divided such that L_{0r}=1+0.5r, r= 0,⋯,4 and ρ_{0s}=15+20s, s = 0,⋯,3. This results in $3\times 4=12$ operating regions; each operating region is characterized by an integer number i that governs the calculation of the corresponding gain matrix $\boldsymbol{L}_e$. This yields that, the operation of the crane is covered by different observer gain matrices $(\boldsymbol{L}_e)_i$. The switching between these gains takes place automatically according to the output (i) of the region finder (Fig. 3.5), which uses the measurements of the luff angle and the length of the cable to detect the current operating region. An important question arise here: At which point inside the region the gain should be calculated? Is it at the center of the region or at some other point inside the region? And what factor governs the selection of this point? This discussion will be given in section 3.5.

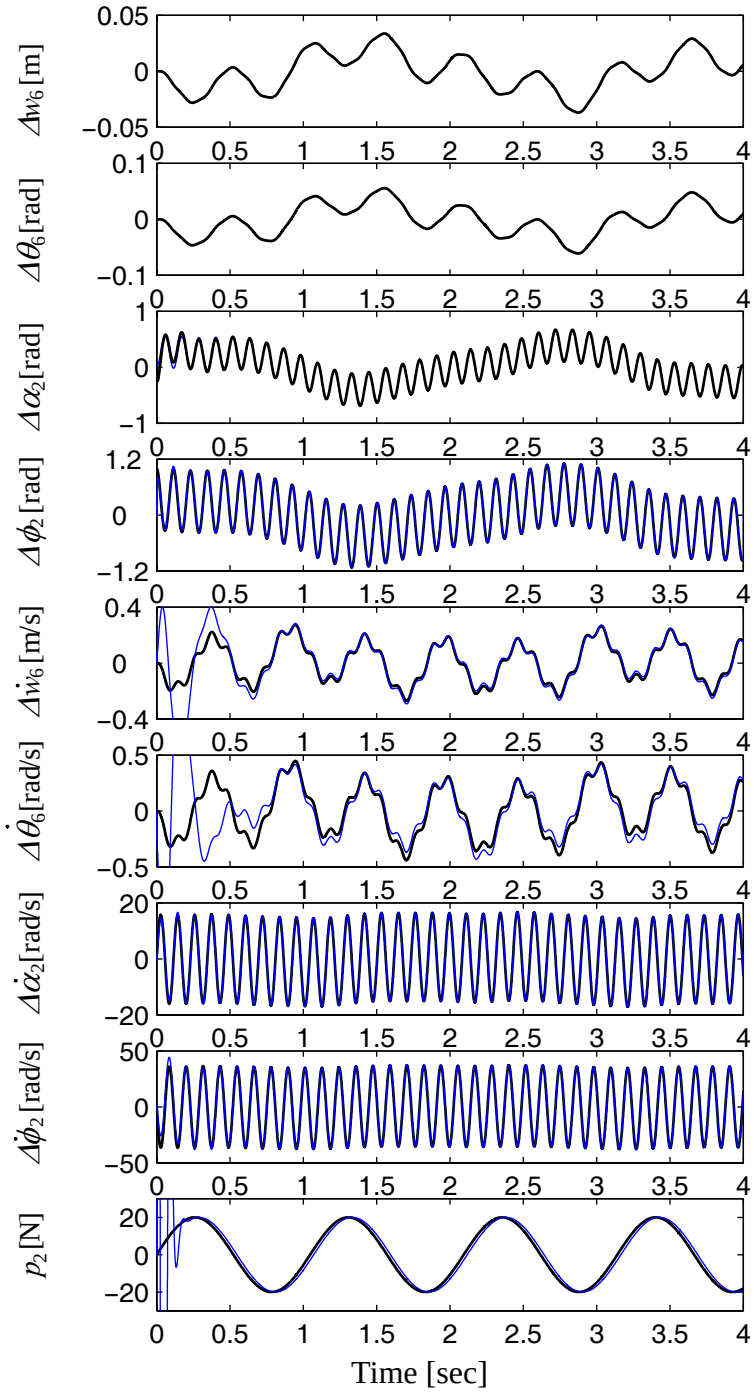

Figure 3.2: Simulation results for actual states and their estimations $\rho_0 = \pi/4$, — actual value, — estimated value.

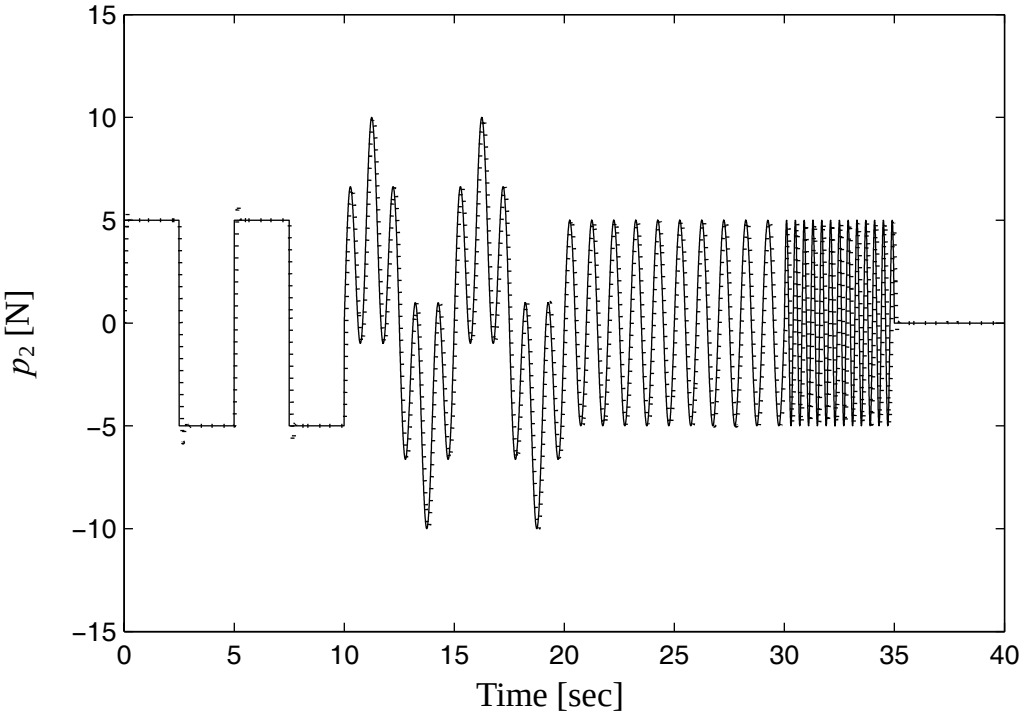

Figure 3.3: Comparison between actual and estimated disturbance force acting on the payload, $\rho_0 = \pi/4$, — actual value, ···· estimated value.

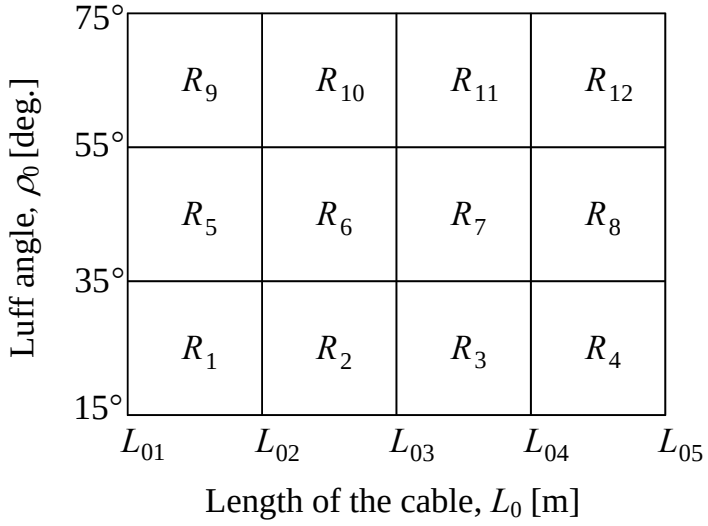

Figure 3.4: Operating regions (R_i), $i = 1, \cdots, 12$

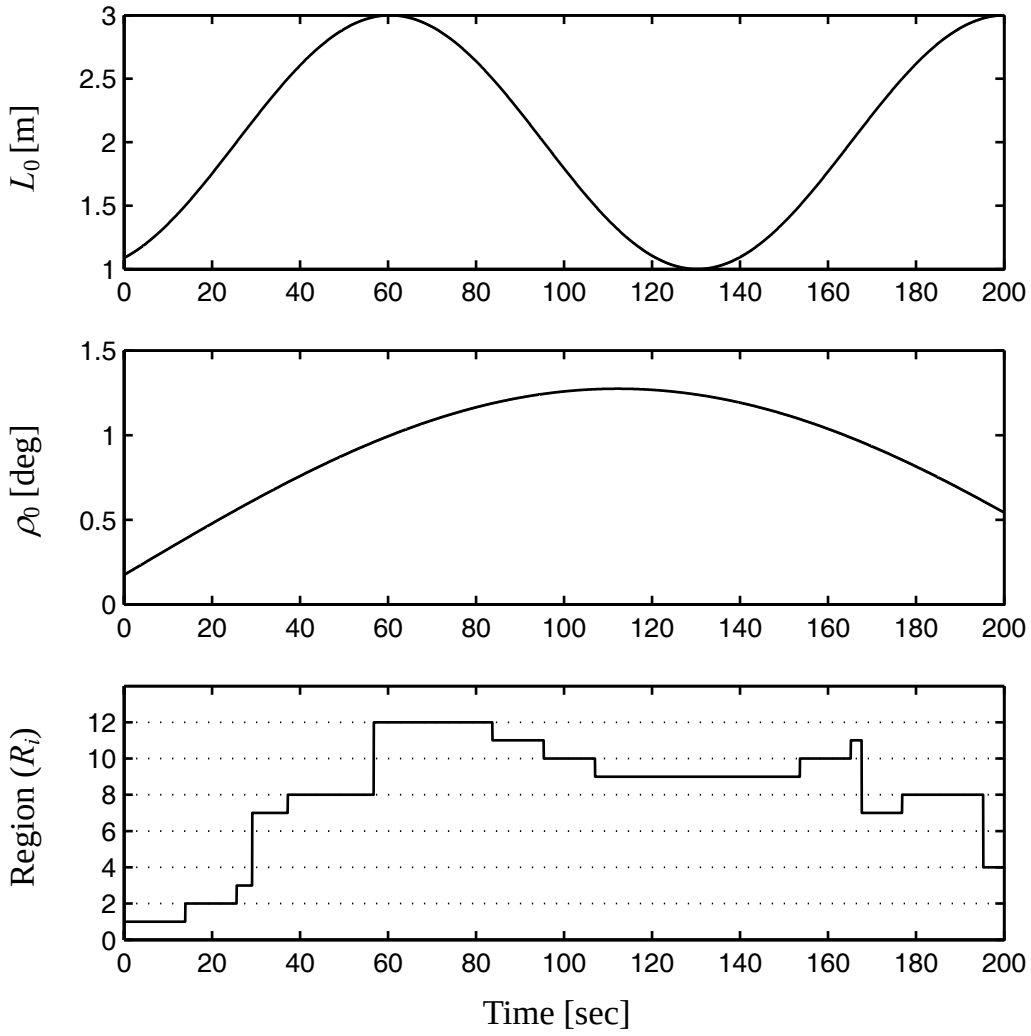

Figure 3.5: Output of the region finder

3.4 Controller design

The PI-Observer discussed in section 3.3 reconstructs the states and the unknown disturbance force p_2. When the disturbances are known, their effect on the response may be canceled or compensated using one of the classical known methods.
In this section, the controller is designed for the model given by Eqs. (3.4) and (3.12). In order to cancel/reduce the effect of the disturbances and to ensure safe cargo transfer of the cane, the control input $\boldsymbol{u}$ is decomposed into three parts,

$$\boldsymbol{u} = \boldsymbol{u}_\delta + \boldsymbol{u}_2 + \boldsymbol{u}_z, \tag{3.26}$$

where $\boldsymbol{u}_\delta$ and $\boldsymbol{u}_2$ are suggested to act against the measured disturbance $\Delta\delta$ and the estimated disturbance p_2 respectively, and $\boldsymbol{u}_z$ is chosen to provide the optimal control for the crane using state feedback, i.e.,

$$\boldsymbol{u}_{\delta} = -\boldsymbol{K}_{\delta}\Delta\delta\,, \tag{3.27}$$

$$\boldsymbol{u}_{2} = -\boldsymbol{K}_{2}\hat{p}_{2}\,, \tag{3.28}$$

$$\boldsymbol{u}_{z} = -\boldsymbol{K}_{z}\hat{\boldsymbol{z}}\,, \tag{3.29}$$

where $\hat{\boldsymbol{z}}$ and $\hat{p}_2$ are the estimated states obtained from Eq. (3.18).

3.4.1 Defining $\boldsymbol{K}_{\delta}$

The rolling motion of the ship affects the payload through the structure of the crane; this tends to disturb the equilibrium position of the payload as demonstrated in Fig. 3.6. It is clear from this figure, that a small roll angle $\Delta\delta$ produces a large shift in the equilibrium position of the payload which induces the unwanted pendulation. The idea behind static disturbance compensation is to find an input vector proportional to the rolling disturbance that can maintain the position of the payload in place as much as possible. This can be achieved in three steps as shown in Figs. (3.7-3.9). In the first step, the luff angle $\Delta\rho$ is employed to prevent the boom from changing its orientation with respect to the horizontal reference by maintaining $\beta = \beta_0$. In the second step the x-coordinate of the payload is recovered by displacing the position of the lower suspension point through ΔD. In the third step the error in the y-coordinate is eliminated by changing the length of the upper cable through ΔL, these three step have to be executed in parallel (at the same time). To find the numerical values of the corresponding three inputs, set the changes in x_{20} and y_{20} resulting from rolling to be zero, i.e.,

$$\Delta x_{20} \approx \frac{\partial x_{20}}{\partial \delta}\Delta\delta + \frac{\partial x_{20}}{\partial \beta}\Delta\beta + \frac{\partial x_{20}}{\partial L}\Delta L + \frac{\partial x_{20}}{\partial D}\Delta D + \frac{\partial x_{20}}{\partial w_6}\Delta w_6 + \frac{\partial x_{20}}{\partial \theta_6}\Delta\theta_6 = 0 \tag{3.30}$$

$$\Delta y_{20} \approx \frac{\partial y_{20}}{\partial \delta}\Delta\delta + \frac{\partial y_{20}}{\partial \beta}\Delta\beta + \frac{\partial y_{20}}{\partial L}\Delta L + \frac{\partial y_{20}}{\partial D}\Delta D + \frac{\partial y_{20}}{\partial w_6}\Delta w_6 + \frac{\partial y_{20}}{\partial \theta_6}\Delta\theta_6 = 0. \tag{3.31}$$

The condition $\beta = \beta_0$ can be fulfilled by setting $\Delta\beta = 0$, i.e.,

$$\Delta\rho = -\Delta\delta. \tag{3.32}$$

Here the roll angle $\Delta\delta$ is assumed to be measured. Therefore, Eqs. (3.30-3.32) can be written in the matrix form

$$\underbrace{\begin{bmatrix} 1 & 0 & 0 \\ 0 & \partial x_{20}/\partial L & \partial x_{20}/\partial D \\ 0 & \partial y_{20}/\partial L & \partial y_{20}/\partial D \end{bmatrix}}_{\boldsymbol{A}_\delta} \underbrace{\begin{bmatrix} \Delta\rho \\ \Delta L \\ \Delta D \end{bmatrix}}_{\boldsymbol{u}_\delta} = -\underbrace{\begin{bmatrix} 1 \\ \partial x_{20}/\partial\delta \\ \partial y_{20}/\partial\delta \end{bmatrix}}_{\boldsymbol{B}_\delta} \Delta\delta - \underbrace{\begin{bmatrix} 0 & 0 \\ \partial x_{20}/\partial w_6 & \partial x_{20}/\partial\theta_6 \\ \partial y_{20}/\partial w_6 & \partial y_{20}/\partial\theta_6 \end{bmatrix}}_{\boldsymbol{F}_\delta} \begin{bmatrix} \Delta w_6 \\ \Delta\theta_6 \end{bmatrix}. \tag{3.33}$$

The displacements $[\Delta w_6 \quad \Delta\theta_6]^T$ can be calculated from Eq. (3.1), which can be written in the form

$$\boldsymbol{K}_0\boldsymbol{q} = \boldsymbol{B}_1\boldsymbol{u} + \boldsymbol{B}_3\Delta\delta. \tag{3.34}$$

Substituting Eq. (3.32) in Eq. (3.34) yields

$$\boldsymbol{q} = \boldsymbol{K}_0^{-1}\boldsymbol{B}_r \begin{bmatrix} \Delta L \\ \Delta D \end{bmatrix}, \tag{3.35}$$

where $\boldsymbol{B}_r$ is a reduced order matrix of $\boldsymbol{B}_1$ of order 12×2 consisting of the second and third columns of $\boldsymbol{B}_1$.

Premultiplying both sides of Eq. (3.35) by the transformation matrix

$$\boldsymbol{H} = \begin{bmatrix} 0 & 0 & 0 & 0 & 0 & 0 & 0 & 0 & 1 & 0 & 0 & 0 \\ 0 & 0 & 0 & 0 & 0 & 0 & 0 & 0 & 0 & 1 & 0 & 0 \end{bmatrix} \tag{3.36}$$

gives

$$\begin{bmatrix} \Delta w_6 \\ \Delta\theta_6 \end{bmatrix} = [\boldsymbol{H}\boldsymbol{K}_0^{-1}\boldsymbol{B}_r] \begin{bmatrix} \Delta L \\ \Delta D \end{bmatrix}$$

$$= \underbrace{\begin{bmatrix} \mathbf{0} \\ \boldsymbol{H}\boldsymbol{K}_0^{-1}\boldsymbol{B}_r \end{bmatrix}}_{\boldsymbol{G}_\delta} \begin{bmatrix} \Delta\rho \\ \Delta L \\ \Delta D \end{bmatrix}. \tag{3.37}$$

In view of Eq. (3.37), equation (3.33) can be written in compact form as

$$\boldsymbol{u}_\delta = -[\boldsymbol{A}_\delta + \boldsymbol{F}_\delta\boldsymbol{G}_\delta]^{-1}\boldsymbol{B}_\delta\,\Delta\delta. \tag{3.38}$$

Comparing the above equation with Eq. (3.27) yields

$$\boldsymbol{K}_{\delta} = [\boldsymbol{A}_{\delta} + \boldsymbol{F}_{\delta}\boldsymbol{G}_{\delta}]^{-1}\boldsymbol{B}_{\delta}\,. \tag{3.39}$$

Simulation results corresponding to 3.0° sinusoidal rolling motion in the neighborhood of the first eigenfrequency are shown in Fig. 3.10. It is noted that the proposed rolling disturbance compensator gain $\boldsymbol{K}_{\delta}$ can reduce the rolling induced pendulations of the payload significantly.

3.4.2 Defining $\boldsymbol{K}_2$

It can be seen from Fig. 1 that the disturbance p_2 acts only on the payload m_2, therefore, it can be easily concluded from Eqs. (2.30 and 2.38) that the corresponding disturbance matrix is

$$\boldsymbol{B}_5 = [0 \quad 0 \quad 0 \quad 0 \quad 0 \quad 0 \quad 0 \quad 0 \quad 0 \quad 0 \quad -1 \quad 1]^T \tag{3.40}$$

Therefore, in view of Eq. (3.9), it can be seen that p_2 affects directly only the last two states z_{23} and z_{24}, while the structure of the input matrix described by Eq. (3.7) indicates that the input vector $\boldsymbol{u}$ affects all the last 12 states, which means that any attempt to cancel the effect of the disturbance on the last two states will disturb the other states. Therefore, there is no feedback matrix using $\boldsymbol{K}_2$ that can cancel statically the effect of p_2 without exciting the other states. Accordingly, the effect of this disturbance force can be reduced by using a closed loop state feedback control leading to dynamical accommodation. In this case, there is no need to measure it. Accordingly, the following question may arise: is it necessary in this case to estimate this disturbance? The answer is yes, because the state feedback controller uses the estimated states obtained by the observer, which can reconstruct the states with minimum error only if the disturbances are taken into consideration while reconstructing the states. This is achieved by using the PI-observer.

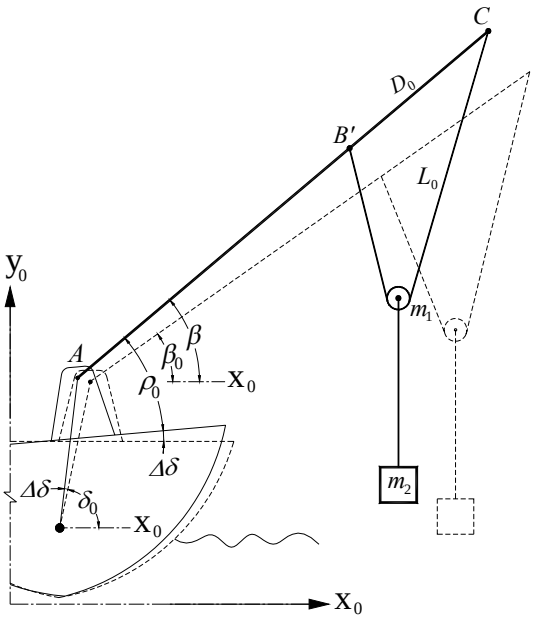

Roll angle = $\Delta\delta$
Luff angle = ρ_0
Position of the lower suspension point = D_0
Length of the upper cable = L_0

Figure 3.6: Rolling through $\Delta\delta$

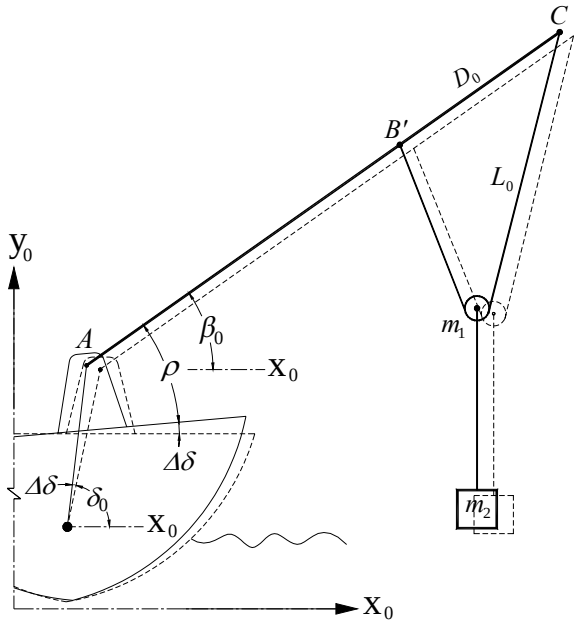

Roll angle = $\Delta\delta$
Luff angle $\rho = \rho_0 - \Delta\delta$
Position of the lower suspension point = D_0
Length of the upper cable = L_0

Figure 3.7: Compensation through $\Delta\rho$

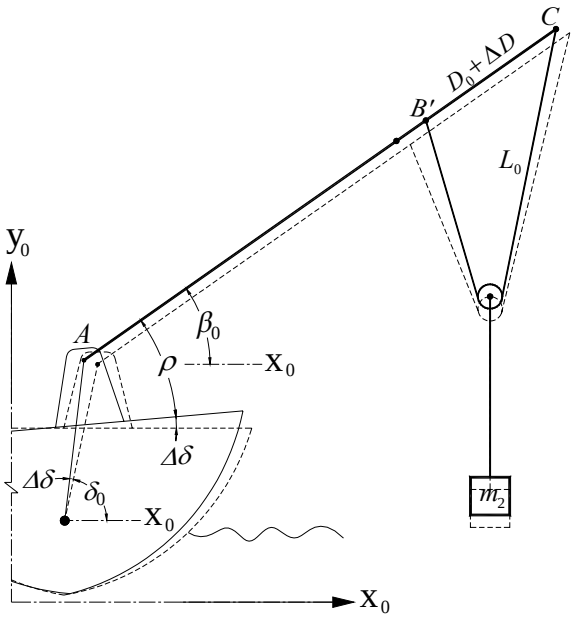

Roll angle = $\Delta\delta$
Luff angle $\rho = \rho_0 - \Delta\delta$
Position of the lower suspension point = $D_0 + \Delta D$
Length of the upper cable = L_0

Figure 3.8: Compensation through ΔD

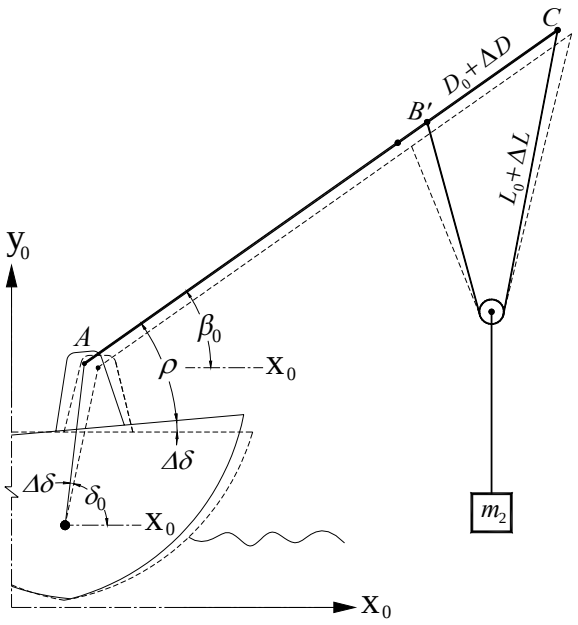

Roll angle = $\Delta\delta$
Luff angle $\rho = \rho_0 - \Delta\delta$
Position of the lower suspension point = $D_0 + \Delta D$
Length of the upper cable = $L_0 + \Delta L$

Figure 3.9: Compensation through ΔL

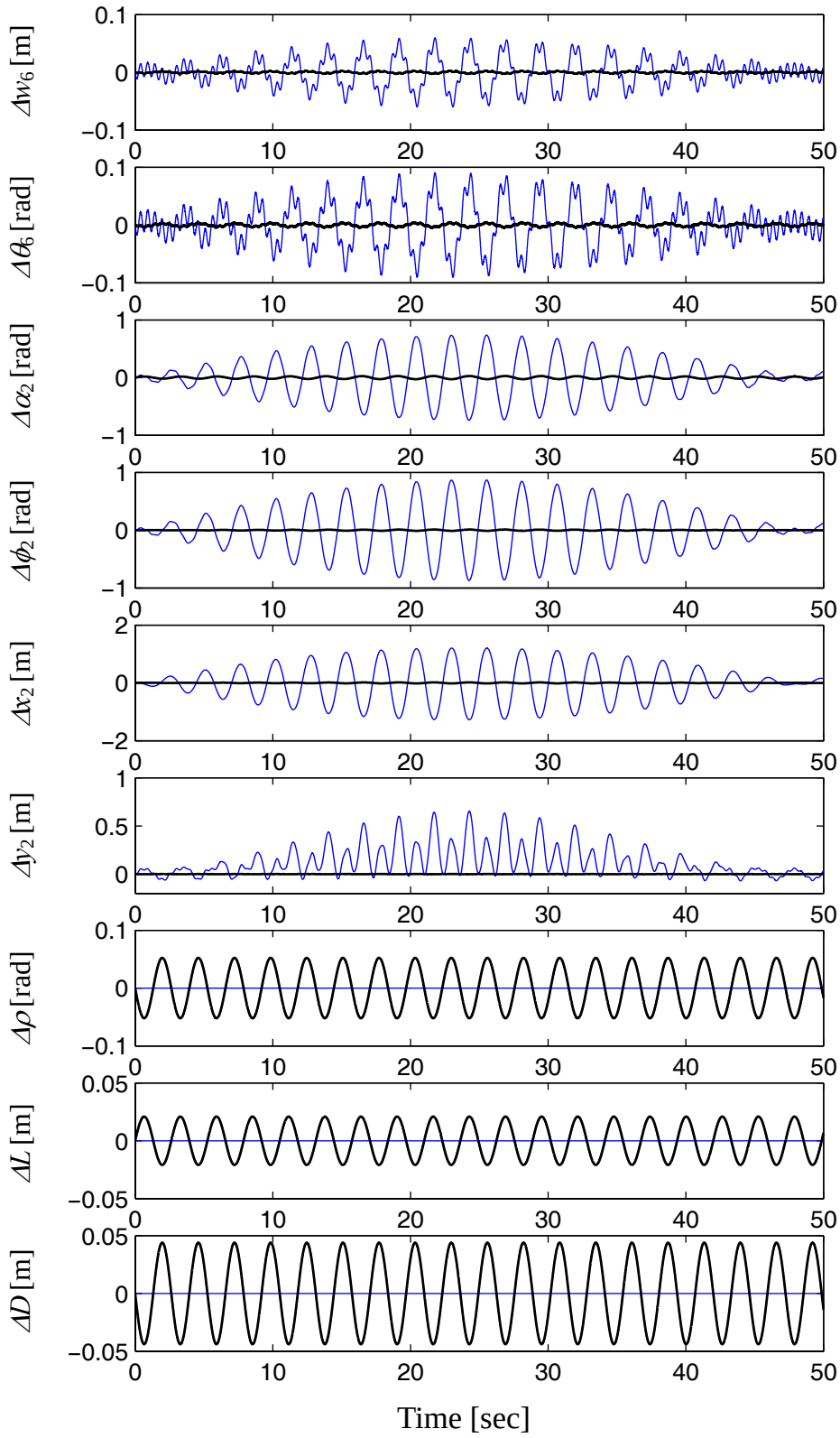

Figure 3.10: Simulation results for disturbance compensation with rolling excitation close to the first eigenfrequency, — without compensation, — with compensation. Rolling amplitude = 3°, $\rho_0 = \pi/4$,

3.4.3 Optimal state feedback control (Calculating $\boldsymbol{K}_z$)

Using the extended state observer described in section 3.3, an optimal linear state feedback controller can be designed if the system is completely state controllable. State controllability can be confirmed by transformation the state space model given by Eq. (3.4) to modal canonical form and ensuring that the corresponding modal input matrix has no rows with zeros for all values of L and β under consideration [Lun02]. In this case, and in view of Eqs. (3.27 and 3.29), the input vector can be calculated as

$$\boldsymbol{u} = -\boldsymbol{K}_z\,\hat{\boldsymbol{z}} - \boldsymbol{K}_\delta \Delta\delta. \tag{3.41}$$

Here $\boldsymbol{u}_2$ is set equal to zero as concluded from section 3.4.2. Inserting Eq. (3.41) into Eq. (3.4) gives

$$\dot{\boldsymbol{z}} = \boldsymbol{A}\boldsymbol{z} - \boldsymbol{B}\boldsymbol{K}_z\,\hat{\boldsymbol{z}} + (\boldsymbol{E} - \boldsymbol{B}\boldsymbol{K}_\delta)\Delta\delta + \boldsymbol{N}p_2\,. \tag{3.42}$$

Assuming that the estimated states using the PI-observer converge to their real values in real time with negligible error, then the above equation can be written as

$$\dot{\boldsymbol{z}} = (\boldsymbol{A} - \boldsymbol{B}\boldsymbol{K}_z)\,\boldsymbol{z} + (\boldsymbol{E} - \boldsymbol{B}\boldsymbol{K}_\delta)\Delta\delta + \boldsymbol{N}p_2\,. \tag{3.43}$$

The state feedback matrix $\boldsymbol{K}_z$ can be calculated as

$$\boldsymbol{K}_z = \boldsymbol{R}^{-1}\boldsymbol{B}^T\boldsymbol{P}, \tag{3.44}$$

where $\boldsymbol{P}$ represents the solution of the algebraic Riccati equation [Oga02, FPE02]

$$\boldsymbol{A}^T\boldsymbol{P} + \boldsymbol{P}\boldsymbol{A} + \boldsymbol{Q} - \boldsymbol{P}\boldsymbol{B}\boldsymbol{R}^{-1}\boldsymbol{B}^T\boldsymbol{P} = \boldsymbol{0}. \tag{3.45}$$

Here $\boldsymbol{Q}$ and $\boldsymbol{R}$ are symmetric positive definite weighting matrices of the states and inputs respectively [ML97]. According to the numerical structure of these matrices, the eigenvalues of the controlled crane system can be altered to get the required behavior of the dynamic response. In reality, the estimated states are used in the feedback loop instead of their real values. Therefore, to guarantee the operation of the controller, the observer must be faster than the real system. Therefore, the eigenvalues of the observer are placed enough to the left of the eigenvalues of the controlled crane; this can be done by tuning the numerical structure of the corresponding weight matrices. With reference to Fig. 3.10, it can be noted that the term $(\boldsymbol{E}-\boldsymbol{B}\boldsymbol{K}_\delta)\Delta\delta$, which is seen in the right hand side of Eq. (3.42), has a negligible effect on the controlled response because of the disturbance compensation ability of the used rolling disturbance compensator $\boldsymbol{u}_\delta$. This means that, the optimal state feedback control is necessary to suppress the

vibrations that can appear due to a nonzero initial condition of the states or due to the presence of the wind force p_2 which is considerable in bad weathers. It is also important to mention here, that the numerical values of the controller gains $\boldsymbol{K}_\delta$ and $\boldsymbol{K}_z$ must be updated according to the current equilibrium region. The operating region, which is governed by the current length of the rope L_0 and the current luff angle ρ_0, is determined by the region finder as discussed before in section 3.3. A block diagram representation of the proposed control strategy is shown in Fig. 3.11.

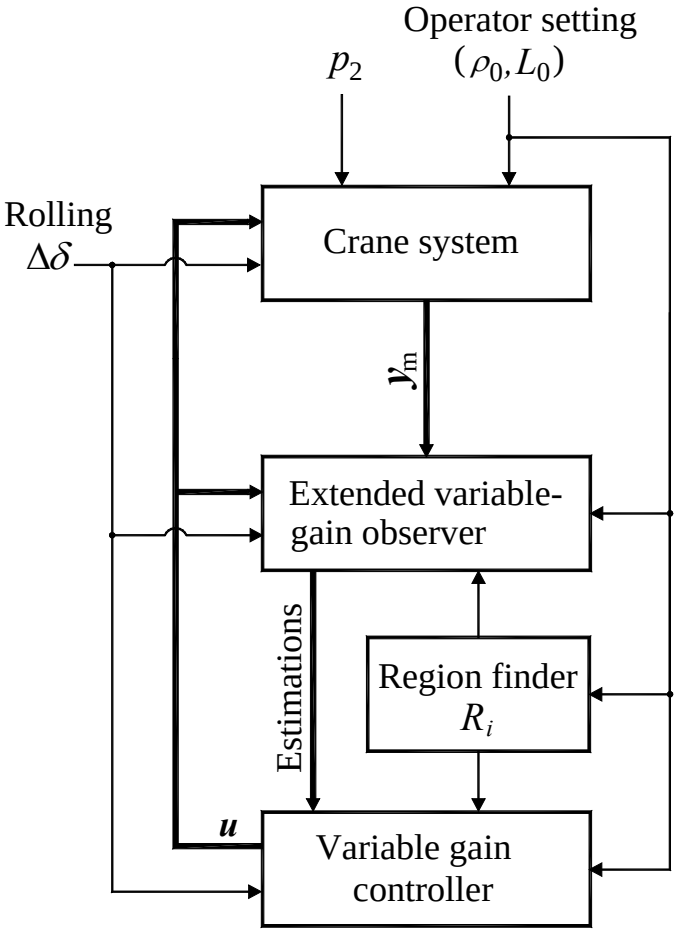

Figure 3.11: Block diagram of the control system

3.5 Robustness

Stability and performance robustness must be taken into consideration in designing feedback control systems. A stable closed loop feedback control system is said to be robust with respect to stability if it remains stable after some changes have been made in the physical or control parameters of the system. In addition, if the system still

fulfills a given level of acceptability of a specific performance criterion such as damping or settling time, then the system is said to be robust with respect to its performance [Dan89]. Here the parameters of the crane vary depending on the current equilibrium point leading to a multi-model problem. Accordingly, the used control strategy is based on dividing the operating parameter space into 12 uniform regions; each region uses a different controller/observer gain set. The size of the region is limited such that the stability and performance robustness of the closed loop control system are ensured over the region. There are many methods to check robustness over the operating region; in the crane under consideration, robustness is guaranteed such that, for all operating points inside each individual region, the dominant eigenvalues of the closed loop system remain in the neighborhood of their nominal values that correspond to the calculated gain of the controller.

To find the appropriate point inside the region at which the corresponding controller gain should be calculated, consider for example the region R_6 shown in Fig. 3.4, and assume, as a first trial, that the region is covered by a constant gain controller and a constant gain observer, and assume that the gain matrix is calculated at the center of the region, i.e., the observer gain matrix and the controller gain matrix are calculated at $\rho_0 = (35°+55°)/2 = 45°$ and $L_0 = (L_{02}+L_{03})/2$. The weighting matrices $\boldsymbol{Q}$ and $\boldsymbol{R}$ are selected such that, sufficient damping is created in the crane with adequate relative stability for the actuators constraint $|\boldsymbol{u}| \leq \max(\boldsymbol{u})$. The current eigenvalues of the closed loop system are obtained by solving the polynomial $|\lambda \boldsymbol{I} - \boldsymbol{A} + \boldsymbol{B}\boldsymbol{K}_z| = 0$. Since $\boldsymbol{A}$ and $\boldsymbol{B}$ vary with the current operating point (L_0,ρ_0) inside the current region, the eigenvalues also vary consequently.

The loci of the three dominant eigenvalues (λ_1, λ_2, and λ_3) and their conjugates due to the variation in L_0 and ρ_0 are shown in Figs. 3.12(a, b, c); the nominal values (design values) of the dominant eigenvalues are denoted by × and the values at the lower left and lower right corners of the region are denoted by □ and ◇ respectively, and the values at the upper left and upper right corners are denoted by Δ and ∇ respectively.
The shaded regions $\Re_{\lambda 1}$, $\Re_{\lambda 2}$ and $\Re_{\lambda 3}$ represent the loci of the dominant eigenvalues for all possible values of ρ_0 and L_0 inside R_6. It can be easily recognized that as the operating point moves toward the lower right corner of the region (L_0 increases and ρ_0 decreases), the eigenvalues λ_1 and λ_3 become closer to the imaginary axis, which means that the crane may lose a considerable percentage of its relative stability with a reduction in the damping ratio.

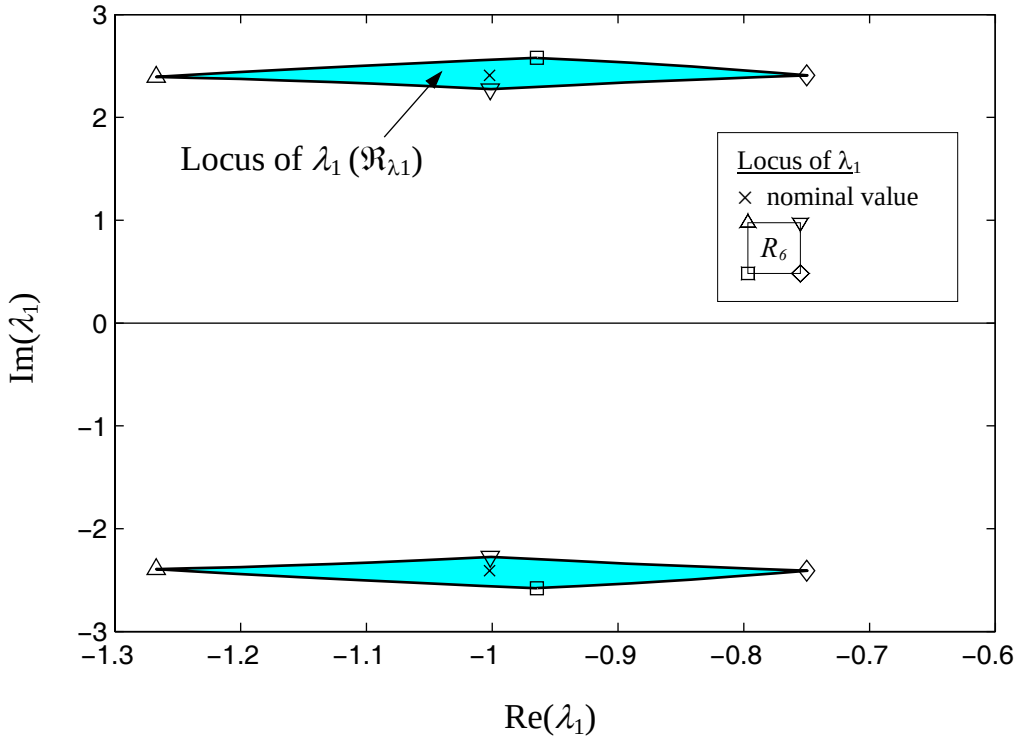

Figure 3.12a: Locus of λ_1 for R_6, the design point is the center point of the region

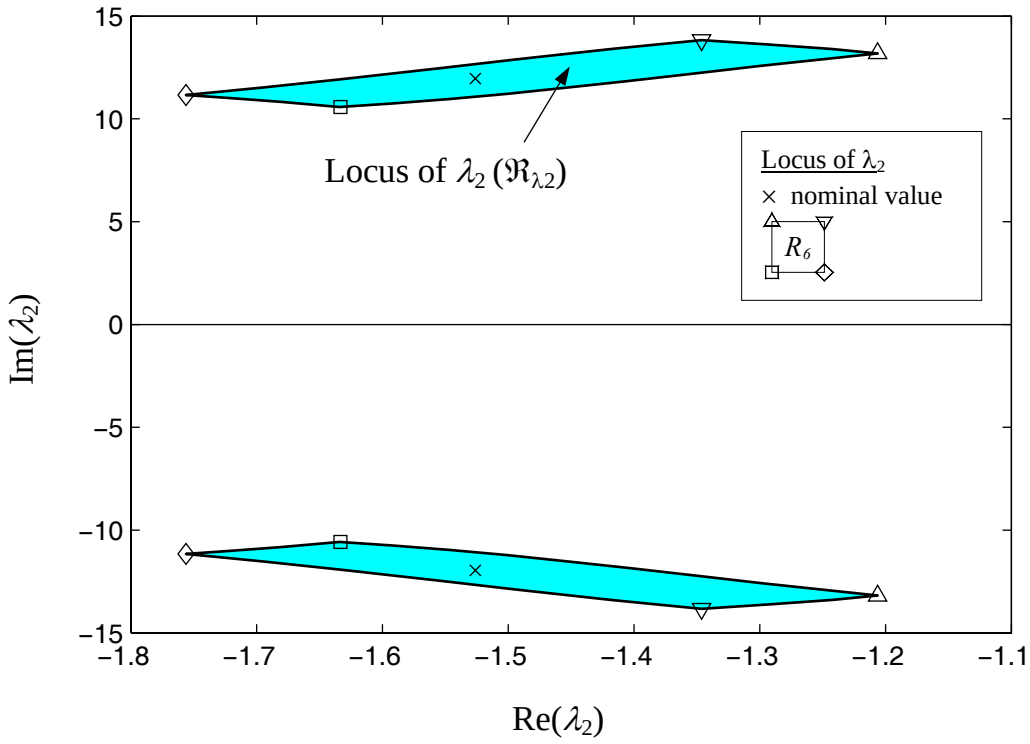

Figure 3.12b: Locus of λ_2 for R_6, the design point is the center point of the region

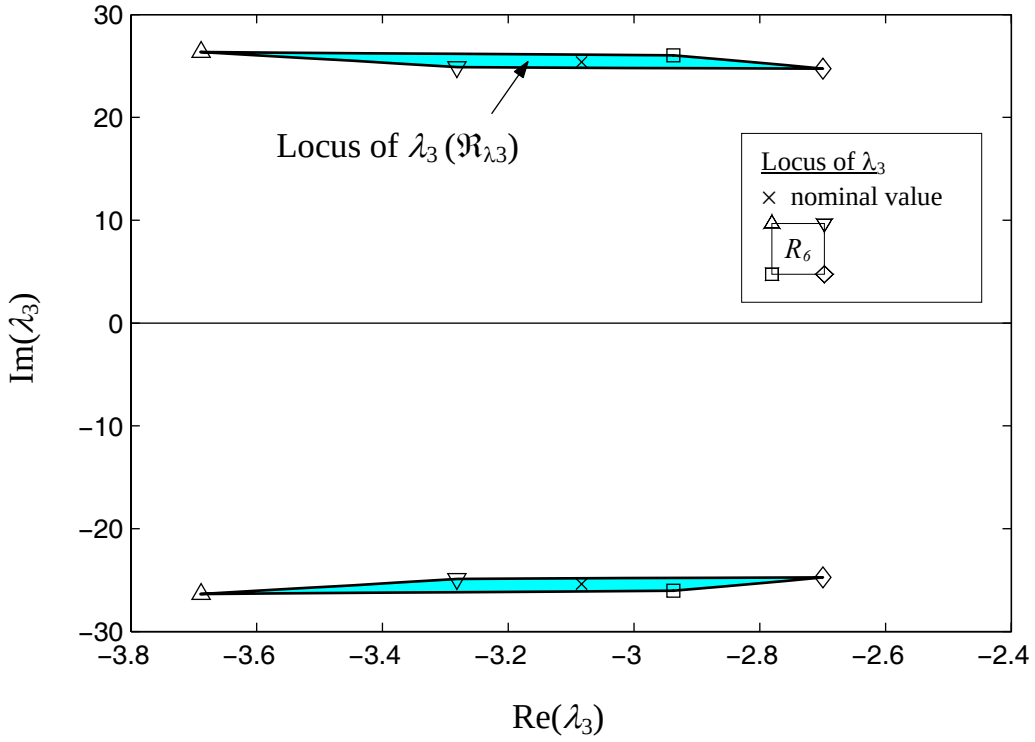

Figure 3.12c: Locus of λ_3 for R_6, the design point is the center point of the region

This leads to the idea of considering the lower right corner as a design point; in this case, the loci of the dominant eigenvalues are shown in Figs. 3.13(a,b,c). It can be seen that for all possible operating points inside R_6, the eigenvalues λ_1 and λ_3 lay to the left of their nominal values, this of course improves the corresponding relative stability and damping ratio. But, the region of λ_2 is completely to the right of its nominal value, such that, as the operating point moves to the upper left corner (Δ), this eigenvalue losses 55% of its relative stability with a considerable reduction in the damping ratio. Therefore, neither the center point nor the lower right corner of the region can give a satisfactory selection of the design point.

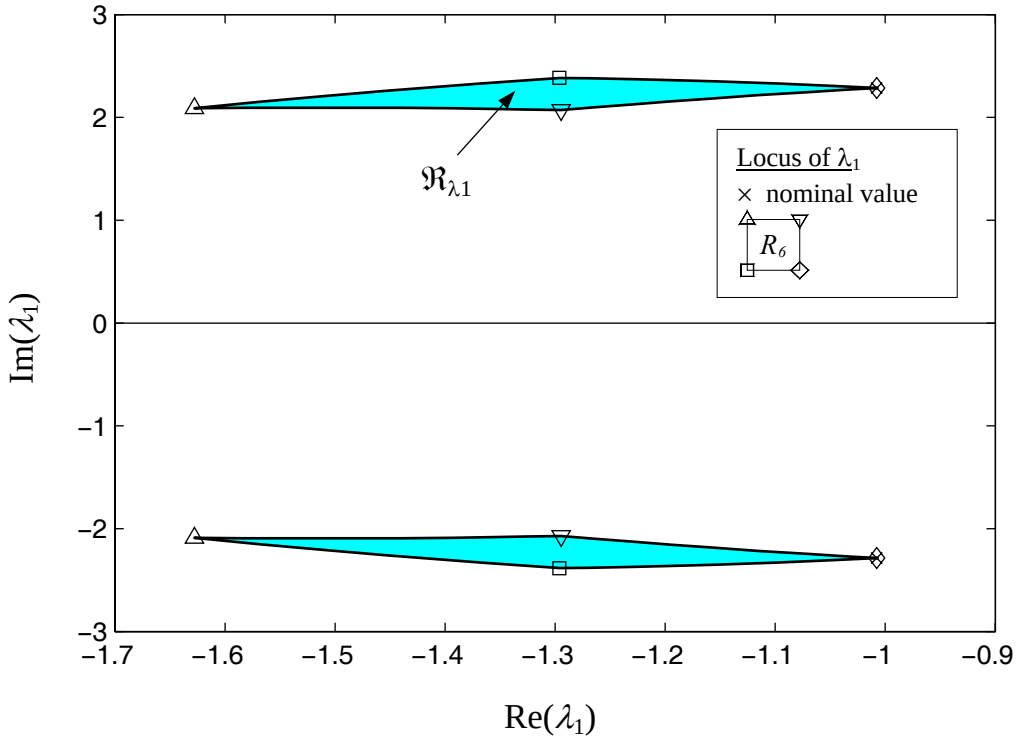

Figure 3.13a: Locus of λ_1 for R_6, the design point is the lower right corner of the region

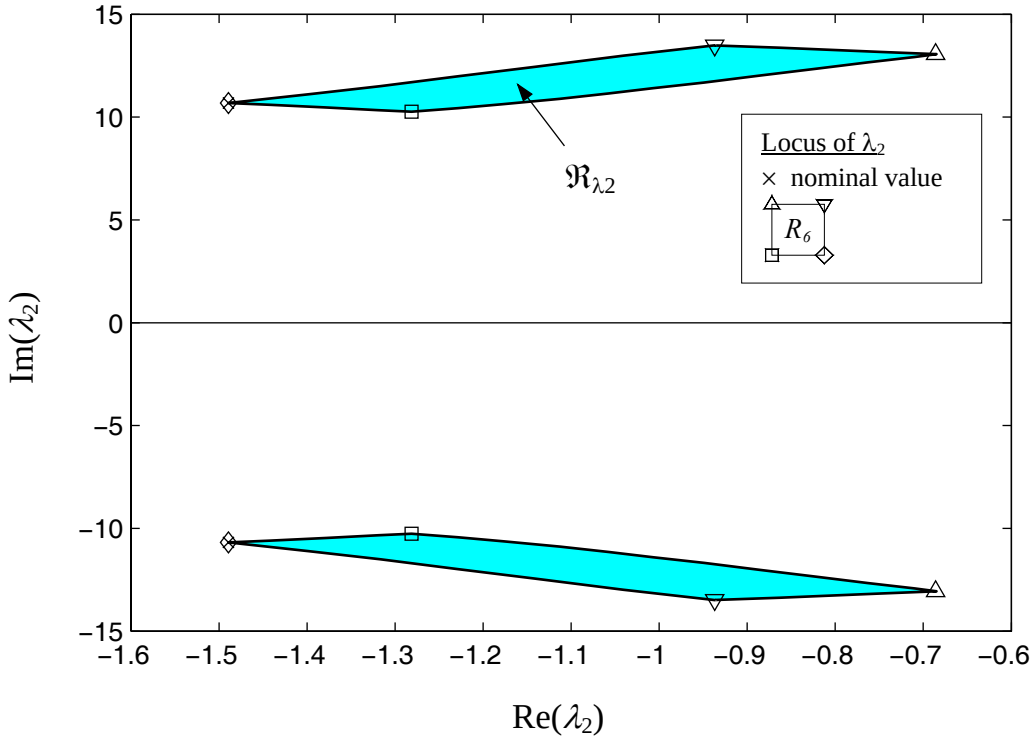

Figure 3.13b: Locus of λ_2 for R_6, the design point is the lower right corner of the region

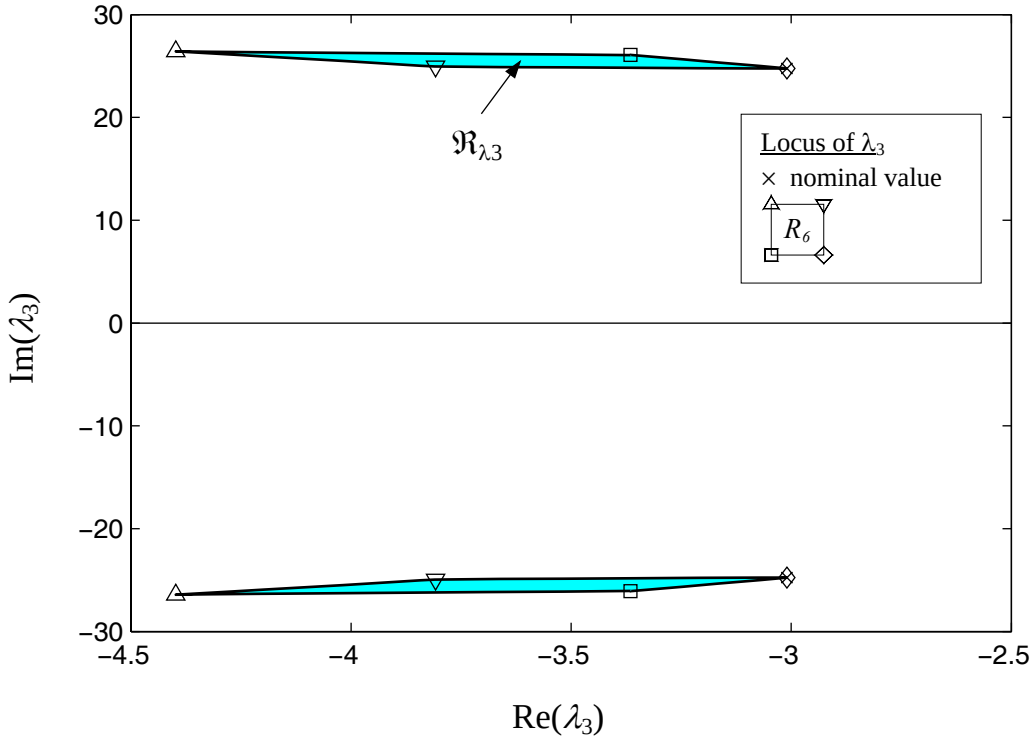

Figure 3.13c: Locus of λ_3 for R_6, the design point is the lower right corner of the region

To overcome this problem, the observer and the controller gains should be updated continuously (not stepwise) inside the operating region according to the current (instantaneous) value of the pair L_0 and ρ_0 to preserve the damping ratio and relative stability over the region. In this way, the gains are calculated at each individual corner of the considered region; the weight matrices are chosen to produce nearly the same relative stability and damping at each corner, and each corner gain should provide a stable operation of the crane for all possible operating points inside the region. The total value of the controller gain, corresponding to the current operating point, is described by the 2-D interpolation polynomial

$$\boldsymbol{K}_z = \boldsymbol{K}_z(x, y) = \boldsymbol{k}_1 + \boldsymbol{k}_2 x + \boldsymbol{k}_3 y + \boldsymbol{k}_4 xy, \tag{3.43}$$

where x and y denote the local coordinate axes of the region as shown in Fig. 3.14, and $\boldsymbol{k}_1, \cdots, \boldsymbol{k}_4$ denote the polynomial coefficient matrices, the numerical values of the these coefficient matrices depend on the gains associated with the corners of the region.

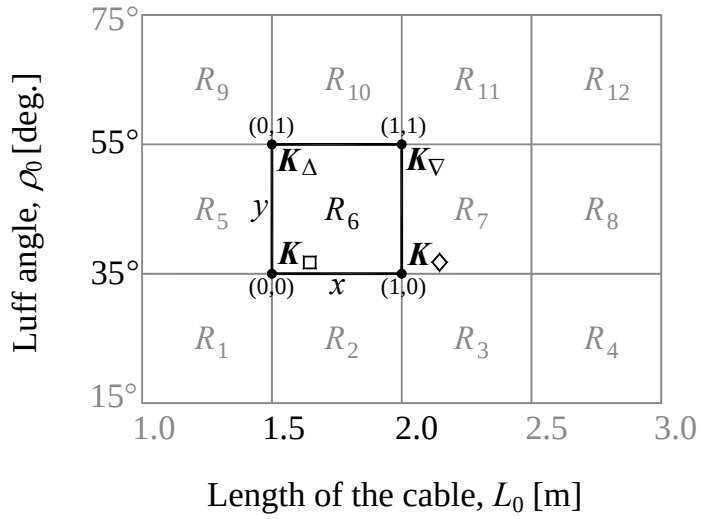

Fig. 3.14: Local coordinates and corner gains of the region

Each corner gain is assumed to satisfy the given interpolation polynomial; therefore, the coefficients of this polynomial can be calculated from Eq. (3.43) to get

$$\begin{aligned}
&\boldsymbol{K}_z(0,0) = \boldsymbol{K}_\square \rightarrow \boldsymbol{k}_1 = \boldsymbol{K}_\square \\
&\boldsymbol{K}_z(1,0) = \boldsymbol{K}_\diamond \rightarrow \boldsymbol{k}_2 = \boldsymbol{K}_\diamond - \boldsymbol{K}_\square \\
&\boldsymbol{K}_z(0,1) = \boldsymbol{K}_\Delta \rightarrow \boldsymbol{k}_3 = \boldsymbol{K}_\Delta - \boldsymbol{K}_\square \\
&\boldsymbol{K}_z(1,1) = \boldsymbol{K}_\nabla \rightarrow \boldsymbol{k}_4 = \boldsymbol{K}_\nabla + \boldsymbol{K}_\square - \boldsymbol{K}_\diamond - \boldsymbol{K}_\Delta .
\end{aligned} \tag{3.44}$$

Substituting Eq. (3.44) into Eq. (3.43) gives

$$\boldsymbol{K}_z = (1-x-y+xy)\boldsymbol{K}_\square + (x-xy)\boldsymbol{K}_\diamond + (y-xy)\boldsymbol{K}_\Delta + (xy)\boldsymbol{K}_\nabla . \tag{3.45}$$

Similarly, the corresponding value of the extended observer gain matrix can be expressed as

$$\boldsymbol{L}_e = (1-x-y+xy)\boldsymbol{L}_\square + (x-xy)\boldsymbol{L}_\diamond + (y-xy)\boldsymbol{L}_\Delta + (xy)\boldsymbol{L}_\nabla , \tag{3.46}$$

and the rolling disturbance compensator gain matrix is described by

$$\boldsymbol{K}_\delta = (1-x-y+xy)\boldsymbol{K}_{\delta\square} + (x-xy)\boldsymbol{K}_{\delta\diamond} + (y-xy)\boldsymbol{K}_{\delta\Delta} + (xy)\boldsymbol{K}_{\delta\nabla} . \tag{3.47}$$

This includes that the gains can be updated continuously according to the local x- and y-coordinates of the current operating point. The loci of the dominant eigenvalues corresponding to R_6 (i.e., $x \in [1;0]$ and $y \in [1;0]$) are shown in Figs. 3.15(a, b, c). Note that the regions $\Re_{\lambda 1\ldots 3}$ of the loci of the dominant eigenvalues are considerably

contracted. Therefore, the relative stability and the damping property are preserved for all operating points inside the region.

Another significant advantage acquired using this interpolation method is that, the problem which may appear due to a stepwise change of the controller gain between two different regions is avoided.

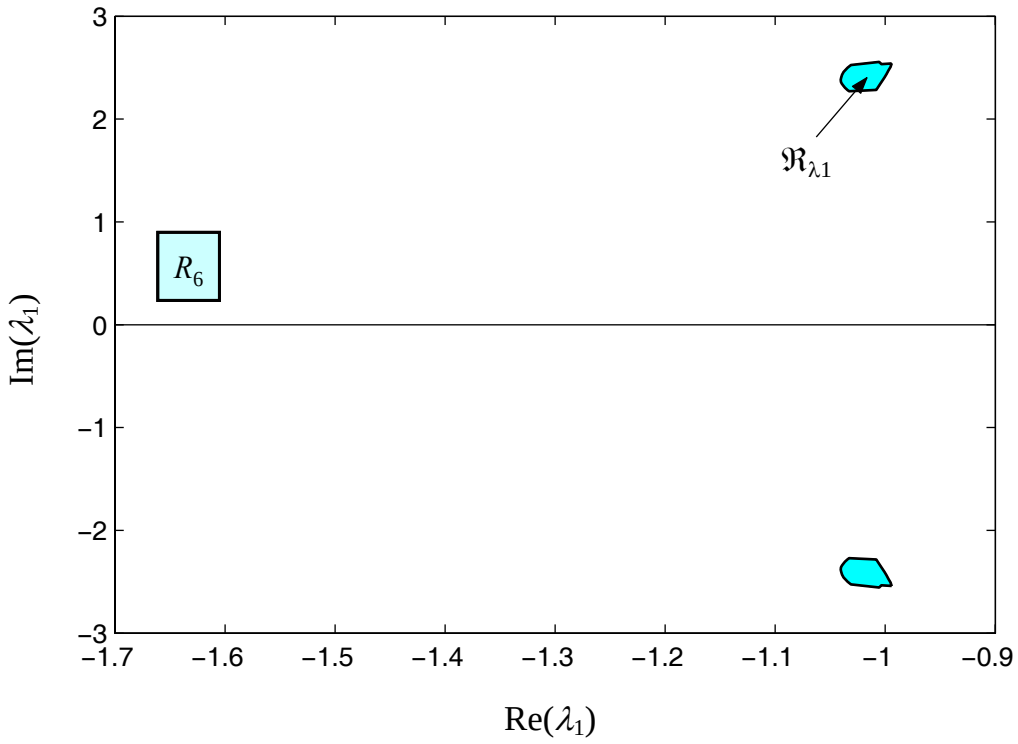

Figure 3.15a: Locus of λ_1 for R_6 using continuous gain method

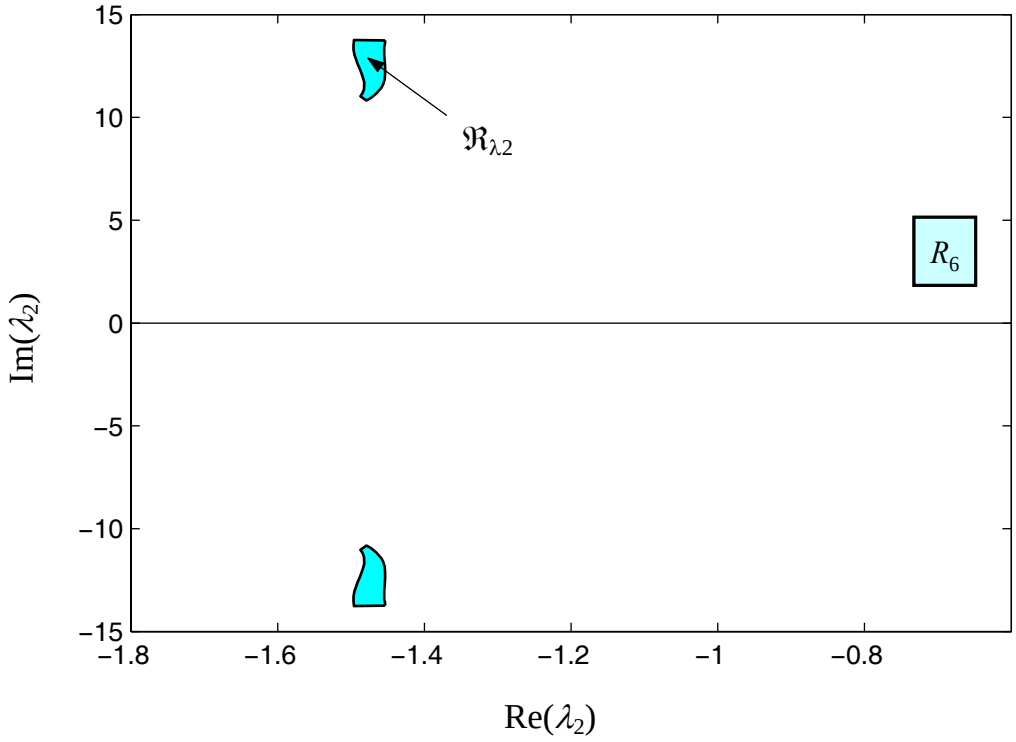

Figure 3.15b: Locus of λ_2 for R_6 using continuous gain method

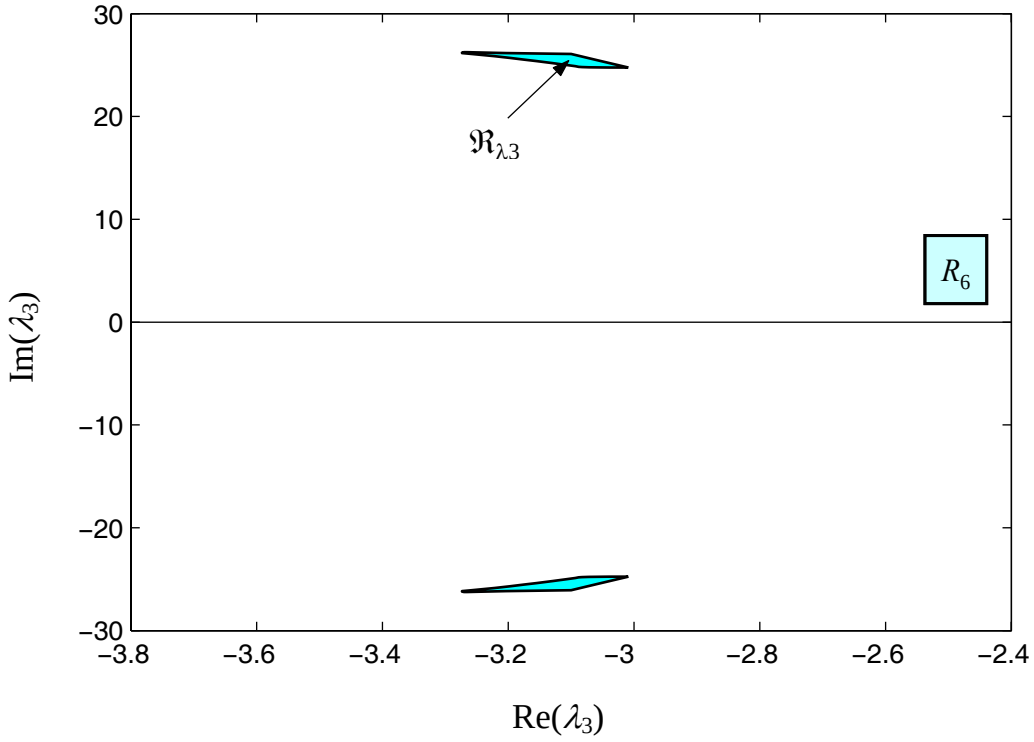

Figure 3.15c: Locus of λ_3 for R_6 using continuous gain method

Figures 3.16(a,b,c) show the loci of the dominant eigenvalues based on the continuous gain method for all admissible equilibrium points inside the entire working space of the crane. i.e., for the control law covering the 12 operating regions. It can be recognized that stability and damping properties are fulfilled.

The previous plots are based on the nominal value of the payload mass, i.e., m_{20} = 5kg. In practice, the payload mass is uncertain; it depends on the cargo being hoisted and may vary within a known interval. Therefore, the crane must be also robust varying values of the payload. In Figs. 3.17(a,b,c) the regions of the dominant eigenvalues are plotted for entire working space of the crane with uncertain payload mass $m_2 \in [0.5;1.5]m_{20}$. Note that the stability is fulfilled for all parameters under consideration.

3.6 Simulation results

Simulation results for different operating conditions, based on the developed continuous gain method, are shown in Figs. (3.18-3.25). In Figs. (3.18-3.20) the payload is subjected to the initial condition $\phi_2(0)$ = 1.0 rad with different operating conditions in terms of the luff angle and cable length. Here the crane is allowed to vibrate for the first 10 seconds, and then the controller is turned ON at t=10 seconds to check the operation of the controller and its ability to suppress the existing vibrations in the elastic and rigid parts of the crane.

In Fig. 3.21 the ship is subjected to sinusoidal rolling excitation with a variable frequency. The response for a sinusoidal rolling close to the average value of the first eigenfrequency of the crane and payload is given in Fig. 3.22. And the effect of a nonzero initial condition in addition to the rolling disturbance excitation is shown in Fig. 3.23. In all cases the observer has no knowledge about the initial condition of the crane. i.e., the initial condition of the observer is set to be zero. In Figs. 3.24 and 3.25, a nonzero disturbance force acting directly on the payload is included. For all of the above mentioned cases, it can be recognized that the controller performs very well and the oscillations are reduced significantly without any noticeable abnormal secondary effect or chattering in the response due to changing the operating region of the crane.

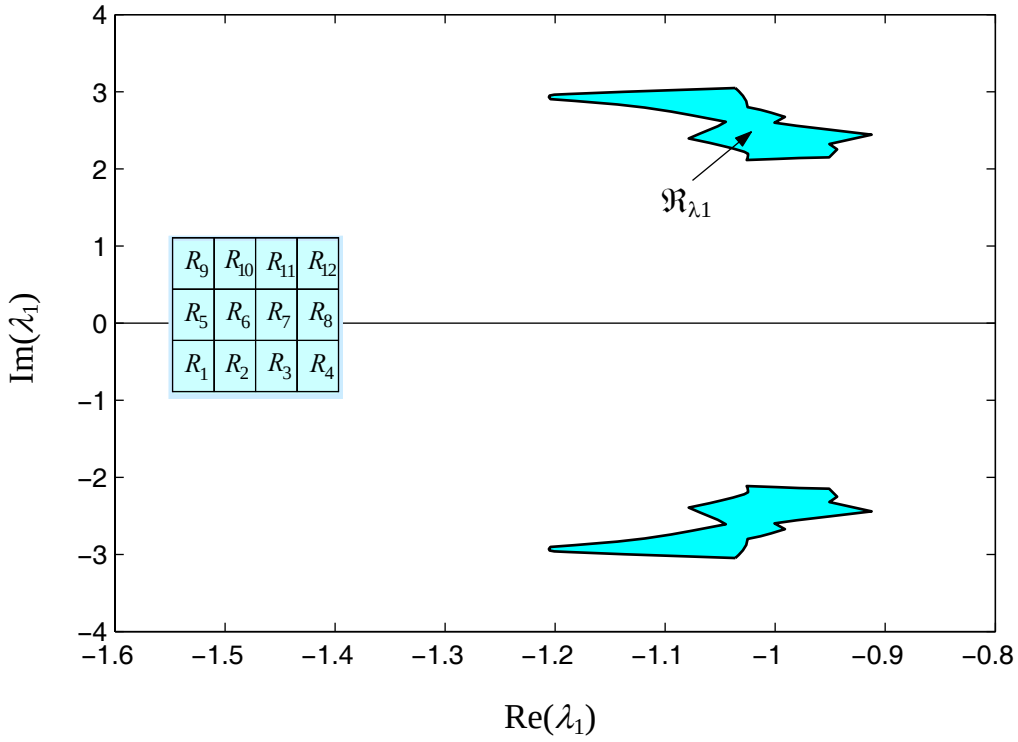

Figure 3.16a: Locus of λ_1 using continuous gain method for all possible values of L_0 and ρ_0 in the entire working space of the crane based on the nominal value of m_2

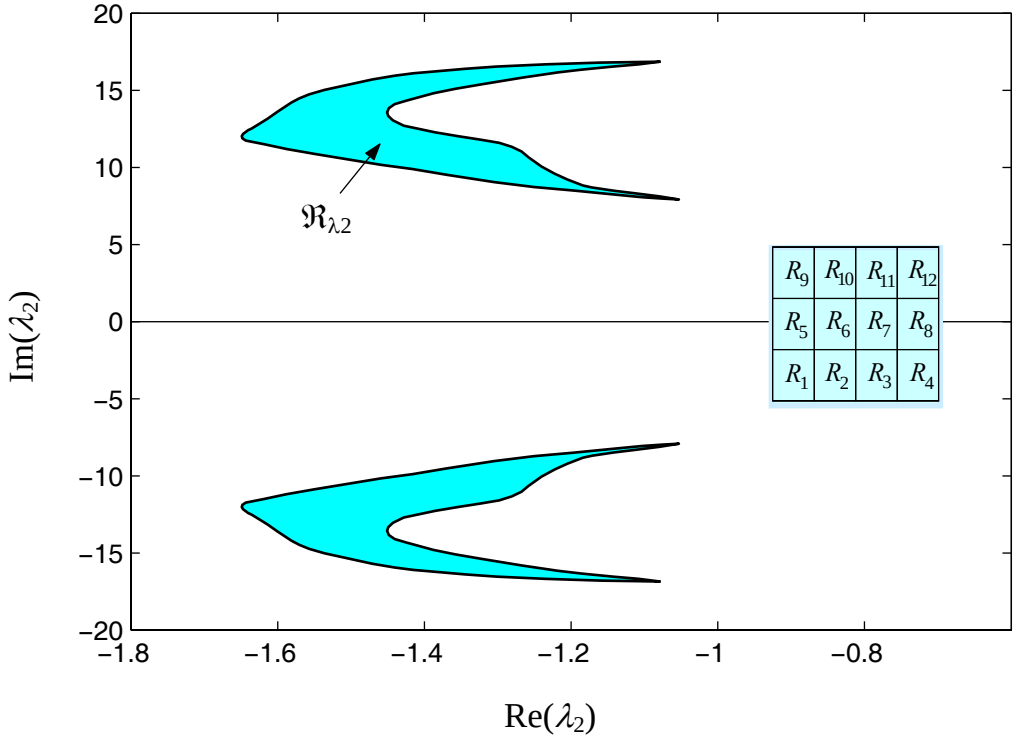

Figure 3.16b: Locus of λ_2 using continuous gain method for all possible values of L_0 and ρ_0 in the entire working space of the crane based on the nominal value of m_2

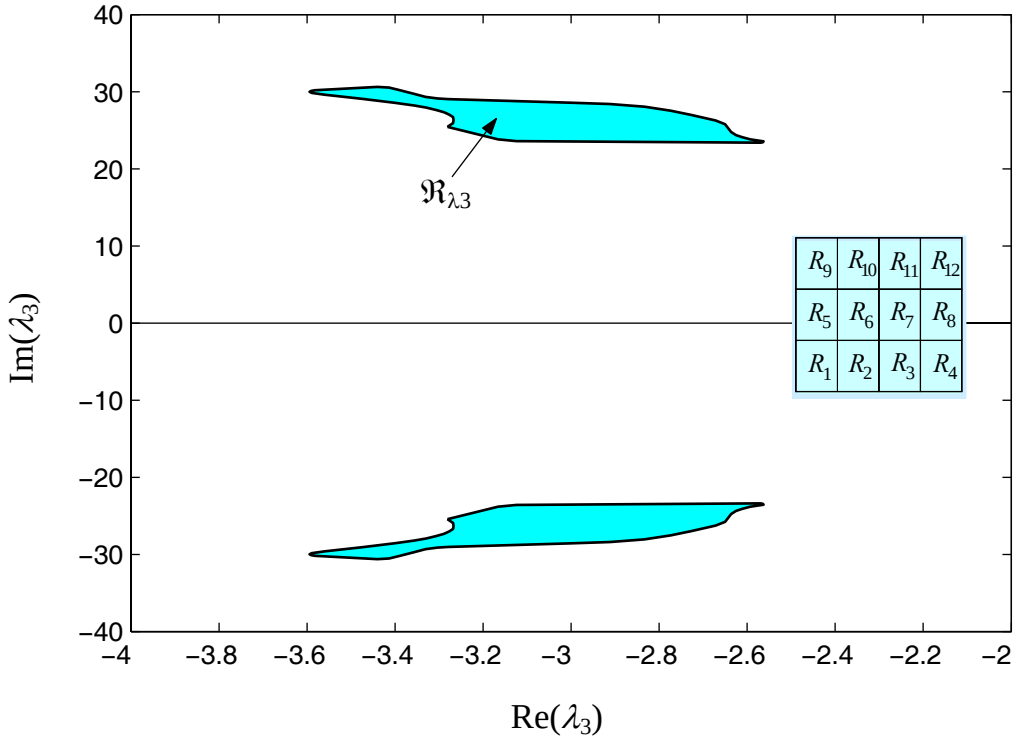

Figure 3.16c: Locus of λ_3 using continuous gain method for all possible values of L_0 and ρ_0 in the entire working space of the crane based on the nominal value of m_2

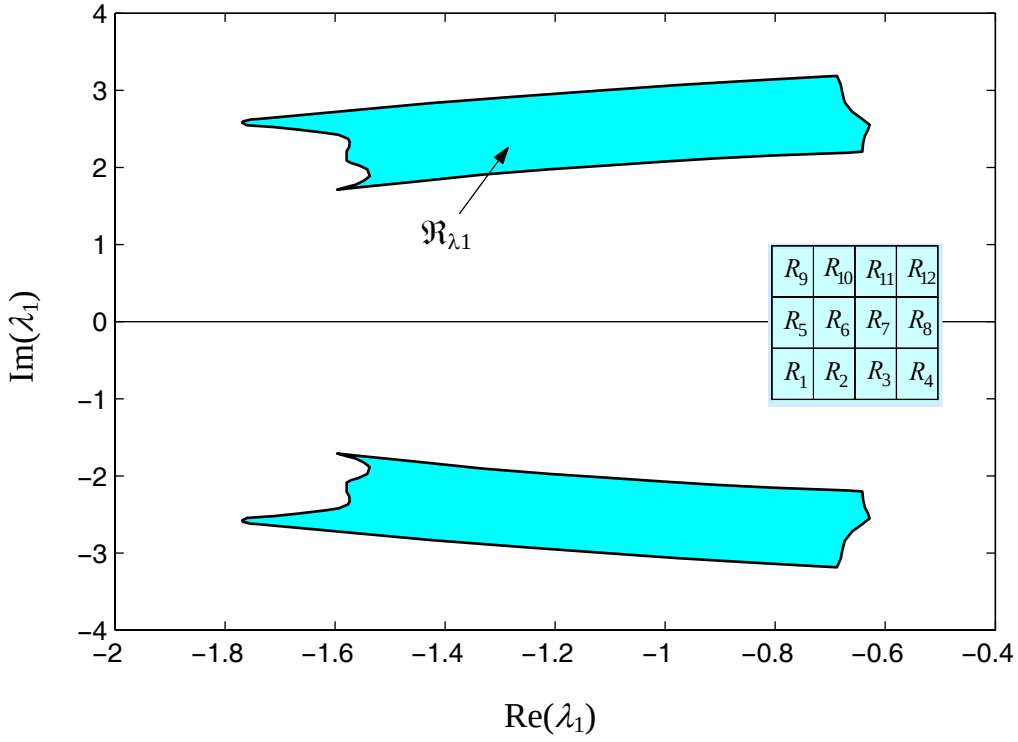

Figure 3.17a: Locus of λ_1 using continuous gain method for all possible values of L_0 and ρ_0 in the entire working space of the crane with uncertain value of m_2

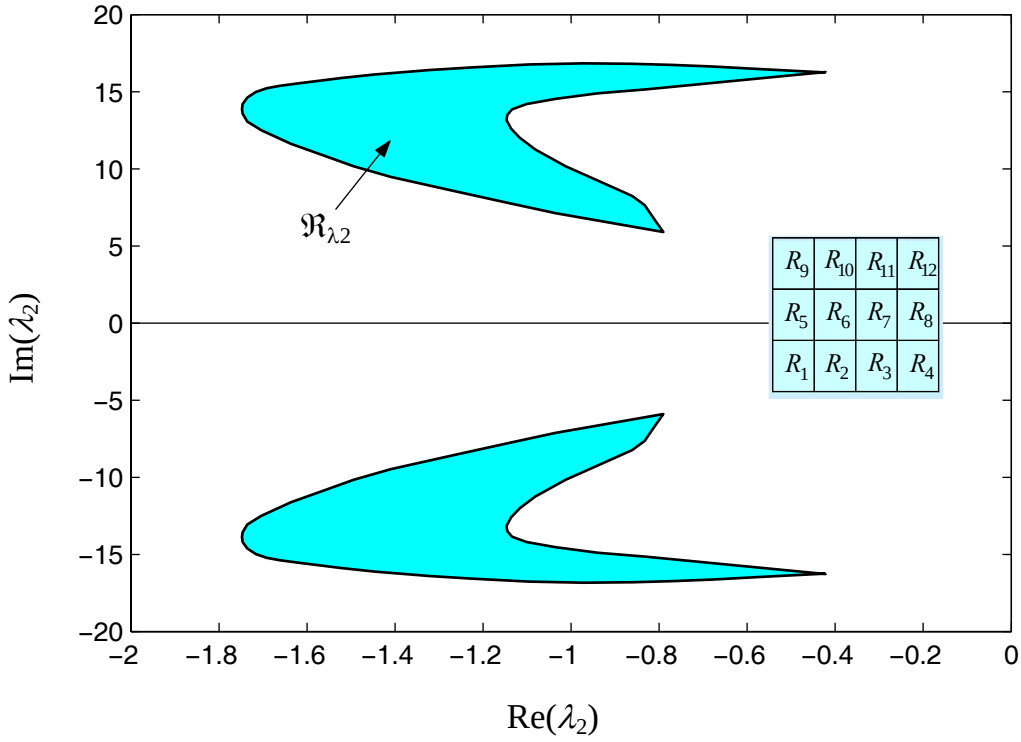

Figure 3.17b: Locus of λ_2 using continuous gain method for all possible values of L_0 and ρ_0 in the entire working space of the crane with uncertain value of m_2

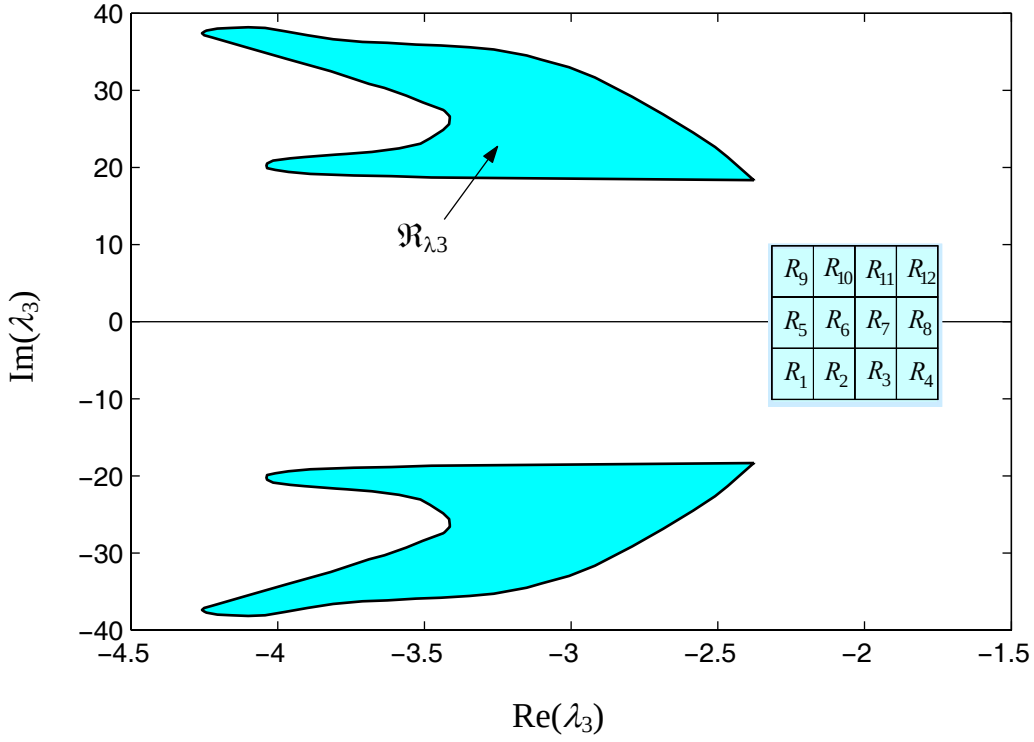

Figure 3.17c: Locus of λ_3 using continuous gain method for all possible values of L_0 and ρ_0 in the entire working space of the crane with uncertain value of m_2

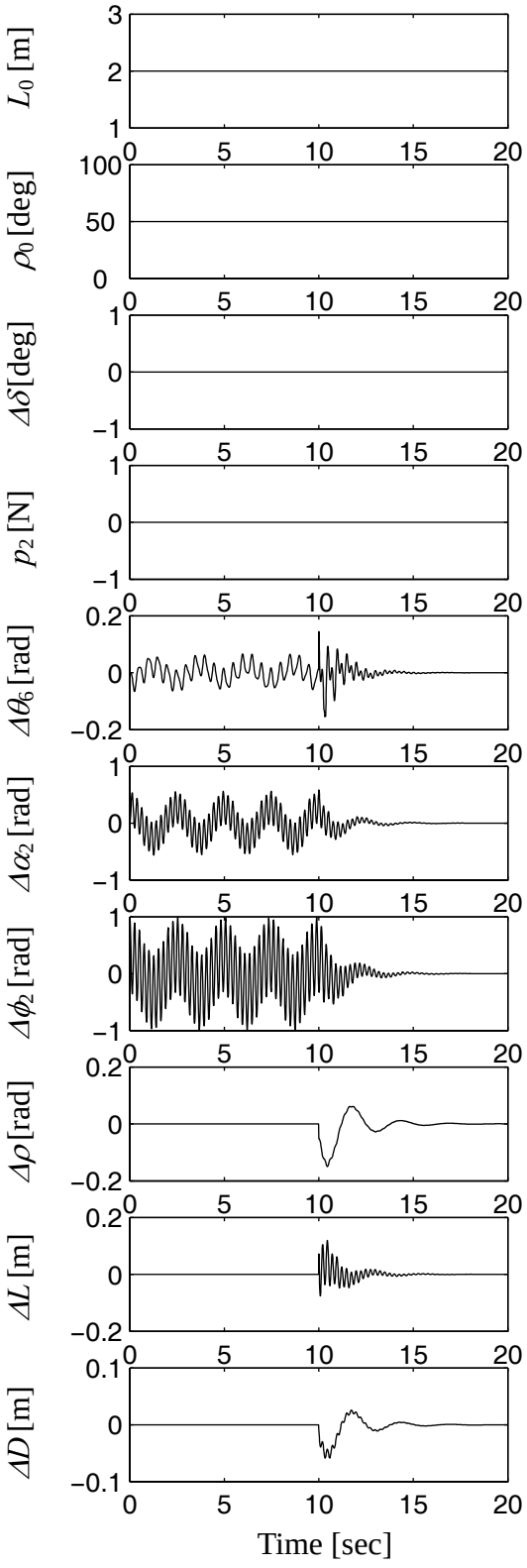

Figure 3.18: Constant cable length and constant luff angle with $\phi_2(0)$=1.0 rad. Control is turned ON at t=10 sec

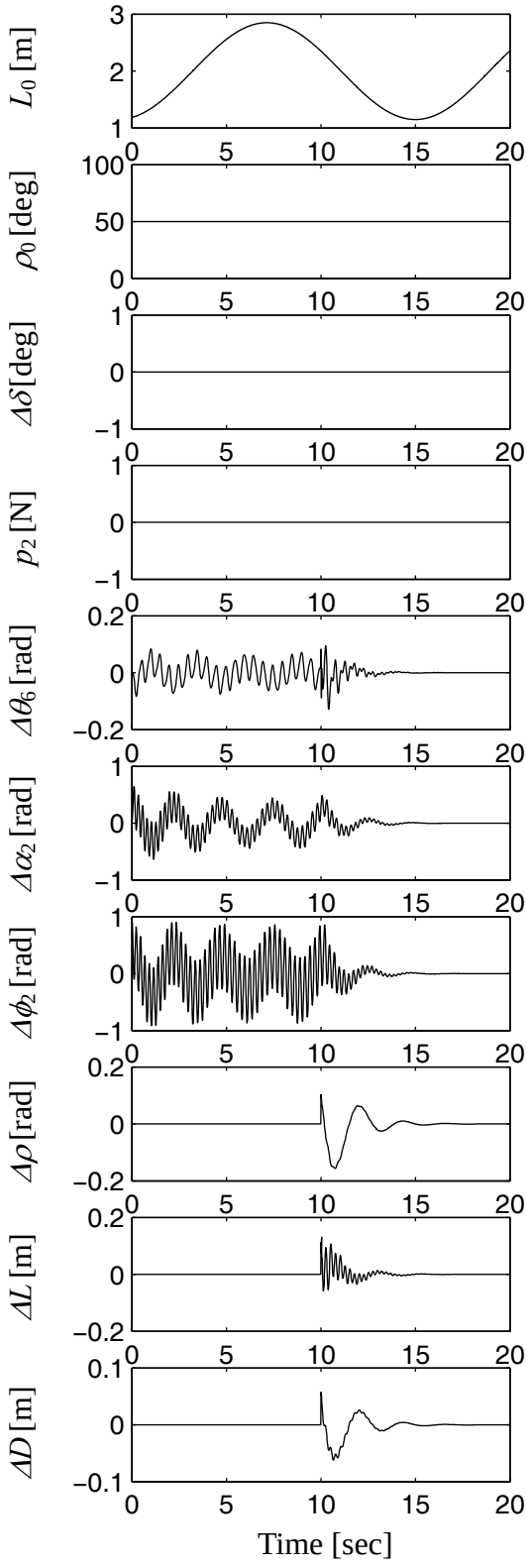

Figure 3.19: Variable cable length and constant luff angle with $\phi_2(0)$=1.0 rad. Control is turned ON at t=10 sec

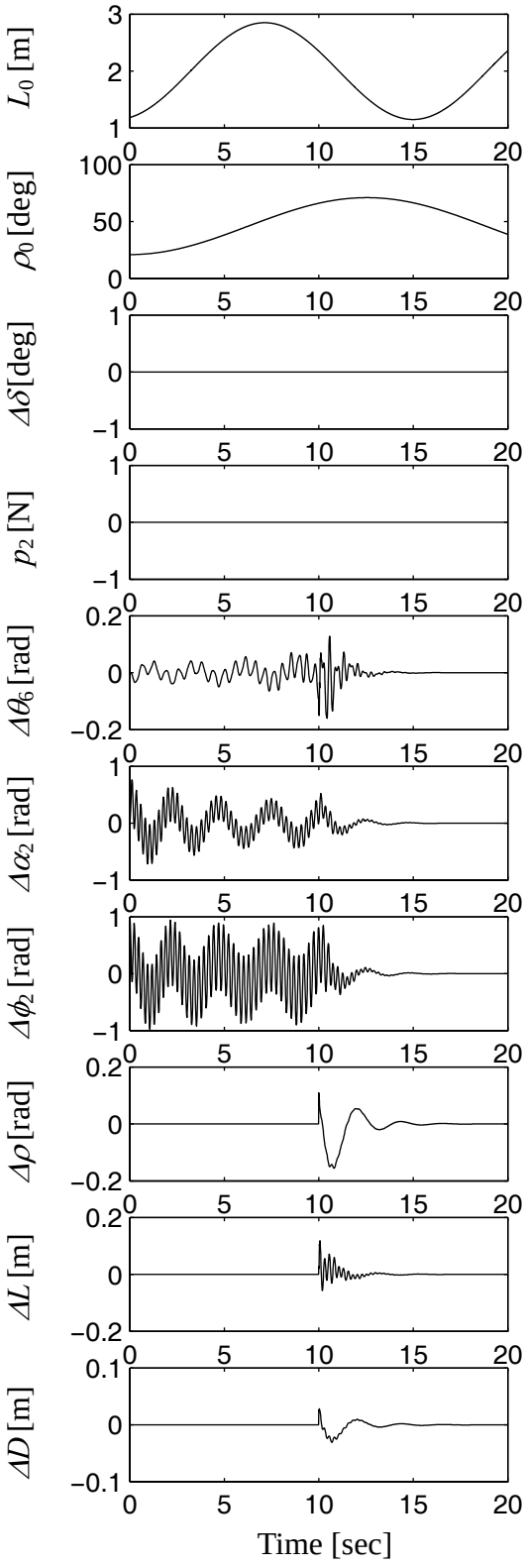

Figure 3.20: Variable cable length and variable luff angle with $\phi_2(0)$=1.0 rad. Control is turned ON at t=10 sec.

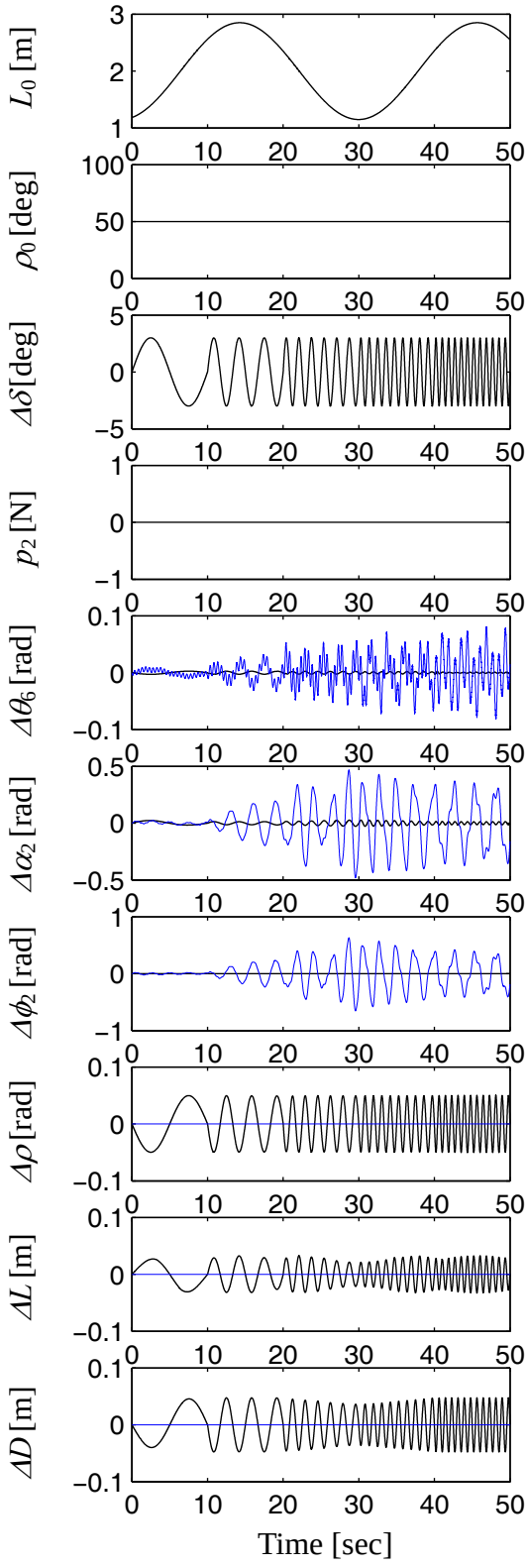

Figure 3.21: Variable cable length and constant luff angle with 3° sinusoidal rolling with variable frequency, — uncontrolled, — controlled

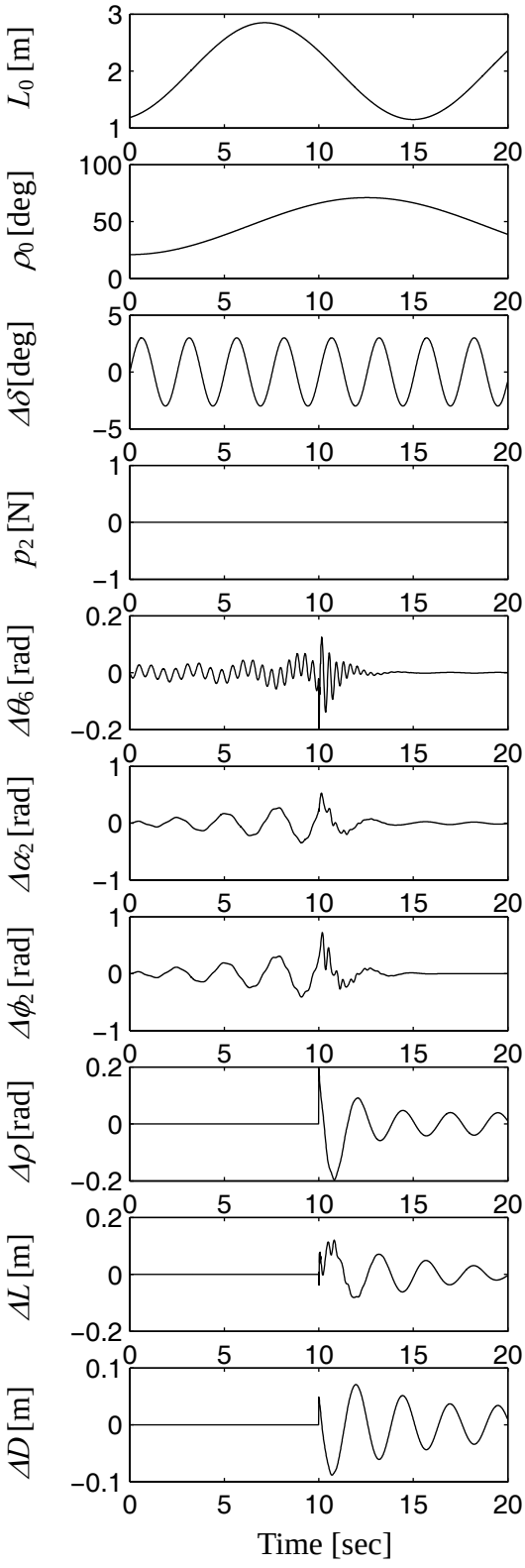

Figure 3.22: Variable cable length and variable luff angle with 3° sinusoidal rolling at the average value of the first eigenfrequency.
Control is turned ON at t=10 sec.

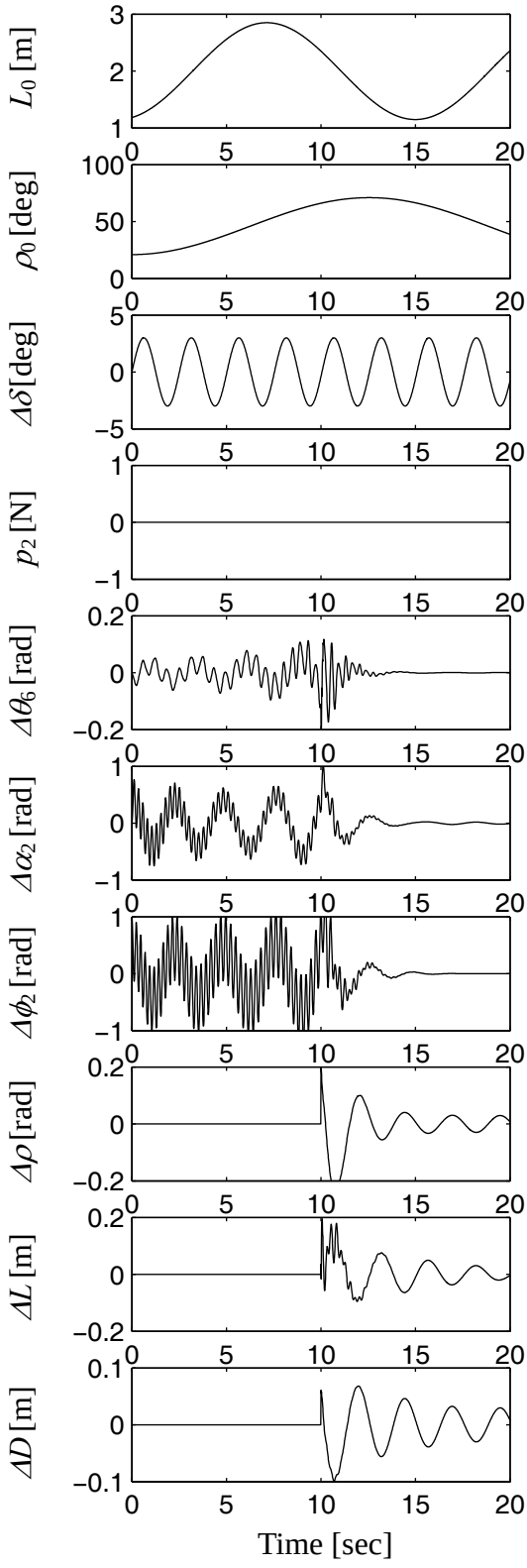

Figure 3.23: Variable cable length and variable luff angle with $\phi_2(0)$=1.0 rad and 3° sinusoidal rolling at the average value of the first eigenfrequency.
Control is turned ON at t=10 sec.

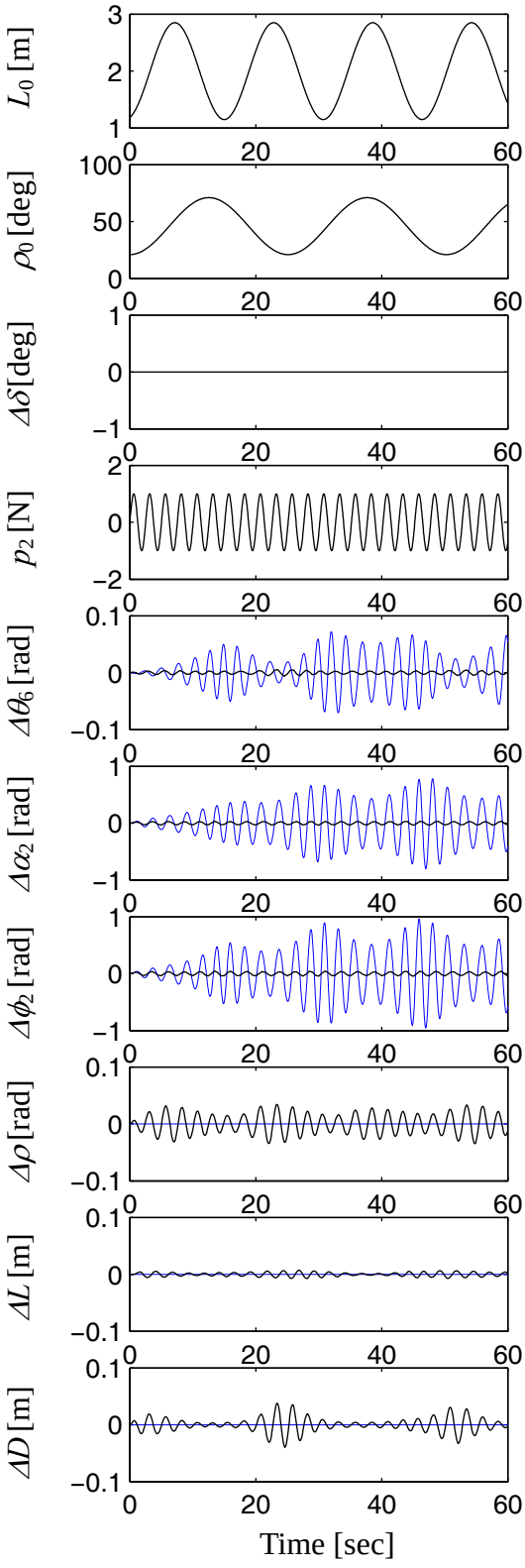

Figure 3.24: Variable cable length and variable luff angle with a sinusoidal disturbing force close to the first eigenfrequency,
— uncontrolled, — controlled

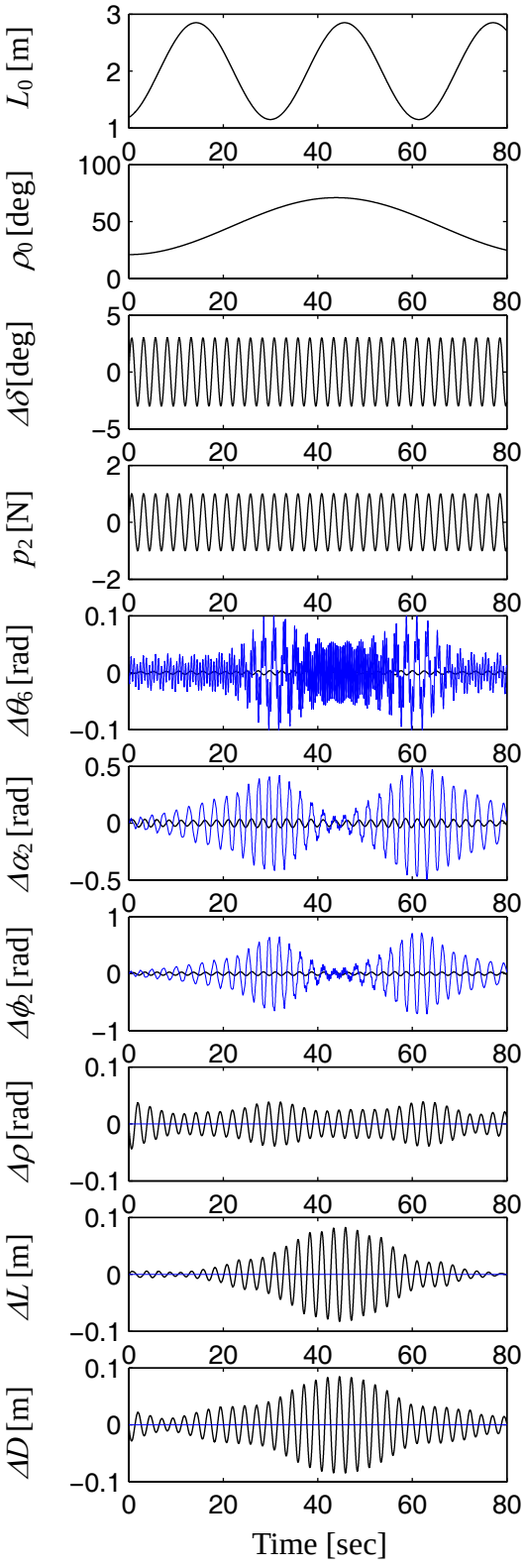

Figure 3.25: Variable cable length and variable luff angle with 3° sinusoidal rolling and a sinusoidal disturbing force close to the first eigenfrequency,
— uncontrolled, — controlled

Also, the control system is simulated for a chaotic rolling disturbance with a dominant frequency close to the first eigenfrequency of the crane (0.4 Hz). Here the chaotic rolling motion is generated using the Chua's equations set which is one of the popular tools for producing such signal. A general dimensionless state equation for a Chua's Oscillator is given as [Sha03]

$$\begin{aligned}\dot{\vartheta}_1 &= k\alpha(\vartheta_2 - \vartheta_1 - f(\vartheta))\\ \dot{\vartheta}_2 &= k(\vartheta_1 - \vartheta_2 + \vartheta_3)\\ \dot{\vartheta}_3 &= k(-\sigma\vartheta_2 - \gamma\vartheta_3)\end{aligned} \tag{3.48}$$

with

$$f(\vartheta) = b\vartheta_1 + \frac{1}{2}(a-b)\{|\vartheta_1 + 1| - |\vartheta_1 - 1|\}, \tag{3.49}$$

where α, σ, γ, a, b, and k are constant parameters. For the selection: α = 15.6, σ = 28.58, γ = 0, a = –1.14286, b = -0.714286, k = 1, with the initial conditions $\vartheta_1(0)$ = 1.16346, $\vartheta_2(0)$ = –0.4972335, and $\vartheta_3(0)$ = –0.905656, the solution of Chua's equations for $\vartheta_1(t)$ is chaotic. Therefore, the rolling excitation is chosen as

$$\Delta\delta(t) = p\,\vartheta_1(t), \tag{3.50}$$

where p is constant; it's value determines the amplitude of the chaotic rolling. The numerical solution of the above three equations for the first 20 seconds is displayed in Fig. 3.26 bellow.

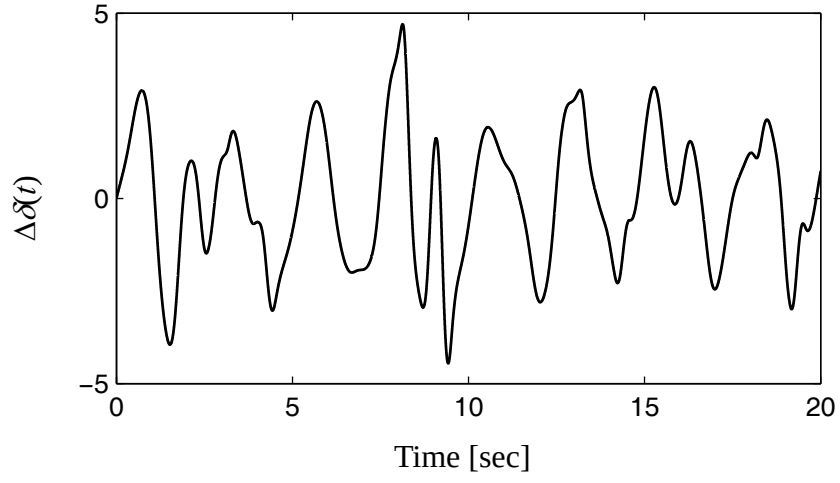

Figure 3.26: Chaotic rolling displacement

The dominant frequency (0.4 Hz) of the chaotic signal can be ensured using the fast Fourier transform function which is available in MATLAB. The controlled and uncontrolled responses due to chaotic rolling excitation of the ship are shown in Fig. 3.27, it can be recognized that the measured oscillations can increase significantly if no control is used, and they are well suppressed when the controller is used. In Fig. 3.28 the payload is subjected to horizontal pulses while the crane is excited by the chaotic rolling, it can be seen that both parts of the controller (the rolling compensation part and the optimal part) perform very well as obtained for the case of sinusoidal rolling excitation.

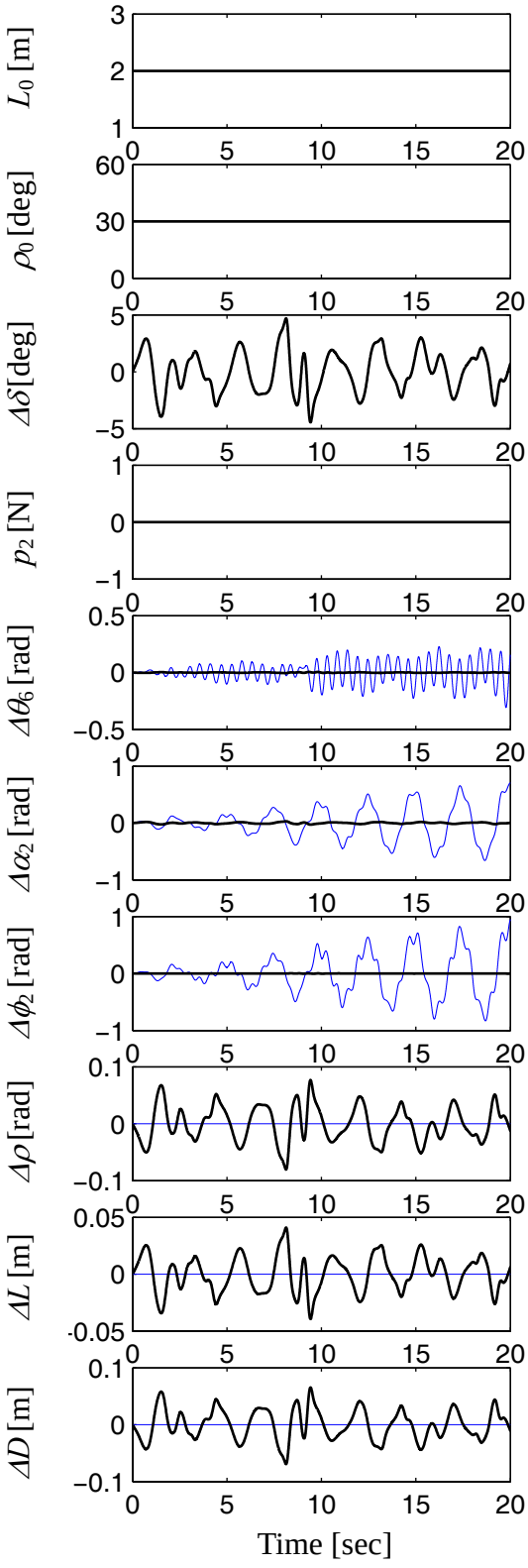

Figure 3.27: Comparison between controlled and uncontrolled responses for chaotic rolling of the ship,
— uncontrolled, — controlled

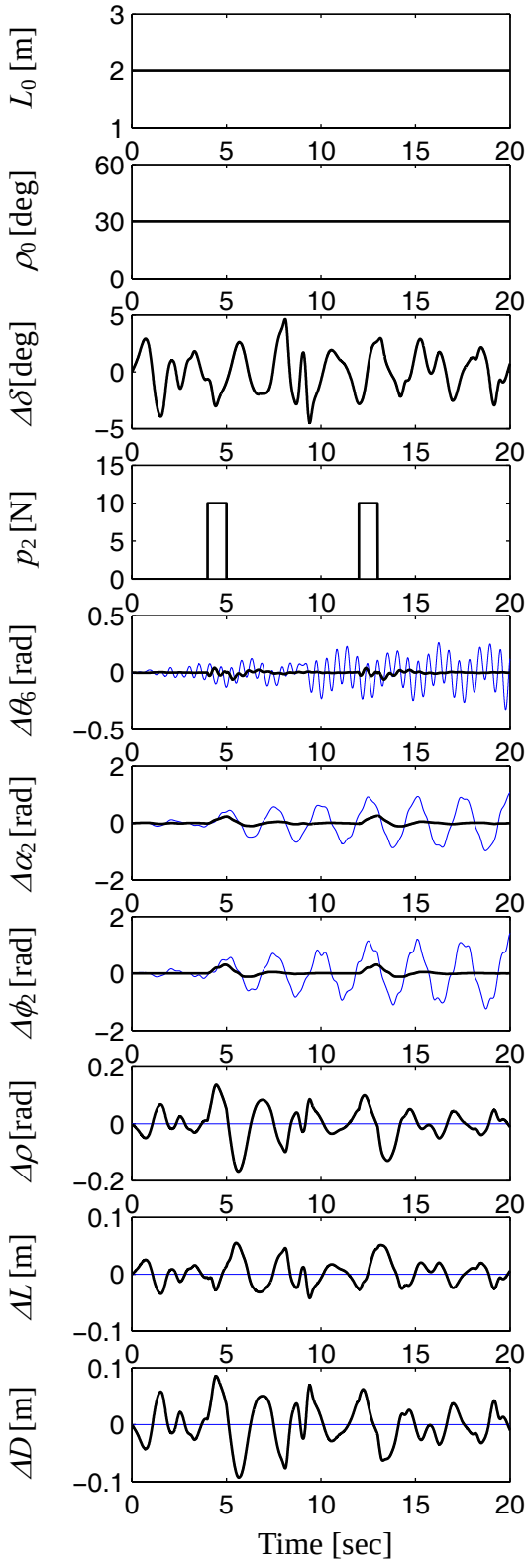

Figure 3.28: Comparison between controlled and uncontrolled responses for chaotic rolling and pulse forces acting on the payload,
— uncontrolled, — controlled

4 Experimental setup and results

This chapter concerns the experimental validation of the mathematical model and simulation results obtained in the previous chapters. A scaled test rig is designed and constructed to simulate the operation of an actual elastic ship-mounted crane at sea. The PI-observer and the model-based controller are implemented using a dSPACE system of adequate processor speed.

4.1 Description of the test rig

The constructed test rig is shown in Fig. 4.1. It has the following inputs:

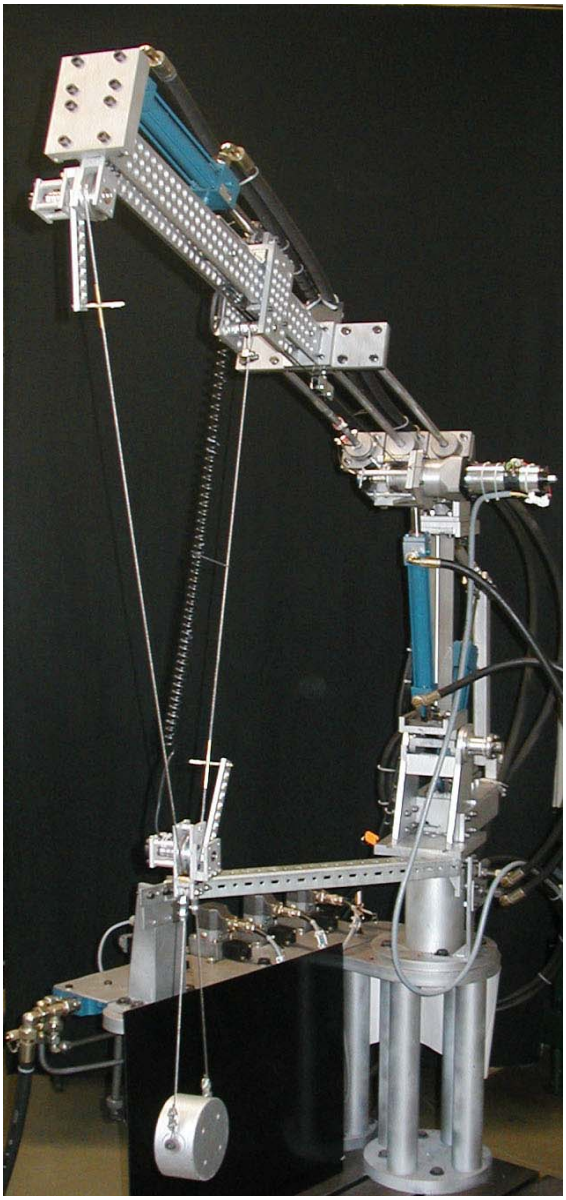

Figure 4.1: Picture of the constructed test rig

(1) The position of the lower suspension point $D(t)$: is controlled using a hydraulic cylinder mounted between the lower suspension point and the tip of the boom (Fig. 4.2). The lower suspension point runs on a practically frictionless linear guide fixed on the upper part of the boom. The displacement $\Delta D(t)$ is measured by a linear incremental encoder as shown in Fig. 4.3.

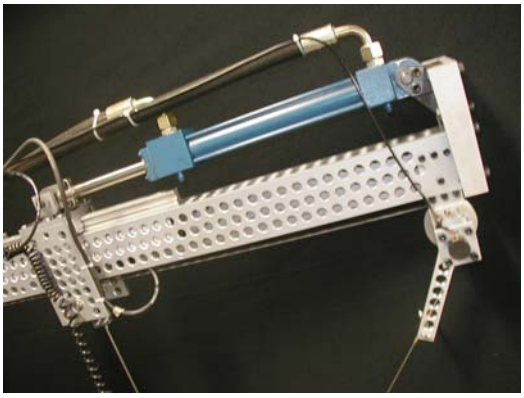

Figure 4.2: Actuator for $D(t)$

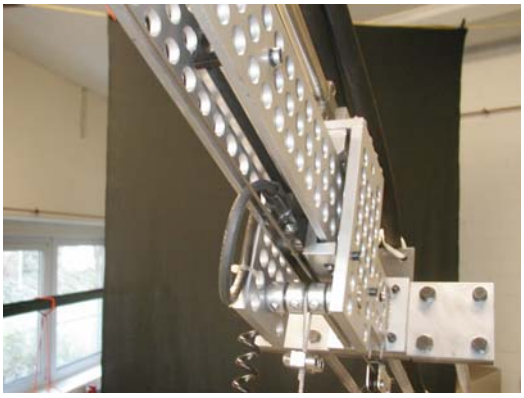

Figure 4.3: Incremental encoder for $D(t)$

(2) The luff angle of the elastic boom $\rho(t)$: The luff angle is controlled by a hydraulic cylinder as shown in Fig. 4.4. The angle is measured using a rotary potentiometer mounted on the luff joint as in Fig. 4.5.

Figure 4.4: Actuator for $\rho(t)$

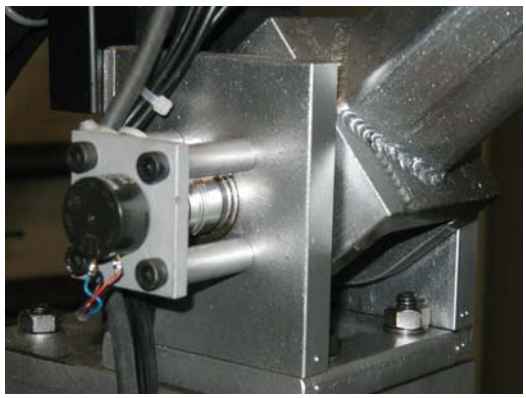

Figure 4.5: Measurement of $\rho(t)$

(3) The length of the upper cable $L(t)$: is controlled by a DC motor integrated with a spur gear box. The cable is wound around a drum driven by the motor as shown in Fig. 4.6. The change in length of the cable $\Delta L(t)$ is measured using a 10 turns rotary potentiometer (measurement range: 0-3600°) connected to the drum as shown in Fig. 4.7.

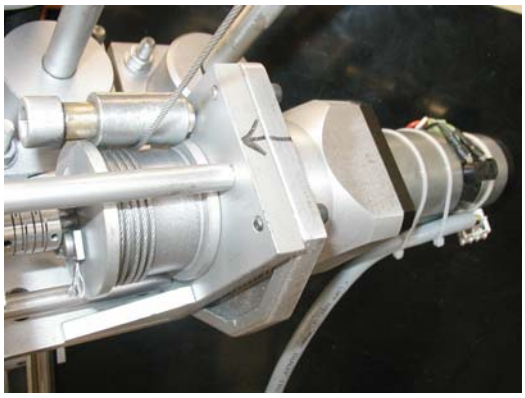

Figure 4.6: Actuator for $L(t)$

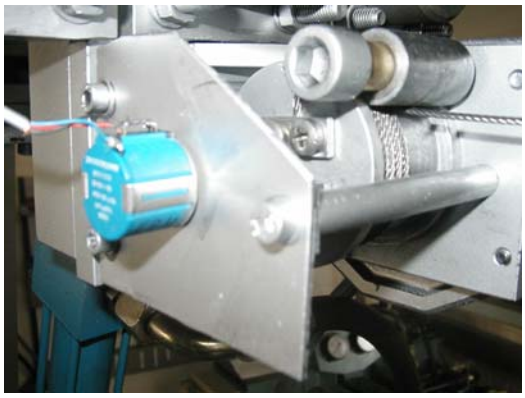

Figure 4.7: Measurement of $L(t)$

(4) The rolling displacement of the crane (input disturbance): the rolling excitation of the crane $\Delta\delta(t)$ due to sea motion is realized by a hydraulic cylinder (Fig. 4.8) which swings the entire crane structure around the designed roll center. In reality, this angle can be measured using a tilt sensor or a gyroscope mounted on the ship. Here, it is measured using a rotary potentiometer mounted on the roll joint as shown in Fig. 4.9.

Figure 4.8: Actuator for rolling

Figure 4.9: Measurement of rolling

In addition to the mentioned inputs and their measuring instruments, three output variables $\Delta\theta_6$, $\Delta\alpha_2$, and $\Delta\phi_2$ must be known to guarantee the observability condition of the crane and payload. The elastic rotational displacement θ_6 is measured directly by a strain gauge glued to the elastic boom as shown in Fig. 4.10. The remaining two angles $\Delta\alpha_2$ and $\Delta\phi_2$ are measured indirectly using two rotary potentiometers equipped with lightweight aluminum levers. The first potentiometer measures the angle η_1 at the upper suspension point between segment L_2 of the upper cable and the rigid part BC of the boom as shown in Fig. 4.11. When the cable swings around the upper suspension point, the aluminum lever swings with it and rotates the rod of the potentiometer, which gives an output voltage proportional to the absolute value of the angle η_1.

Figure 4.10: Strain gauge for measuring the elastic rotational displacement

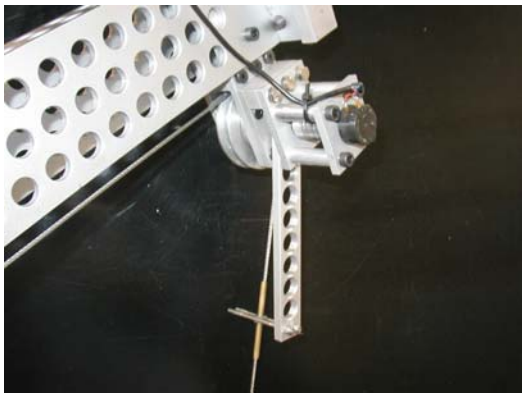

Figure 4.11: Measurement of the cable swinging angle η_1 with the boom

The second potentiometer measures the angle η_2 between the payload cable l and the segment L_2 of the upper cable as shown in Fig. 4.12. Here the aluminum lever, connected to the potentiometer rod, swings with L_2 and the potentiometer body is mounted on the pulley housing such that it rotates with the pendulation angle $\Delta\phi_2$ of the payload cable l. Accordingly, the potentiometer gives a measure of the relative angle between L_2 and l. A flexile spiral cable is used to transmit the output voltage from the potentiometer to the controller.

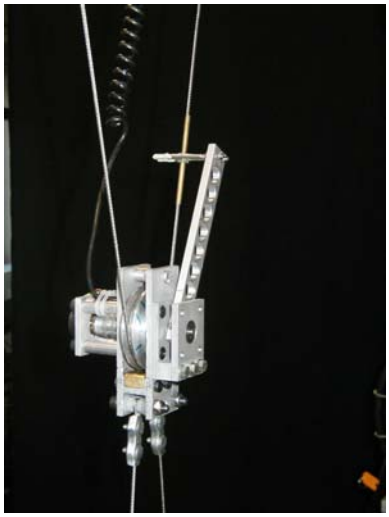

Figure 4.12: Measurement of η_2

The five potentiometers are supplied with a reference voltage of 10 volts obtained from a constant voltage supply unit as shown in Fig. 4.13. The measuring instruments (the potentiometers and the linear incremental encoder) are connected to the controller (dSPACE processor) through a connection block with MIMO channels (Fig. 4.14).

Figure 4.13: Constant voltage supply unit

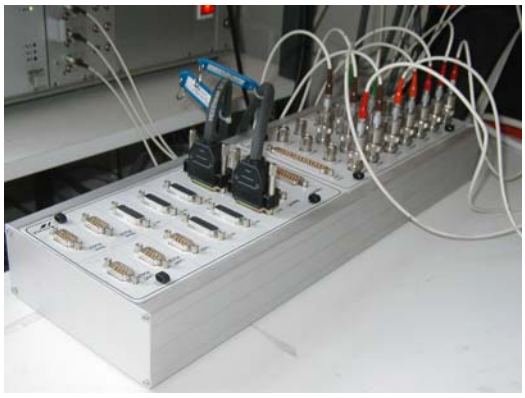

Figure 4.14: dSPACE connection block with MIMO channels

The strain gauge is connected to the controller connection block through a strain gauge amplifier (Fig. 4.15) which transforms the mechanical strain into a voltage. The DC motor is energized by a power amplifier (Fig. 4.16) which amplifies the command signal coming from the dSPACE.

Figure 4.15: Strain gauge amplifier

Figure 4.16: Power amplifier for the DC motor

The three hydraulic cylinders are activated by three servo valves mounted on the test rig as shown in Fig. 4.17. These servo valves are energized by the controller through a three channels servo valve signal amplifier as shown in Fig. 4.18.

Figure 4.17: The three servo valves

Figure 4.18: Servo valve signal amplifier

The required oil pressure and flow rate are supplied to the system by a hydraulic pump of adequate capacity as shown in Fig. 4.19.

Figure 4.19: The hydraulic pump

The dSPACE controller is programmed by MATLAB SIMULINK which includes the multi model PI-Observer and the variable-gain controller. Each actuator of the crane is controlled by a PD-tracking controller to ensure that the actuators track the input commands (desired displacements) coming from the MIMO variable-gain controller as illustrated in Fig. 4.20.

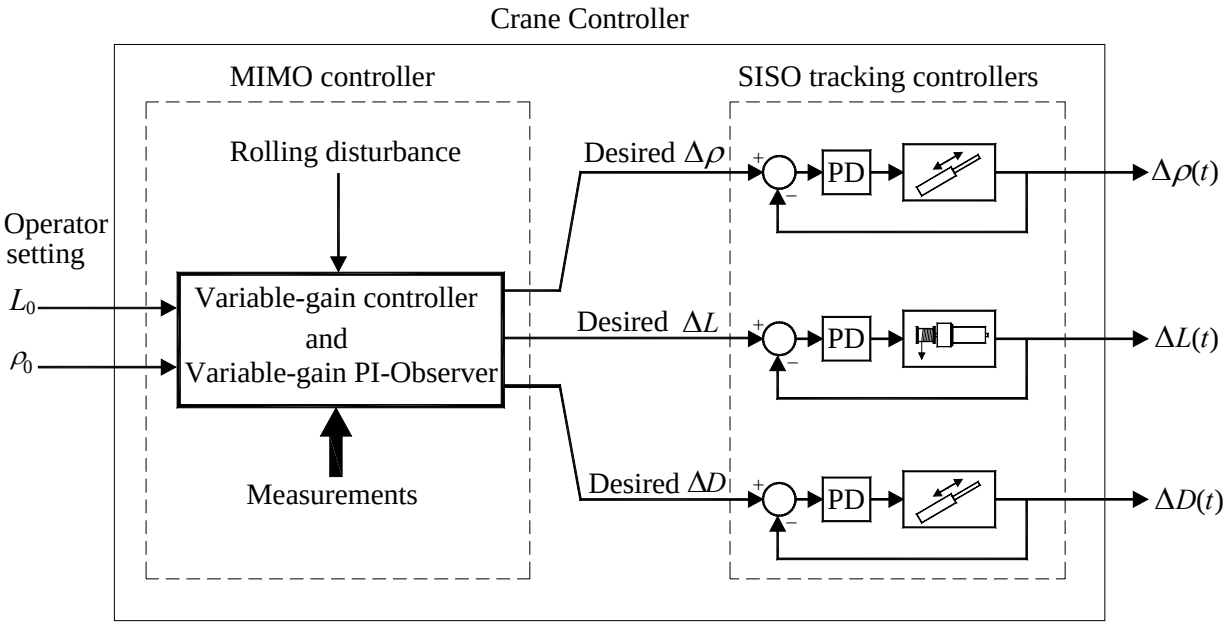

Figure 4.20: Block diagram of the PD-tracking controllers to realize the inputs

The measurements η_1 and η_2 are described in Fig. 4.21. Accordingly, the vector $[\Delta\theta_6 \quad \Delta\alpha_2 \quad \Delta\phi_2]^T$ can be easily computed from the available measurements $[\theta_6 \quad \eta_1 \quad \eta_2]^T$ such that

$$\eta_1 = \alpha_2 - \psi \tag{4.1}$$

$$\eta_2 = \alpha_2 + \frac{\pi}{2} - \phi_2. \tag{4.2}$$

Solving the above two equations for α_2 and ϕ_2 gives

$$\begin{aligned} \alpha_2 &= \eta_1 + \psi \\ &= \eta_1 + \rho + \Delta\delta + \theta_6 \end{aligned} \tag{4.3}$$

and

$$\begin{aligned} \phi_2 &= \eta_1 - \eta_2 + \psi + \pi/2 \\ &= \eta_1 - \eta_2 + \rho + \Delta\delta + \theta_6 + \pi/2. \end{aligned} \tag{4.4}$$

Using Eqs. (4.3,4.4), the vector $[\Delta\theta_6\ \Delta\alpha_2\ \Delta\phi_2]^T$ can be expressed in compact form as

$$\underbrace{\begin{bmatrix}\Delta\theta_6\\ \Delta\alpha_2\\ \Delta\phi_2\end{bmatrix}}_{\boldsymbol{y}_m} = \begin{bmatrix}1 & 0 & 0\\ 1 & 1 & 0\\ 1 & 1 & -1\end{bmatrix} \underbrace{\begin{bmatrix}\theta_6\\ \eta_1\\ \eta_2\end{bmatrix}}_{\text{measured}} + \begin{bmatrix}0 & 0\\ 1 & 1\\ 1 & 1\end{bmatrix} \underbrace{\begin{bmatrix}\rho\\ \Delta\delta\end{bmatrix}}_{\text{measured}} - \underbrace{\begin{bmatrix}\theta_{60}\\ \alpha_{20}\\ -\pi/2\end{bmatrix}}_{\text{known}}. \tag{4.5}$$

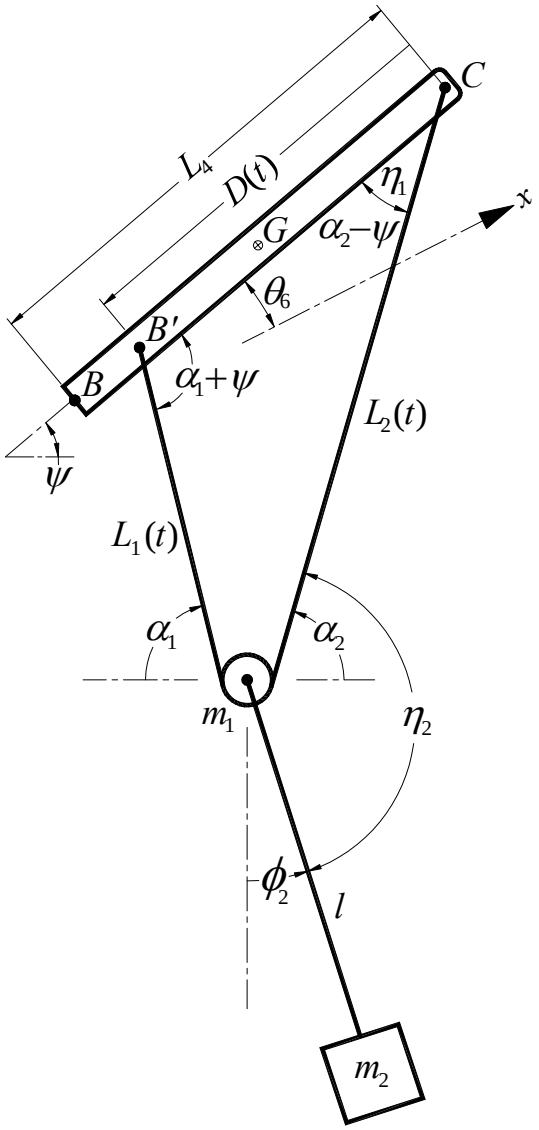

Figure 4.21: Description of the measurements η_1 and η_2

4.2 Experimental results

Three sets of experiments were carried out to validate the model and the controller for the expected operation conditions of a real crane at sea. In the first set, the open loop response of the crane is measured for a predetermined initial condition and rolling excitation, the experimental results are then compared with those results obtained by simulation to check the validity of the derived mathematical model.

In the second set, the crane was subjected to sinusoidal and chaotic rolling excitation in the neighborhood of the first eigenfrequency of the crane, in the uncontrolled case, this excitation caused the amplitude of measurements to grow rapidly to a dangerous level. Consequently, the experiment had to be stopped after the first 9-11 seconds. This set was repeated for different luff angles and cable lengths (different models) in order to test the operation of the region finder and the behavior of the variable-gain observer and controller.

In the third set, the crane was given a nonzero initial condition and allowed to vibrate without control and then the experiment was repeated with control. This gave a measure of the damping created in the crane by the optimal state controller.

In the fourth set, the crane was subjected to a resonance sinusoidal rolling excitation with the controller turned ON, during this test (at $t \approx 3$ seconds) the payload was subjected to a considerable horizontal impact force (p_2) to check the ability of the controller to compensate for both effects at the same time.

These experiments were repeated for different payloads in order to test the robustness of the observer and controller with respect to the payload mass which is usually considered as an unknown parameter.

Experimental and simulation results for the open loop system are shown in Figs. (4.22-4.23). In the first figure, the payload is displaced horizontally by hand through 0.8 m and then released, it is clear that the simulation and experimental results are close to each other, the decrement of the succeeding amplitudes, observed in the experimental results, can be explained due to the coulomb and viscous frictions which are not considered in the model, this existing friction is also responsible for dampen out the higher mode oscillations which are noticed in the simulation results. In Figure 4.23 the open loop experimental and simulation results are shown for a sinusoidal rolling excitation.

In Figs. (4.24-4.31) the experimental results for a nominal payload mass (m_2=5.0 kg) are shown. In Fig. 4.24, the open loop and closed loop results for a cable length of 1.6 m with 30° luff angle are shown. Here the crane was subjected to a sinusoidal rolling

excitation close to the its first eigenfrequency. In Figure 4.25 the crane was excited by a chaotic rolling excitation as described by Eqs. (3.50-3.52). Figure 4.26 shows the results for hoisting the payload with a constant luff angle, and in Fig. 4.27 the closed loop response is considered for hoisting and then lowering the payload while keeping a constant luff angle. The effect of changing the luff angle on the response is shown in Fig. 4.28, and the effect of a nonzero initial condition on the response is shown in Fig. 4.29, here the payload is displaced horizontally by hand through 0.8 m and then released. Comparison between the controlled and uncontrolled responses shows that the controller can suppress the vibrations completely within 3 pendulation cycles of the payload while the open loop vibrations continued for a long time. The closed loop response for sinusoidal rolling excitation with a horizontal impact force applied directly to the payload at $t \approx 3.5$ seconds is shown in Fig. 4.30, the results show that the controller can significantly suppress the effect of rolling and other unknown disturbances at the same time. The ability of the controller to dampen out the elastic vibrations in the boom is tested by pushing the tip of the boom downward and then released, comparison between controlled and uncontrolled results are shown in Fig. 4.31; it can be recognized that the controller provided a significant damping in the boom and the elastic vibration amplitude has converged to zero after 3 oscillation periods.

The effect of using larger payload mass on the controlled response is shown in Figs. (4.32-4.36). Here the results belong to 8.0 kg payload (160% of the nominal value). Similarly, Figs. (4.37-4.41) show some experimental results for 1.0 kg payload (20% of the nominal value).

From the obtained experimental results, it is possible to recognize that the used control approach performed very good and created the necessary damping for the worst case of operating conditions when the crane is excited at the resonant frequency. Also, the experimental results for hoisting the payload and changing the luff angle (i.e., changing the model of the crane) proved that the used interpolation method, in which the observer and controller parameters are calculated in real time, guaranteed a smooth change of the controller and observer gains and a smooth switching between different operating regions, no chattering or unwanted second effect were observed. In addition, robustness of the controller and the observer due to changing the payload mass was demonstrated experimentally.

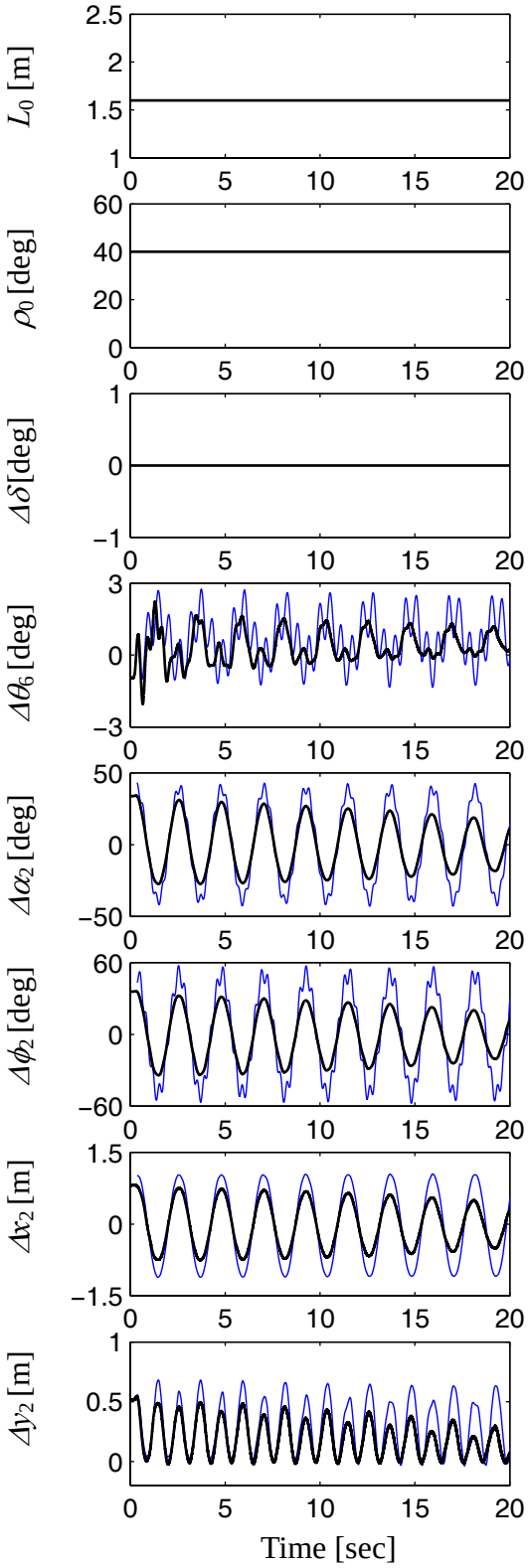

Figure 4.22: Simulation and experimental results for the open loop system due to the initial condition $\Delta x_2(0)$=0.8 m, m_2=5.0 kg,
— simulation, — experiment

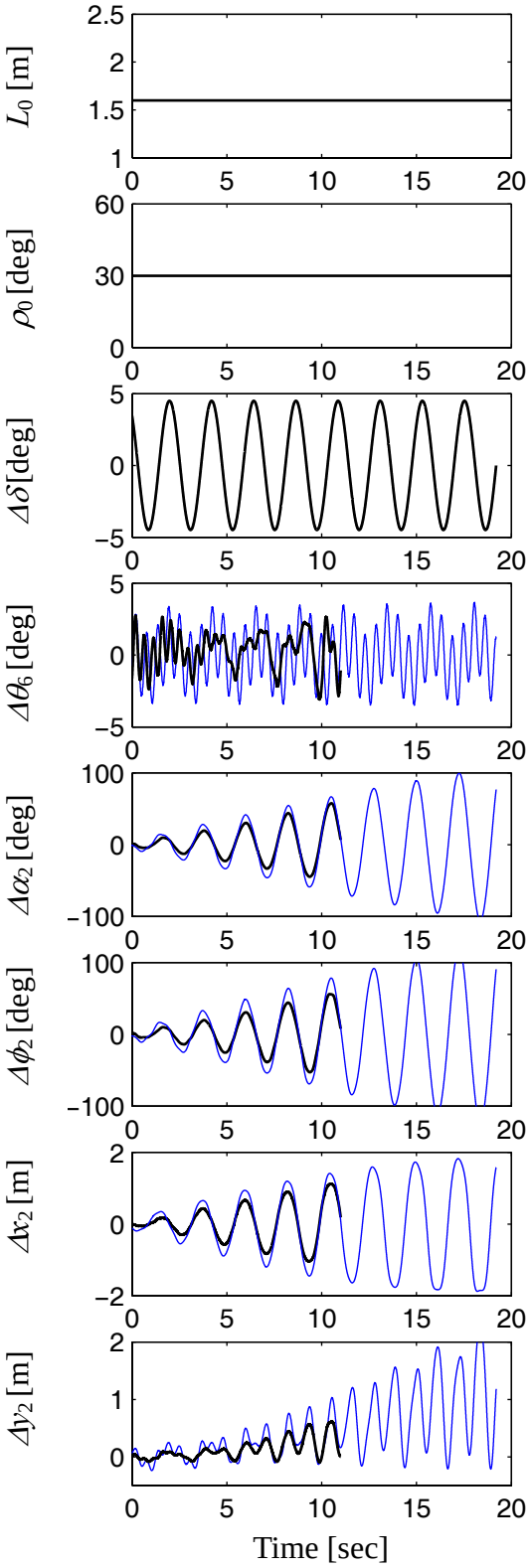

Figure 4.23: Simulation and experimental results for the open loop system due to rolling close to the first eigenvalue of the crane. m_2=5.0 kg
— simulation, — experiment

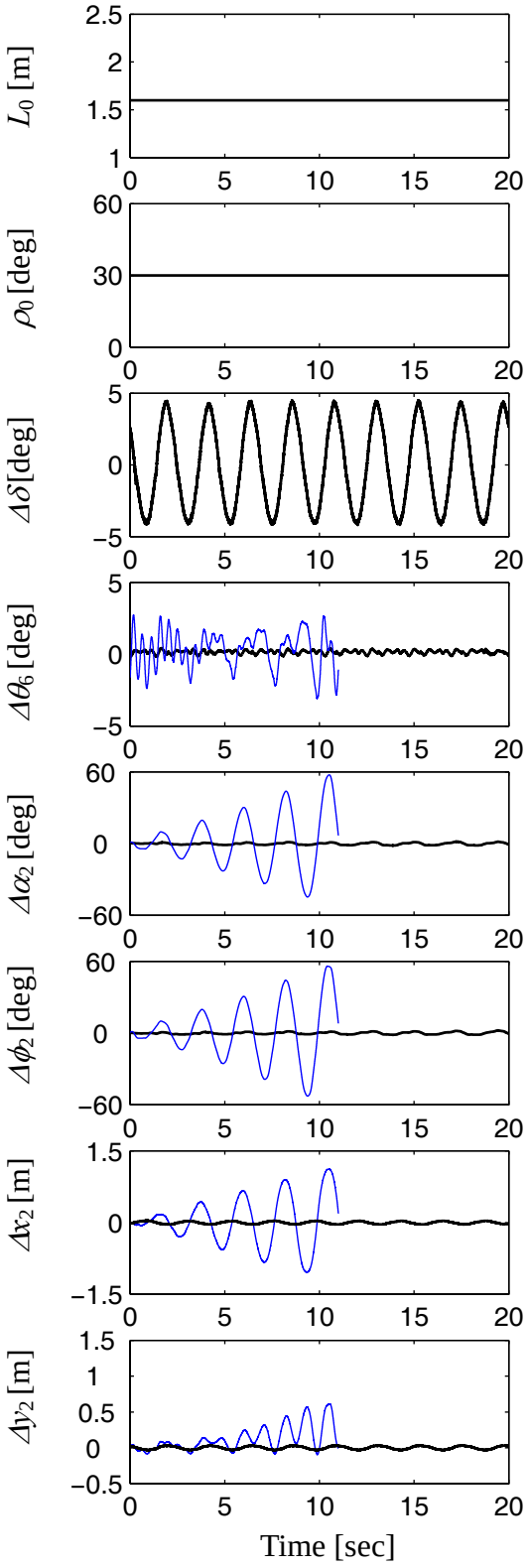

Figure 4.24: Constant cable length and constant luff angle with sinusoidal rolling close to the first eigenfrequency, m_2=5.0 kg,
— uncontrolled, — controlled

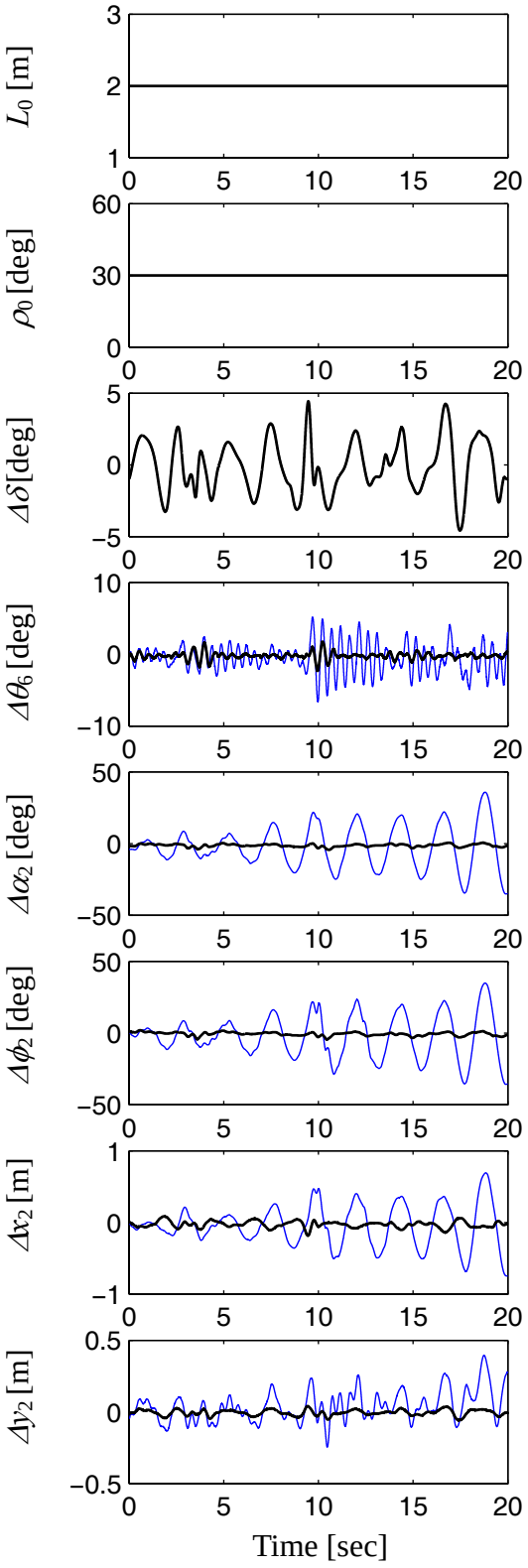

Figure 4.25: Response due to chaotic rolling excitation with a dominant frequency close to the first eigenvalue of the crane. m_2=5.0 kg
— uncontrolled, — controlled

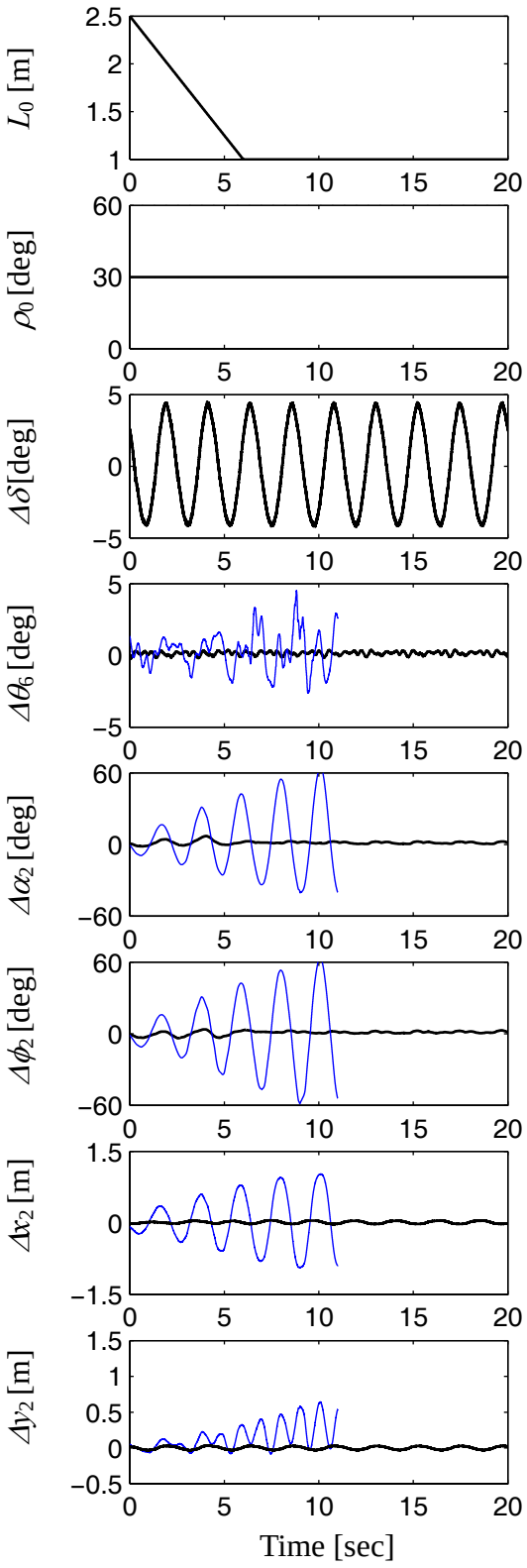

Figure 4.26: Variable cable length (payload hoisting) and constant luff angle with sinusoidal rolling the close to the first eigenfrequency, m_2=5.0 kg, — uncontrolled, — controlled

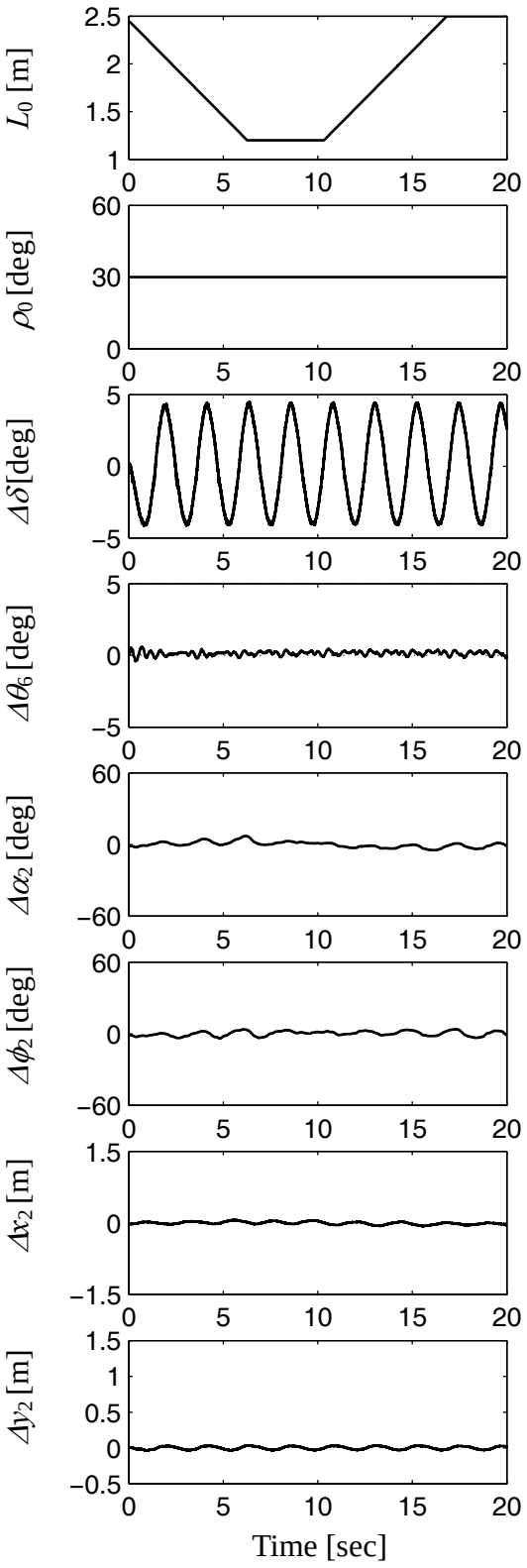

Figure 4.27: Controlled response for variable cable length and constant luff angle with sinusoidal rolling in the close to the first eigenfrequency, m_2=5.0 kg

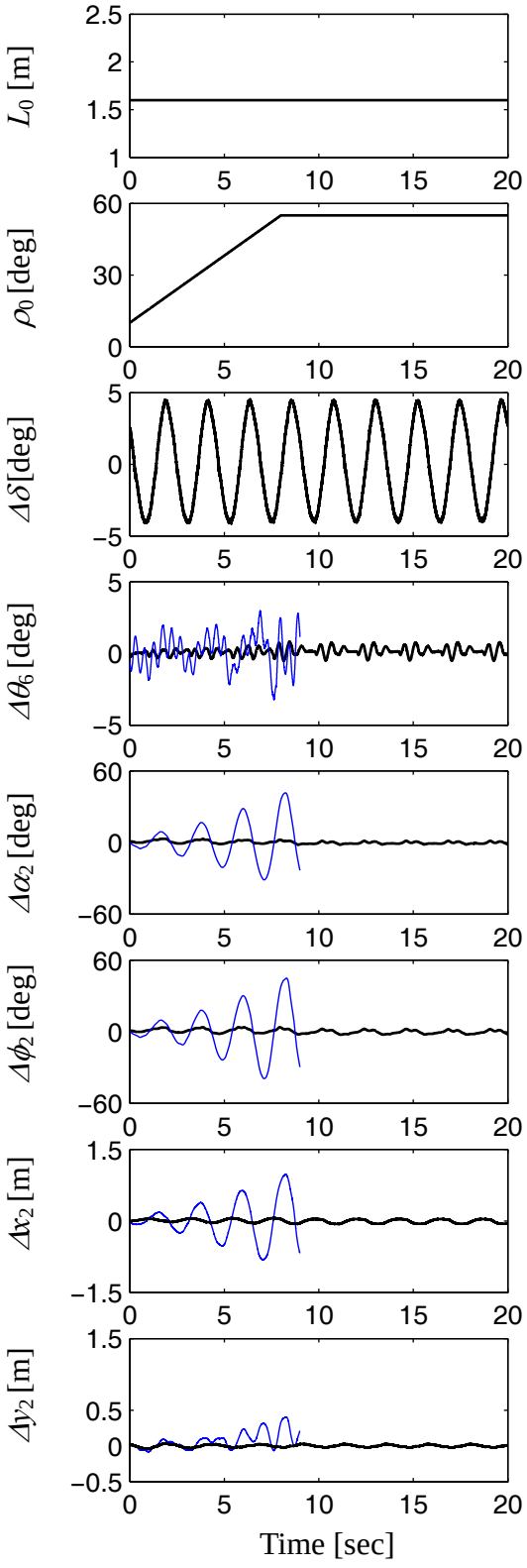

Figure 4.28: Constant cable length and variable luff angle with sinusoidal rolling close to the first eigenfrequency, m_2=5.0 kg,
— uncontrolled, — controlled

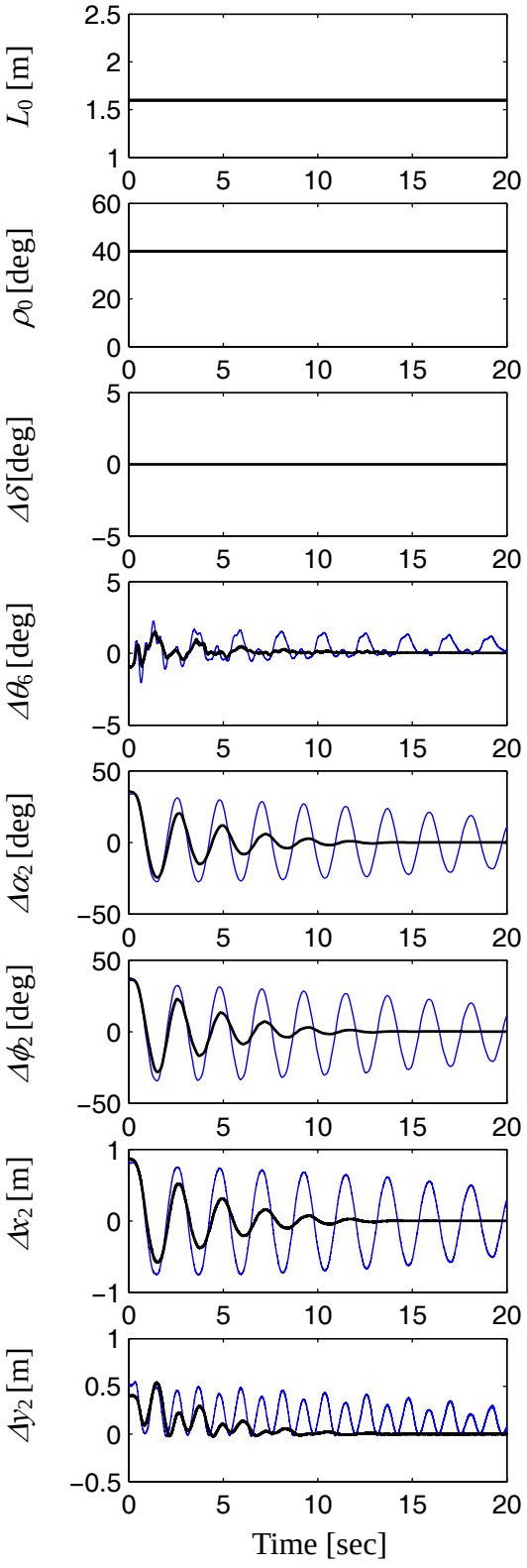

Figure 4.29: Response due to non zero initial condition $\Delta x_2(0)$=0.8 m, m_2=5.0 kg,
— uncontrolled, — controlled

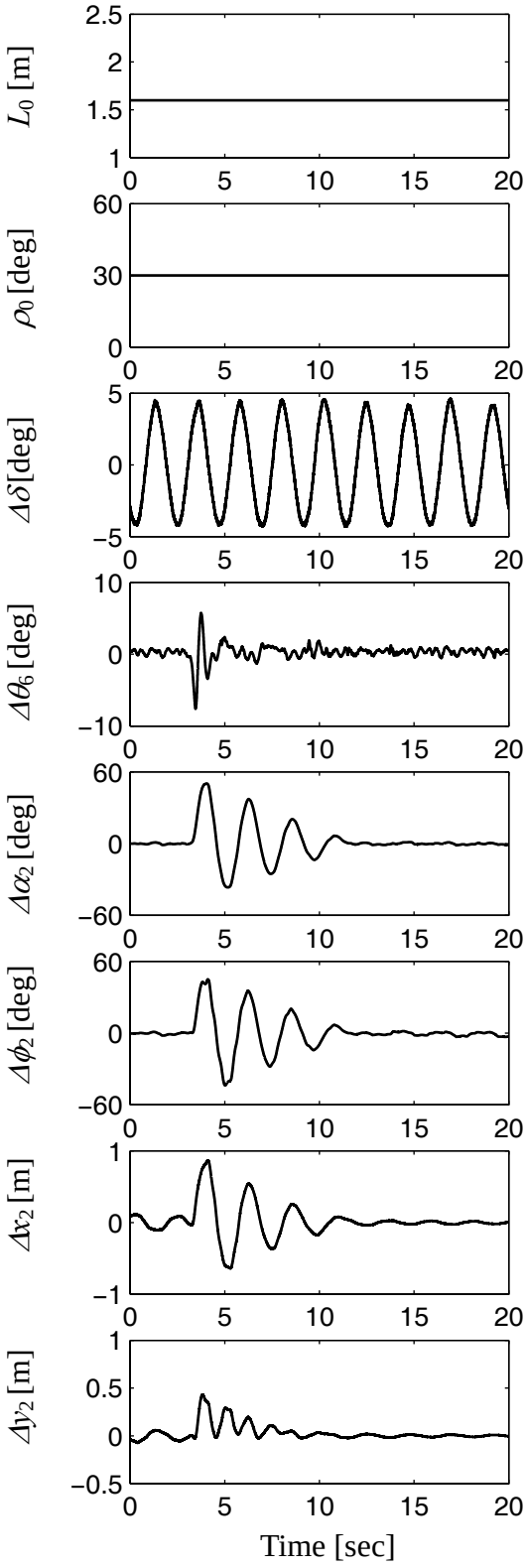

Figure 4.30: Controlled response due to rolling and a horizontal impact force applied to the payload at $t \approx 3.5$ seconds, m_2=5.0 kg

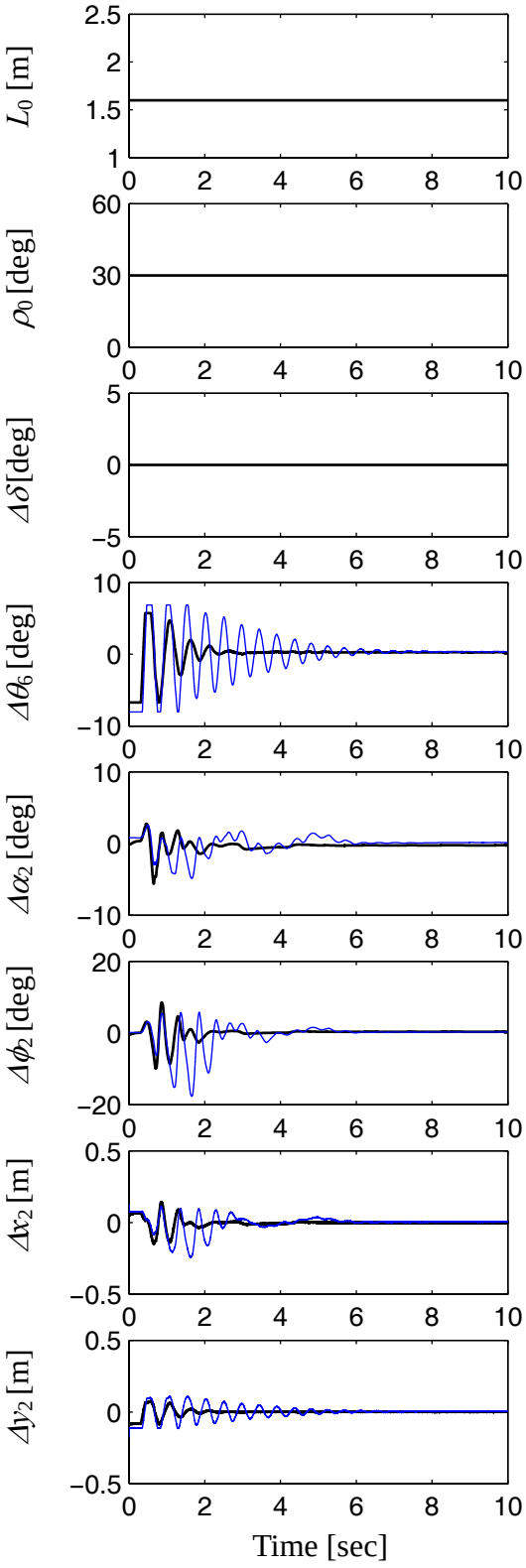

Figure 4.31: Response due to a nonzero initial condition of the elastic boom, the boom is deflected downward by hand and then released, m_2=5.0 kg, — uncontrolled, — controlled

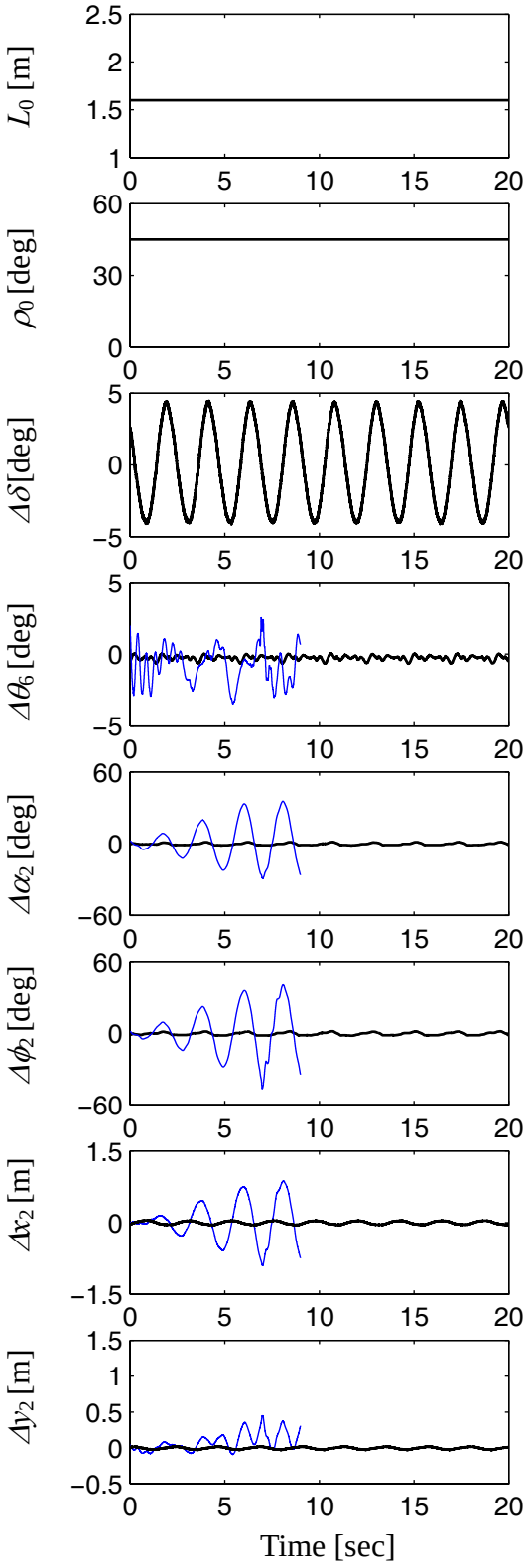

Figure 4.32: Constant cable length and constant luff angle with sinusoidal rolling close to the first eigenfrequency, m_2=8.0 kg,
— uncontrolled, — controlled

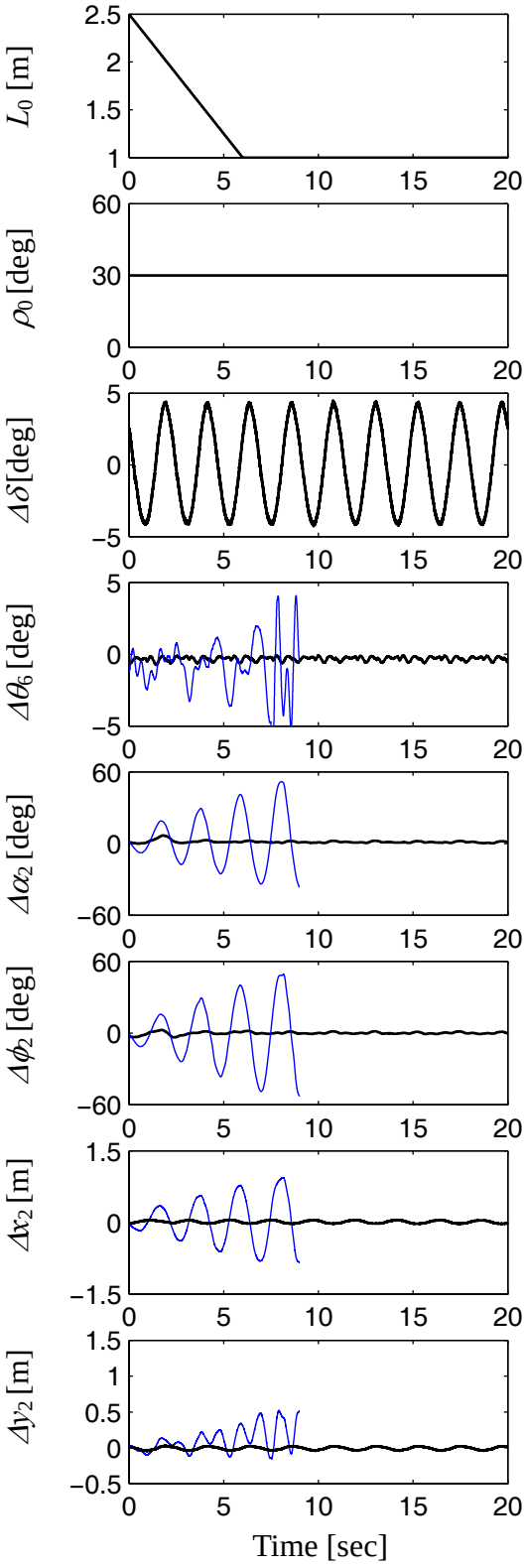

Figure 4.33: Variable cable length and constant luff angle with sinusoidal rolling close to the first eigenfrequency, m_2=8.0 kg,
— uncontrolled, — controlled

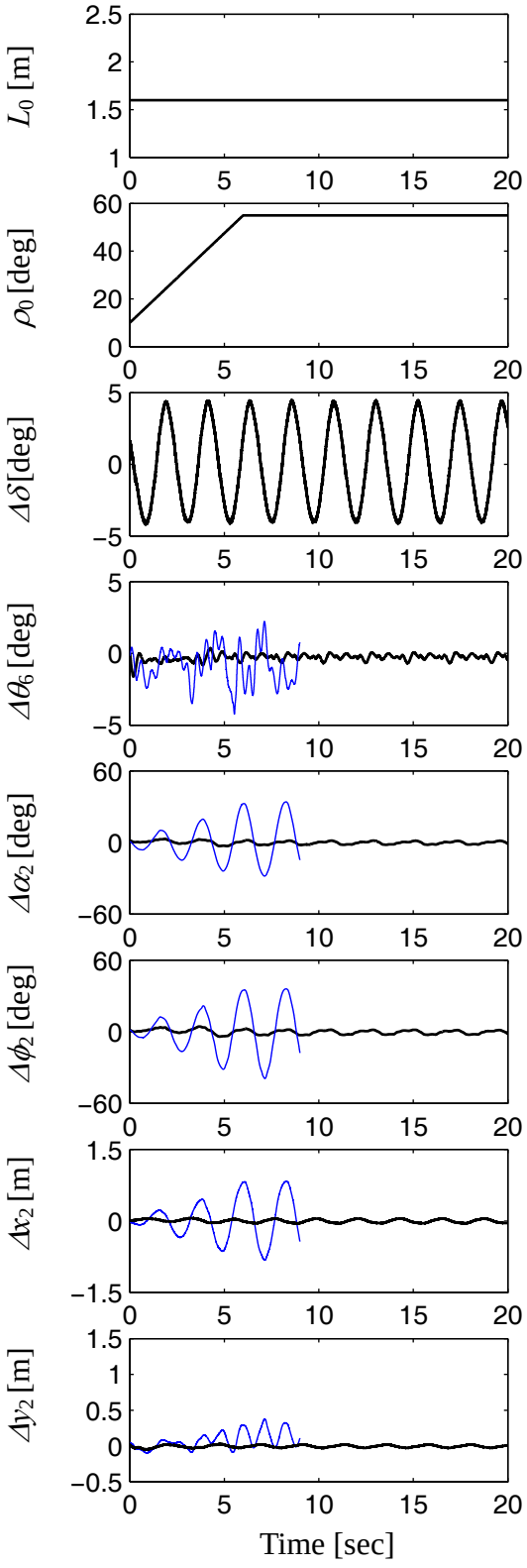

Figure 4.34: Constant cable length and variable luff angle with sinusoidal rolling close to the first eigenfrequency, m_2=8.0 kg,
— uncontrolled, — controlled

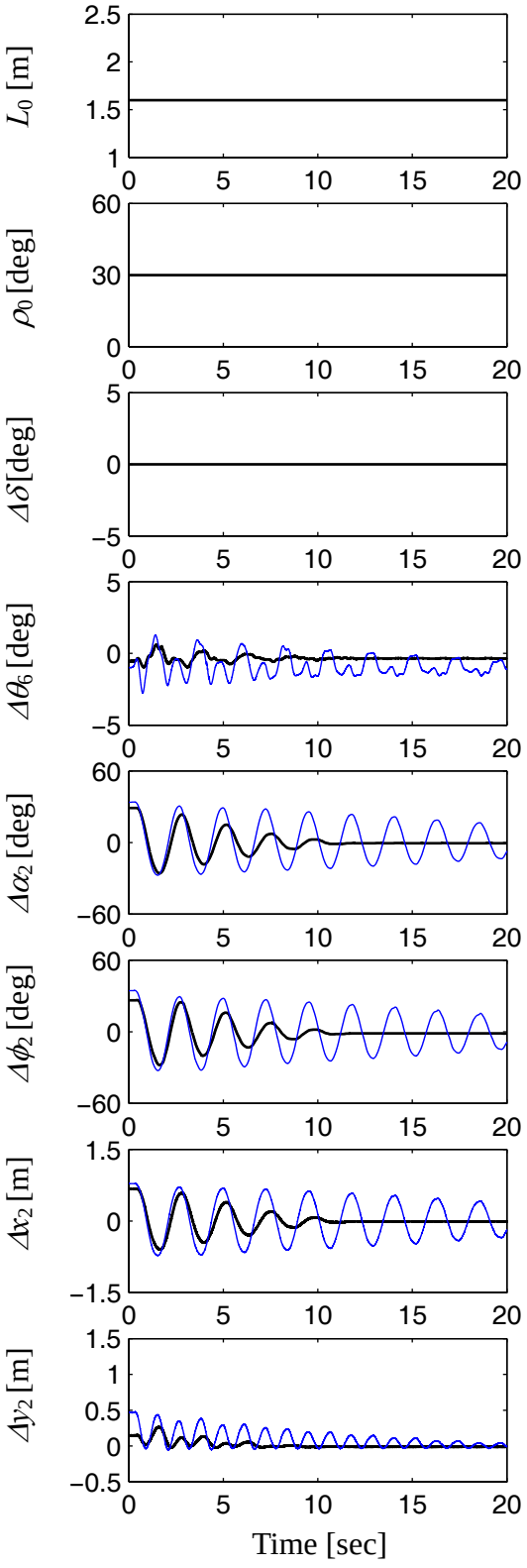

Figure 4.35: Response due to nonzero initial condition $\Delta x_2(0)$=0.7 m, m_2=8.0 kg,
— uncontrolled, — controlled

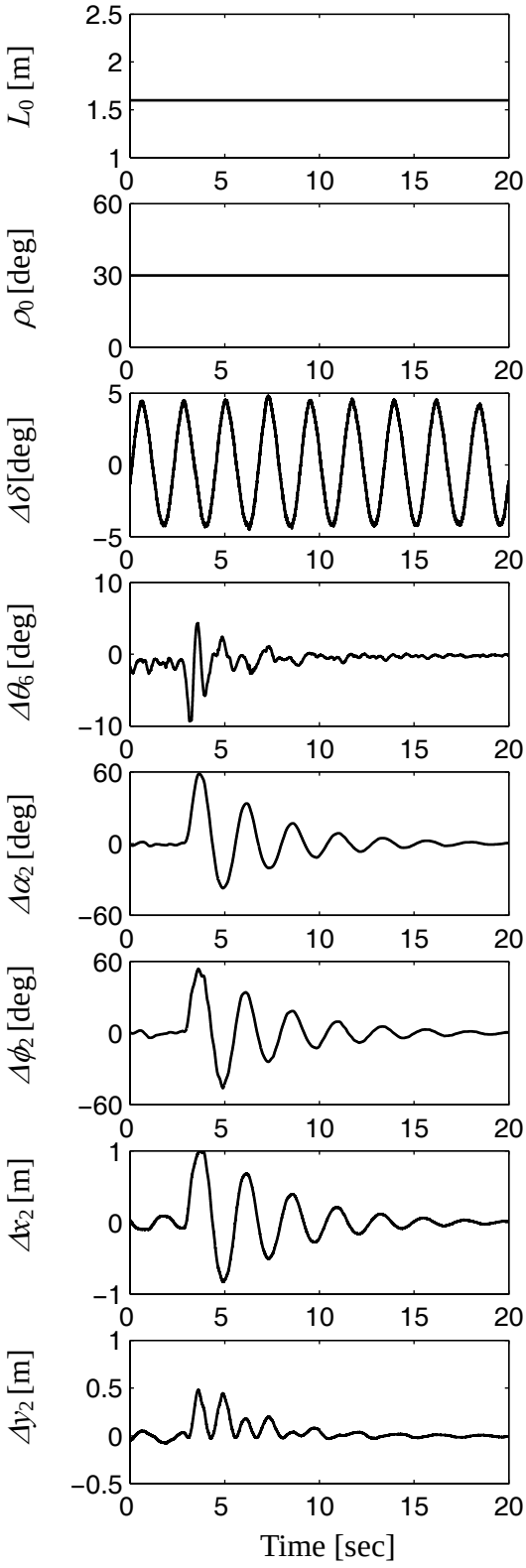

Figure 4.36: Controlled response due to rolling and a horizontal impact force applied to the payload at t≈3 seconds, m_2=8.0 kg

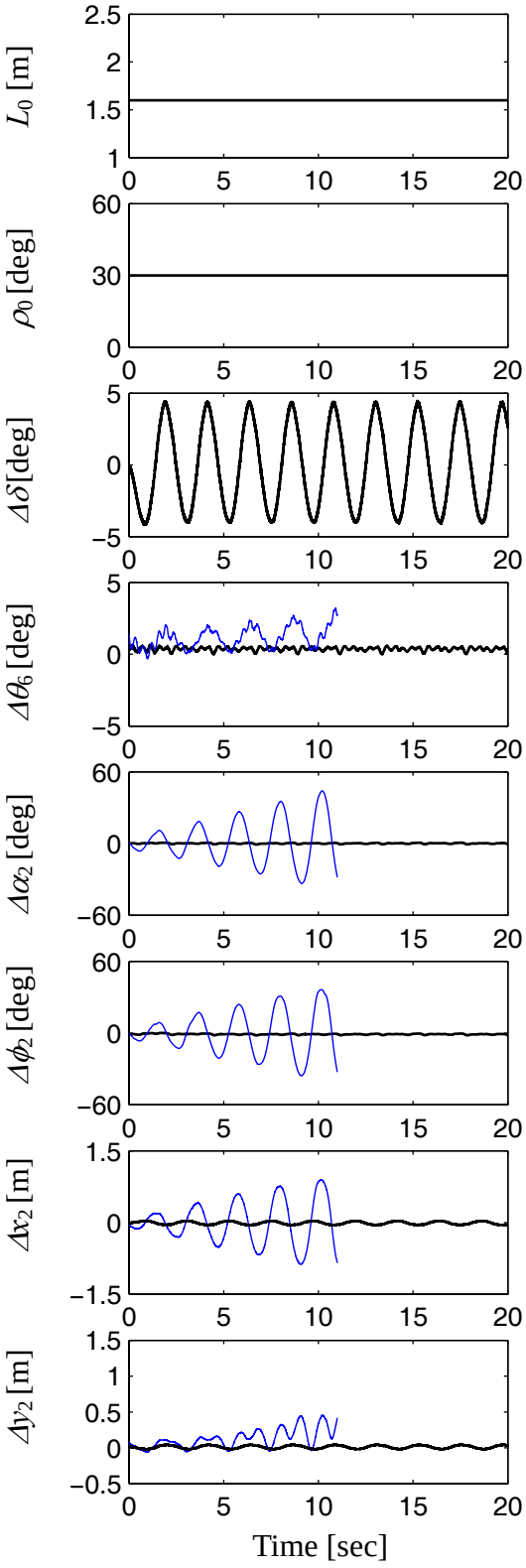

Figure 4.37: Constant cable length and constant luff angle with sinusoidal rolling close to first eigenfrequency, m_2=1.0 kg,
— uncontrolled, — controlled

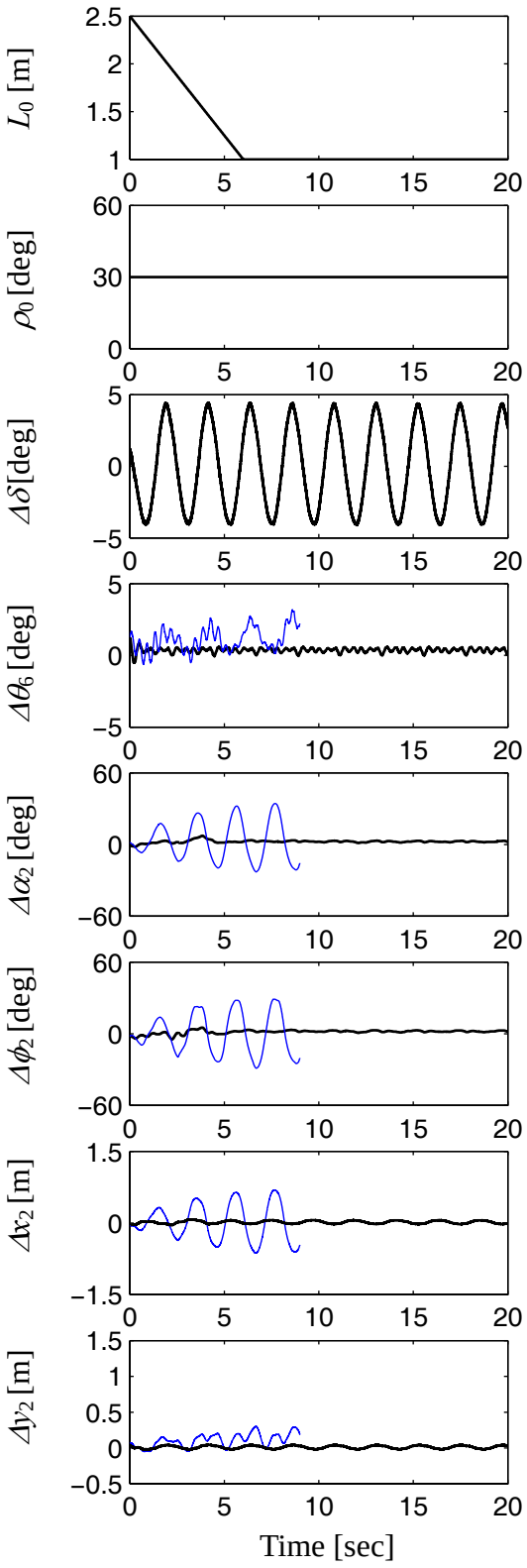

Figure 4.38: Variable cable length and constant luff angle with sinusoidal rolling close to the first eigenfrequency, m_2=1.0 kg,
— uncontrolled, — controlled

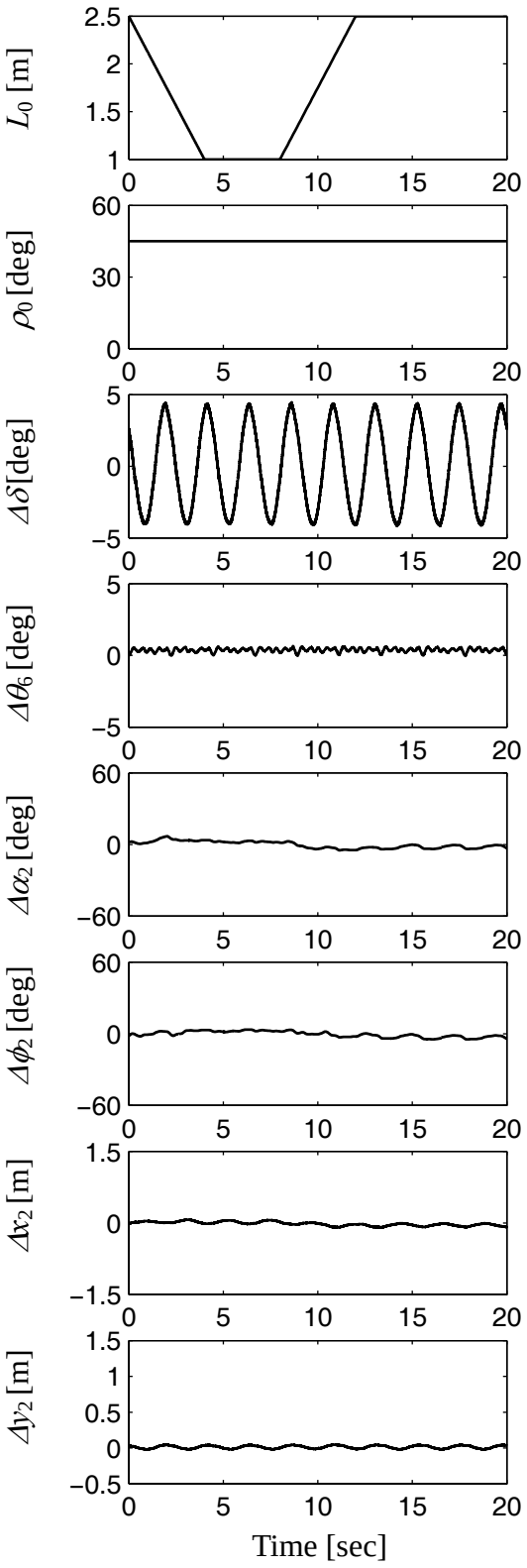

Figure 4.39: Controlled response for rolling excitation with variable cable length, m_2=1.0 kg

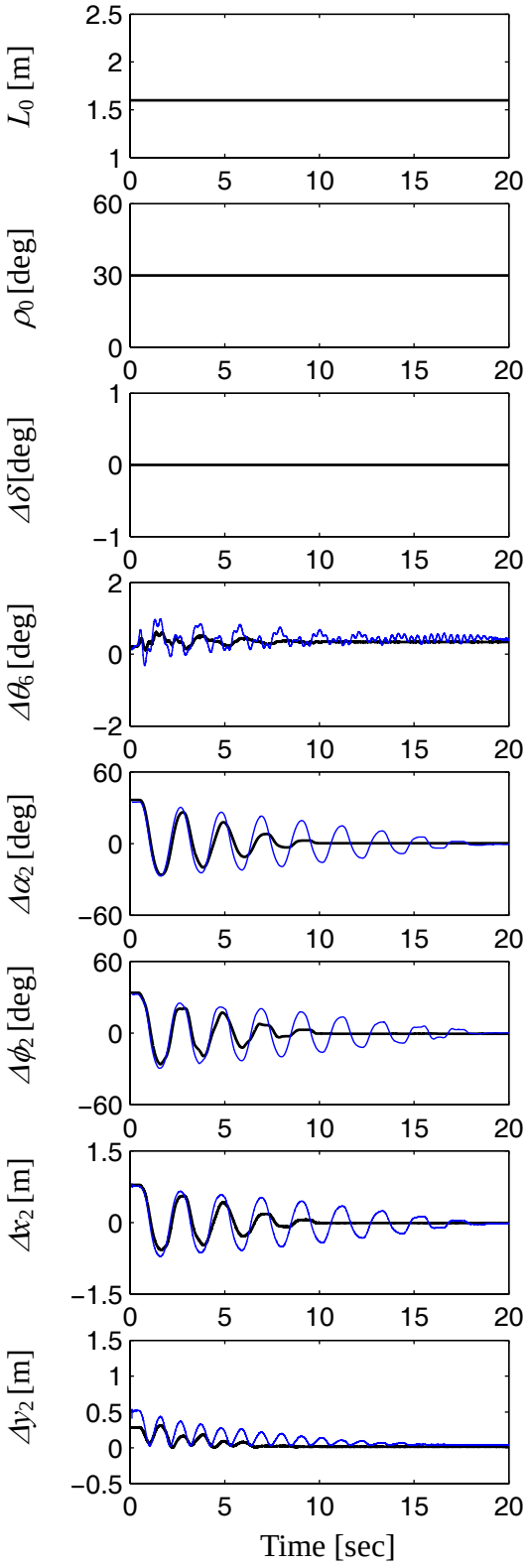

Figure 4.40: Response due to nonzero initial condition $\Delta x_2(0)$=0.8 m, m_2=1.0 kg,
— uncontrolled, — controlled

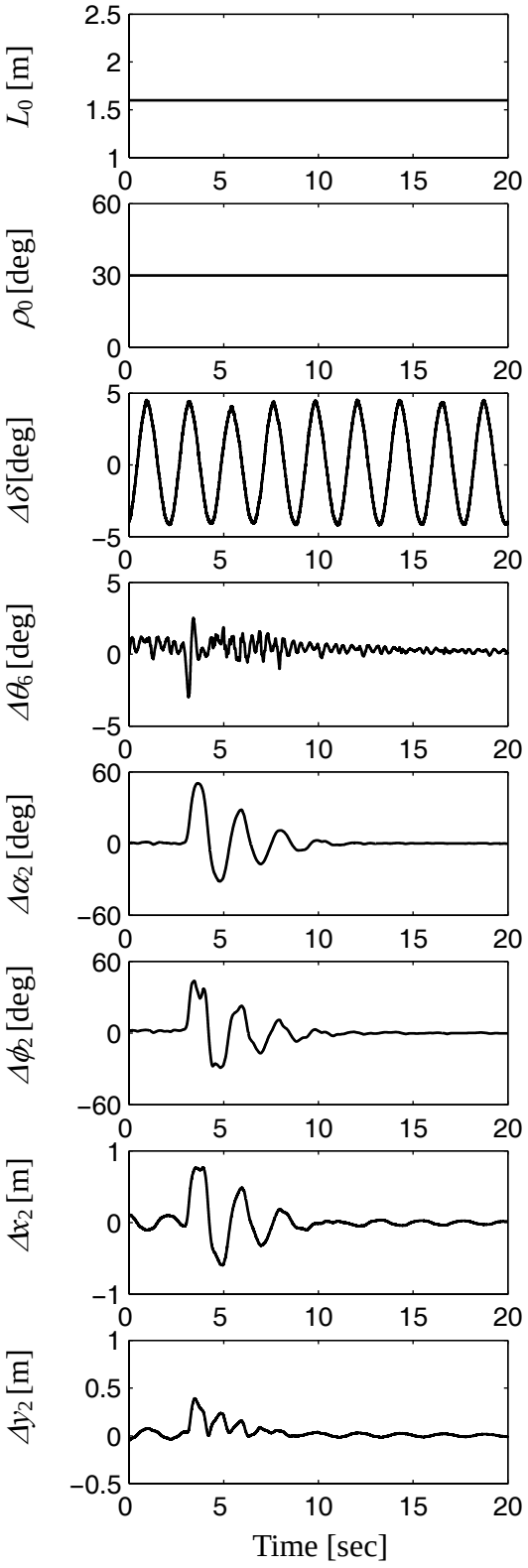

Figure 4.41: Controlled response due to rolling and a horizontal impact force applied to the payload at t≈3 seconds, m_2=1.0 kg

5 Summary, conclusions, and recommendations

5.1 Summary and conclusions

The full nonlinear mathematical mode1 of an elastic ship-mounted crane equipped with Maryland Rigging is derived. The obtained model describes the dynamics of the elastic boom and the payload in addition to the other moving parts (the pulley and the rigid part of the boom) in the plane of the boom. Taylor series expansion method is utilized to expand the model about the current equilibrium point, which varies with the length of the upper cable and the luff angle of the boom. The higher order terms are collected in a separate vector in the right hand side of the governing differential equations. Simulation results showed that the higher order terms has no considerable contribution in the dynamic response of the crane and payload. Therefore, the linear model is considered to design the model-based controller.

Since the model is linearized about the current equilibrium point which is dependent on the operator commands (the cable length and the boom luff angle), the dynamic of the crane is described using a multi model approach; each model is valid only for a specified equilibrium point and therefore for a defined region in the neighborhood of the equilibrium point.

Changing the position of the lower suspension point of the upper cable showed a significant effect in controlling the horizontal vibrations of the payload. Therefore, this improved the controllability of the crane significantly when compared with these cranes with fixed suspension points. The length of the cable has been employed to compensate for the vertical displacements of the payload, and the elastic vibrations were compensated by utilizing the luff angle.

Observability and controllability are guaranteed using three measurements and three control inputs. The states in addition to the disturbance force acting on the payload are reconstructed by a PI-Observer. Two controllers are run in parallel to suppress the vibrations in the crane and payload; the first controller is the rolling disturbance compensator; it produces an input command proportional to the measured roll angle to prevent the sea motions from transmitting to the payload through the structure of the crane. The second controller is an optimal state feedback controller based on the states reconstructed by the PI-Observer; its duty is to create the necessary damping to dampen out the vibrations due to other effect as nonzero initial conditions or disturbance forces acting on the payload, it is also responsible to suppress the vibrations caused by operator commands (hoisting and lowering the payload).

A variable gain observer and a variable-gain controller are designed to control the crane which represented by a multi-model problem; the numerical values of the gains

are updated in real time according to (a) the current operating region, which is determined by the region finder, and (b) the location of the current operating point inside the current region. Each operating region has four corners, and each corner has its own observer and controller gain set. The actual controller and observer gains at any point inside the region are calculated using 2D interpolation polynomial; this ensures a smooth operation of the controller and preserves the stability and performance robustness as demonstrated using the root locus method. In addition, transition of the controller between different operating regions (leaving a certain operating region and entering a new region) takes place gradually and in a smooth manner because any two successive regions have a common edge of two common nodes. This guaranteed that no stepwise change in the gains occurred and therefore chattering in the response is avoided. Simulation results showed that the expressed control strategy has a significant effect in suppressing the vibrations in the crane for different values of the payload mass.

The mathematical model and the proposed control strategy are validated by conducting a set of experiments on a scaled test rig. The controller is implemented using dSPACE, which has been programmed by MATLAB SIMULINK. The experimental results validated the simulation results and showed that the controller works very well and fulfills the theoretical goals. Robustness is confirmed experimentally by testing the performance of the controller for different payload masses and different operating conditions.

Consequently, this work can be considered as a background for a new construction of ship mounted cranes of elastic booms which can carry out the cargo transfer faster than rigid boom cranes with less power consumption. Also, employing the position of the lower suspension as an input can be realized easily without introducing much complexity to the design of crane. This distinguishes the proposed crane design from the previous cranes which have rigid booms and fixed suspension points. Another important advantage which should be added here is that, the proposed crane can operate safely in the worst case scenario of sea motion excitations at the resonance frequencies. This is due to the controllability capability obtained by using the three inputs together.

5.2 Recommendations

For further studies and future works, we recommend the following:

1. Extend the mathematical model to include the out of plane motions
2. Include the dynamics of the actuator in the model
3. Consider the upper part of the boom (part BC) to be also elastic
4. Design a filter in the input side to contribute in damping out the oscillations coming from the operator command inputs.

References

[AN01] Abdel-Rahman, E. and Nayfeh, A., 2001, "Feasibility of two-dimensional control for ship-mounted cranes," *DETC 2001 Proceedings of the ASME Design Engineering Technical Conferences*, Pittsburgh, Pennsylvania, DETC 2001/VIB-21454.

[CR00] Charles L. Phillips, Royce D. Harbror, 2000, "*Feedback Control Systems*," 4nd ed. Prentice-Hall International, New Jersey, USA.

[DV99] Dadone, P. and Van Landingham, H. F., 1999, "The use of Fuzzy logic for controlling Coulomb friction in crane swing alleviation," *Intelligent Engineering Systems through Artificial Neural Networks* **9**, 751-756.

[Dan89] Daniel J. Inman. 1989, "*Vibration with Control, Measurement, and Stability*," Prentice-Hall International, Mexico, pp. 141-182.

[FPE02] Gene F. Franklin, J. David Powell, Abbas Emami-Naeini, 2002, "*Feedback Control of Dynamic Systems*," 4th ed. Prentice Hall, New Jersey.

[HMN01] Henry, R., Masoud Z., Nayfeh, A., and Mook, D., 2001, "Cargo pendulation reduction on ship-mounted cranes via boom-luff angle actuation," *Journal of Vibration and Control* **7**, 1253-1264.

[Hol01] Holman, J. P., 2001, "*Experimental Methods for Engineers*," 7th ed., McGraw-Hill, USA.

[Jac04] Jacob Fraden, 2004, "*Handbook of Modern sensors, Physics, Design, and Applications*," 3rd ed., Springer, New York, USA.

[KHB99] Kimiaghalam, B., Homaifar, A., and Bikdash, M., 1999, "Pendulation suppression of a shipboard crane using fuzzy controller," *Proceedings of the American Control Conference*, San Diego, CA, Vol. 1, pp. 586-590.

[KHB00] Kimiaghalam, B., Homaifar, A., and Bikdash, M., 2000, "Feedback and Feedforward Control Law for a Ship Crane with Maryland Rigging System," *Proceedings of the American Control Conference*, Chicago, IL, Vol. 2, pp. 1047-1051.

[KS105] Krajcin, I., Söffker, D., 2005, “Diagnosis and Control of 3D Elastic Mechanical Structures”. In Precedings 12th international Symposium, Smart Structures and Materials: Smart Structures and Integrated Systems, San Diego, USA, 13 pages.

[KS205] Krajcin, I., Söffker, D., 2005, “Advanced Model-Based Disturbance Rejection Control Using Proportional-Integral-Observer,” *DETC 2005 ASME 20th Biennial Conference on Mechanical Vibration and Noise (VIB)*, Long Beach, California, DETC 2005-84997.

[Lun02] Lunze, 2002 “*Regelungstechnik*2*, Mehrgrößensysteme, Digital Reglung*” Springer Verlag, Berlin.

[MNM04] Masoud Z., Nayfeh, A., and Mook, D., 2004, “Cargo pendulation reduction of ship-mounted cranes,” *Nonlinear Dynamics* **35**, 299-311.

[Mei86] Meirovitch, L. 1986, “*Elements of Vibration Analysis*,” 2nd ed. McGraw-Hill Book Company, New York, Chap. 8, pp. 300-346.

[ML97] Müller, P. C., Lückel, J., 1997, “Zur Theorie der Störgrößenaufschaltung in linearen Mehrgrößenregelsystemen”. Regelungstechnik **25**, pp. 54-59.

[Mül98] Müller, P. C., 1998, “Control of nonlinear systems by applying disturbance rejection control techniques”. In Proceedings IEE Int. Conference CONTROL 88, Institution of Electrical Engineers, London, pp. 734-737.

[Nor00] Norvelle, F. Don. 2000, “*Electrohydraulic Control Systems*,” Prentice Hall, New Jersey.

[Oga02] Katsuhiko Ogata. 2002, “*Modern Control Engineering*,” 4th ed. Prentice Hall, New Jersey.

[Sha03] Shahrokh Yadegari, 2003, “Chaotic Signal Synthesis with Real Time Control: Solving Differential Equations in PD, MAX/MSP, and JMAX,” *Proceedings of the 6th Int. Conference on Digital Audio Effects* (*DAFx-03*), London, UK.

[SBM93] Söffker, D., Bajkowski, J. and Müller, P.C., 1993, “Detection of Cracks in Turbo Rotors – a New Observer Based Method”. ASME Journal of Dynamic Systems, Measurements and Control 3, pp. 518-524.

[SYM95] Söffker, D., Yu, T. J., Müller, P. C., 1995, “State Estimation of Dynamical Systems with Nonlinearities by using Proportional-Integral Observer”. International Journal of System Science, Vol. **26** (9), pp. 1571-1582.

[YHG97] Yuan, G. H., Hunt, B. R., Grebogi, C., Ott, E., Yorke, J. A., and Kostelich, E. J., 1997, “Design and control of shipboard cranes,” *DETC 97 Proceedings of the ASME Design Engineering Technical Conference*, Sacramento, CA, DETC97/VIB-4095.

Notation

L_1, L_2	segments length of the upper cable
L, l	length of the upper cable and length of the payload cable
L_3, L_4, L_5	Geometrical parameters of the crane
D, ρ	position of the lower suspension point and luff angle
α_1, α_2 , ϕ_2	angle of L_1 with the horizontal, angle of L_2 with the horizontal, and angle of l with the vertical
w_i, θ_i	elastic displacement and elastic rotation at node i
β, δ	angle of the boom with the horizontal and roll angle
x_i, y_i	x and y coordinates of m_i, i =1,2
$\boldsymbol{x}_0$, $\boldsymbol{y}_0$	unit vectors in the x_0- and y_0- directions
T_1, T_2, T_3	tension in L_1, L_2, and l
p_2, $\hat{p}_2$	actual and estimated disturbance force
Q_B, M_B	shear force and bending moment at point B
m_1, m_2, m_{BC}	mass of the pulley, payload, and member BC
m, E, I	mass density, elastic modulus, cross section moment of area of the elastic boom
ζ	local coordinate in the finite element
$\boldsymbol{M}_0$, $\boldsymbol{K}_0$	mass and stiffness matrices
$\boldsymbol{B}_1$, $\boldsymbol{B}_2$	input matrices
$\boldsymbol{B}_3$, $\boldsymbol{B}_4$, $\boldsymbol{B}_5$	disturbance matrices
$\boldsymbol{q}$, $\boldsymbol{z}$, $\hat{\boldsymbol{z}}$	displacement vector, state vector, and estimated state vector
$\boldsymbol{u}$, $\boldsymbol{y}$, $\boldsymbol{y}_{\mathrm{m}}$	input, output, and measurement vectors
$\boldsymbol{A}$, $\boldsymbol{A}_e$	system and extended system matrices
$\boldsymbol{B}$, $\boldsymbol{B}_e$	input and extended input matrices
$\boldsymbol{E}$, $\boldsymbol{E}_e$	disturbance and extended disturbance matrices corresponding to rolling
$\boldsymbol{N}$	disturbance matrix corresponding to the wind force acting on the payload
$\boldsymbol{C}$, $\boldsymbol{C}_e$	output and extended output matrices
$\boldsymbol{D}$, $\boldsymbol{F}$	input and disturbance feed forward matrices.
$\boldsymbol{L}_1$, $\boldsymbol{L}_2$, $\boldsymbol{L}_e$	observer gain components and extended observer gain matrix
λ_i	i^{th} eigenvalue
$\boldsymbol{e}$, $\boldsymbol{J}$	error vector and input matrix for the error equation of the observer
$\boldsymbol{Q}$, $\boldsymbol{Q}_e$	weight matrix of the states and the estimated states for the optimal design
$\boldsymbol{R}$, $\boldsymbol{R}_e$	weight matrix of the inputs and the measurements for the optimal design
$\boldsymbol{P}$	solution of Ricatti equation
$\boldsymbol{u}_\delta$, $\boldsymbol{K}_\delta$	input vector and gain of the rolling disturbance compensator
$\boldsymbol{u}_2$, $\boldsymbol{K}_2$	input vector and gain of the wind disturbance compensator
$\boldsymbol{u}_z$, $\boldsymbol{K}_z$	input vector and gain of the optimal controller
η_1, η_2	measurement angles of the upper and lower cables

List of Figures